

**Fumarolic Activity, Acid-Sulfate Alteration and
High-Sulfidation Epithermal Precious Metal
Mineralization in the Crater of
Kawah Ijen Volcano (Java, Indonesia)**

Samantha Scher

**Department of Earth & Planetary Sciences
McGill University
Montreal, Quebec, Canada**

April 2012

**A thesis submitted to McGill University in fulfillment of the
requirements of the degree of Master of Science**

© Samantha Scher, 2012

Abstract

High-sulfidation epithermal deposits are genetically associated with calc-alkaline volcanism in subduction zones, and although these ore deposits are excellent places to focus research, subduction zone stratovolcanoes provide important windows on magmatic-hydrothermal processes that are not available from study of the corresponding ore deposits. There is general agreement that the hydrothermal alteration accompanying the high-sulfidation epithermal ores is the product of volcanic degassing, however, there is considerably less agreement on the nature and origin of the ore fluid. Opinion is divided over whether the ore fluid is a vapor or a liquid, and whether it is entirely volcanic or of mixed volcanic-meteoritic origin.

The research presented here details a field-based investigation of the magmatic-hydrothermal environment of Kawah Ijen volcano, an active stratovolcano (mainly andesitic pyroclastics and lavas) located in the Ijen Caldera Complex in Java, Indonesia. The Kawah Ijen crater is approximately one kilometer in diameter and contains a hyperacidic lake (pH ~ -0.5) and a small and actively degassing solfatara, which is surrounded by a much larger area of acid-sulfate alteration that was exposed during a phreato-magmatic eruption of the volcano in 1817; the eruption excavated the crater to a depth of 250 m. The research described in this thesis involved sampling and chemical analyses of the gases and their condensates (the surface equivalents of the ore-forming magmatic-hydrothermal fluids) collected from the solfatara and rock samples taken from the alteration center.

Condensed fumarolic gases (pH ~ -0.5) released from the solfatara and sampled at temperatures between 330 and 495 °C contain up to 3 ppm Cu and 3.8 ppm As; the concentration of Ag is below detection. The alteration center is characterized by zones of residual silica, alunite-pyrite and kaolinite/dickite; based on alunite-pyrite geothermometry, the area formed at a temperature between 200 and 300 °C. High sulfidation epithermal mineralization occurs in this area in the form of massive and vein-hosted pyrite that contains up to 200 ppb

Au, 16 ppm Ag, 6,800 ppm Cu, and 3,430 ppm As; these elements are invisible at the highest resolution of scanning electron microscopy, and thus occur either in the form of nano-particles or are in solid solution in the pyrite.

The manuscript in Chapter 3 summarizes the observations detailed above to support a model in which highly acidic gases condensed ~ 250 m beneath the floor of the pre-1817 crater at Kawah Ijen volcano. In the area near the source of the vapors, the ratio of fluid to rock was extremely high and resulted in the leaching of elements from the andesitic host rock, leaving behind a residue of “vuggy silica.” With increasing distance from the source, in an area of intermediate fluid/rock ratio, the condensed liquids replaced the primary minerals of the host with alunite and pyrite. The kaolinite/dickite zone formed in a rock-buffered environment (low fluid/rock ratio), in the zone furthest from the vapor source. Gold- silver- and copper-bearing phases were undersaturated in the condensed liquids, however, they were able to concentrate by adsorbing on the surfaces of the growing pyrite crystals, which developed p-type conductive properties as a result of the uptake of arsenic. The metals were incorporated in the pyrite either by their electrochemical reduction to form native metal nano-particles, through coupled substitutions with arsenic for iron and sulfur, or in the case of Cu, by direct replacement of Fe. This thesis provides new insight into the formation of high-sulfidation epithermal deposits, showing, in particular, that high sulfidation epithermal precious metal mineralization can form directly from condensed volcanic gases and that the processes of alteration and metallic mineralization occur synchronously.

Résumé

Les dépôts épithermaux à forte sulfuration sont génétiquement associés au volcanisme calco-alkalin dans les zones de subduction, et bien que ces gisements métallifères soient des places de choix pour focaliser la recherche, les stratovolcans des zones de subduction fournissent d'importantes indications quant aux procédés magmatiques et hydrothermaux qui ne paraissent pas dans l'étude des gisements correspondants. Il existe un accord global sur le fait que le dégazage volcanique soit responsable de l'altération hydrothermale accompagnant les minerais épithermaux à forte sulfuration. Cependant les avis sont considérablement moins unanimes sur la nature et l'origine des fluides du minerai. Le fluide minéralisateur pourrait être soit sous forme de vapeur ou sous forme de liquide, et son origine pourrait être soit entièrement volcanique soit un mélange volcanique-météorique.

Cette étude présente les détails d'une étude sur l'environnement magmatique-hydrothermal du volcan Kawah Ijen, un stratovolcan actif (produisant principalement des pyroclastites andésitiques ainsi que des laves) situé dans le Complexe Ijen Caldera à Java en Indonésie. Le cratère Kawah Ijen a un diamètre d'environ un kilomètre et contient un lac hyper acide ($\text{pH} \sim -0.5$) ainsi qu'une petite solfatare en dégazage actif, entourée d'une aire d'altération acide-sulfate beaucoup plus grande qui était exposée durant l'éruption phréato-magmatique du volcan en 1817; l'éruption avait excavé le cratère à une profondeur de 250 m. L'étude décrite dans cette thèse comprend l'échantillonnage et l'analyse chimique des gaz et de leurs produits de condensation (l'équivalent en surface des fluides magmatiques hydrothermaux ayant formé le minerai) recueillis dans la solfatare et des échantillons de roche pris au niveau du centre de l'altération.

Les gaz de fumerolles condensés ($\text{pH} \sim -0.5$) émis par la solfatare et échantillonnés à des températures entre 330 et 495 °C contiennent jusqu'à 3 ppm Cu et 3.8 ppm As; la concentration de Ag est sous le niveau de détection. Le centre de l'altération est caractérisé par des zones de silice résiduelle, d'alunite-

pyrite et de kaolinite/dickite; selon la géothermométrie de l'alunite-pyrite, la zone s'est formée à des températures entre 200 et 300 °C. La minéralisation épithermale à forte sulfuration survient à cet endroit sous la forme de pyrite massive dans la veine hôte, contenant jusqu'à 200 ppb Au, 16 ppm Ag, 6800 ppm Cu et 3340 ppm As; ces éléments sont invisibles sous la plus forte résolution du microscopie à balayage électronique, et donc apparaissent soit sous la forme de nano-particules soit en solution solide dans la pyrite.

Le manuscrit du chapitre 3 résume les observations décrites ci-haut, supportant un modèle dans lequel des gaz très acides ont été condensés à ~ 250 m sous le plancher du cratère pré-1817 du volcan Kawah Ijen. Dans la région près de la source de vapeur, le ratio fluide/roche était extrêmement élevé et a eu pour résultat le lessivage d'éléments de la roche hôte andésitique, laissant derrière un résidu de silice vacuolaire. En s'éloignant de la source, vers une zone où le ratio fluide/roche est intermédiaire, les liquides condensés ont remplacé les minéraux primaires de l'hôte avec de l'alunite et de la pyrite. La zone kaolinite/dickite s'est formée dans un environnement où la roche était en tampon (faible ratio fluide/roche), dans la zone la plus éloignée de la source de vapeur. Les phases contenant soit or, argent ou cuivre étaient sous-saturés en liquides condensés, cependant ils étaient aptes à se concentrer par adsorption sur les surfaces des cristaux de pyrite en croissance, ayant développé des propriétés conductrices de type p résultant de l'assimilation d'arsenic. Les métaux ont été incorporés dans la pyrite soit par la réduction électrochimique pour former des nanoparticules de métal, soit par substitutions couplées du fer et du soufre par l'arsenic, ou dans le cas du Cu, par remplacement direct du Fe. Cette thèse procure une vision nouvelle quant à la formation de dépôts épithermaux à forte sulfuration, en montrant, en particulier, que la minéralisation épithermale à forte sulfuration de métaux précieux peut se former directement à partir des gaz volcaniques condensés, et que les procédés d'altération et de minéralisation métallifère peuvent se produire simultanément.

Contribution of Authors

This thesis is divided into three chapters of which one is a scientific paper. This paper will be submitted to a peer-reviewed journal for publication. I am the first author of this paper and share the authorship with my supervisor, A.E. Williams-Jones and Glyn Williams-Jones, a professor at Simon Fraser University that is the co-supervisor of the Kawah Ijen volcano research group and was instrumental in writing this paper. I carried out the field work, prepared and analyzed the samples, interpreted the data, and wrote the paper. Both of the co-authors on the paper participated in the field work and contributed to the data interpretation and edited the chapters. I developed the ideas and the models proposed in the papers with input from my supervisor and second co-author on the paper.

Acknowledgments

Foremost I would like to thank my supervisor, Willy, for giving me the opportunity to travel to Indonesia and climb Kawah Ijen everyday for almost two months. More importantly, his insight, guidance and support were invaluable to my fieldwork and thesis.

To Vincent van Hinsberg, Glyn Williams-Jones, Nathalie Vigouroux, Guillaume Mauri, Stephanie Palmer, Kim Berlo, as well as my volunteer field assistants, Thibault, Dini, Robin, Elsa, and Sigolyn, and local miners Jumanto and Pa Im: thank you for all your assistance with my fieldwork and helping me during the course of my project. Thanks to John Stix for his input during my committee meetings. Also many thanks to Lang Shi (McGill), Michel Preda (UQAM), Simon Jackson (GSC), and Dani-D Savard (UQAC) for their help in using the electron microprobe, X-ray diffraction and LA-ICPMS, respectively.

To my friends at McGill University, thank you for breaking up the monotony of sitting at a computer or crushing rocks all day. Finally, a special thanks to Ariel, Leigh-Ann, Danielle, Jahan, Jason, Laura, Cheeks, Patrick, Anne, and my family, especially Mike, for their support.

Table of Contents

Title page	i
Abstract	ii
Résumé	iv
Contribution of authors	vi
Acknowledgments	vii
Table of contents	viii
List of tables	x
List of figures	xi
Appendices	xii
Chapter 1: General Introduction	1
1.1 Introduction	1
1.2 Low- and high-sulfidation epithermal deposits	2
1.3 Models for the formation of high-sulfidation epithermal systems	2
1.4 Aqueous geochemistry of gold	5
1.5 Gold in high-sulfidation epithermal systems	6
1.6 Modern analogues of high-sulfidation epithermal systems	7
1.7 Kawah Ijen Volcano	8
1.8 Objectives of the study	9
1.9 Methods	9
1.10 Thesis organization	12
1.11 References	13
Chapter 2: Geologic Setting	20
2.1 Geotectonic setting of Indonesia	20
2.2 Ijen Caldera Complex	24
2.3 Kawah Ijen Volcano	26
2.4 The hydrothermal system at Kawah Ijen	31
2.5 References	32

Introduction to Chapter 3	35
Chapter 3: Fumarolic Activity, Acid-Sulfate Alteration and High-Sulfidation Epithermal Precious Metal Mineralization in the Crater of Kawah Ijen Volcano (Java, Indonesia)	36
Abstract	37
3.1 Introduction	39
3.2 Geological Setting	40
3.3 Eruptive History	45
3.4 Methodology	46
3.5 The Alteration Center	49
3.5.1 Mass changes accompanying alteration	56
3.5.2 Alunite chemistry	62
3.5.3 Pyrite chemistry	64
3.5.4 Sulfur isotopes	67
3.6 Gas and Sublimate Composition	67
3.7 Discussion	72
3.7.1 Introduction	72
3.7.2 Pressure-temperature	73
3.7.3 $fO_2 - pH$	74
3.7.4 Fluid-rock interaction	76
3.7.5 Transport and deposition of metals	83
3.7.6 Model for alteration and pyrite enrichment at Kawah Ijen	84
3.8 Conclusions	85
3.9 References	86
Chapter 4: Thesis Conclusions and Contributions to Knowledge	94
4.1 Main Findings	94
4.2 Contributions to Knowledge	95
4.3 References	96

List of Tables

Chapter 3

1. LA-ICPMS analyses of pyrite grains	55
2. Whole rock compositions for unaltered Kawah Ijen volcanics	57
3. Whole rock compositions for altered Kawah Ijen crater rocks	58
4. Electron microprobe analyses of alunite crystals	65
5. Electron microprobe analyses of pyrite grains	66
6. Sulfur isotope analysis of alunite-pyrite pairs	70
7. Composition of fumarolic gases and their condensates	71
8. Compositions used for fluid/rock simulation	78

List of Figures

Chapter 1

1. Alteration center sample locations11

Chapter 2

1. Tectonic setting of Indonesia21
2. Single-channel analog seismic reflection profile across the subduction zone
of Central Java22
3. Schematic of the geomorphology of the Ijen Caldera Complex25
4. The summit of Kawah Ijen27

Chapter 3

1. Tectonic setting of Indonesia41
2. Schematic of the geomorphology of the Ijen Caldera Complex43
3. Total Alkali-Silica (TAS)44
4. Map of the alteration center in the Kawah Ijen crater50
5. Macroscopic features of altered rocks in the Kawah Ijen crater52
6. Backscattered electron microprobe images showing textural relationships in
the alteration center53
7. Binary plots of immobile element concentrations at Kawah Ijen59
8. Binary plot of TiO_2 v Al_2O_3 61
9. Diagrams of relative mass changes in the alteration center63
10. Binary plots of Au versus Ag, Cu and As concentrations in pyrite68
11. Binary plots of Ag, Cu and As concentrations in pyrite69
12. $\log f\text{O}_2$ – pH diagram of the system K-Al-Si-O-H, Fe-S-O and S-H75
13. Reaction progress diagrams80

List of Appendices

I. Sample locations and mineral proportions	97
II. LA-ICPMS analysis of pyrite grains	99
III. Whole rock compositions of unaltered Kawah Ijen volcanics	105
IV. Whole rock compositions of altered Kawah Ijen crater rocks	106
V. Electron microprobe analysis of pyrite grains	111
VI. Composition of fumarolic gases and their condensates	112
VII. logK and reactions for log f O ₂ – pH diagram	114

General Introduction

1.1. Introduction

Epithermal deposits form at shallow depth (between 1 and 2 km beneath the erosional surface) and at relatively low temperature ($<300\text{ }^{\circ}\text{C}$; White and Hedenquist, 1995). These deposits typically host Au and Ag mineralization as well as base metals, Sb, Hg, and S. Epithermal deposits are located in subduction-related tectonic environments and most are hosted by Tertiary or younger volcanic rocks, although there are rare epithermal deposits that formed as early as the Precambrian age (White and Herrington, 2000; Groves and Bierlein, 2007). This age distribution is likely due to variations in erosional and volcanic activity; i.e., preservation and global tectonics (e.g., subduction-related calc-alkaline volcanism during continent assembly; White and Herrington, 2000).

There are two classification schemes for epithermal deposits; acid-sulfate and adularia-sericite (Heald et al., 1987) and high sulfidation and low sulfidation, respectively (Hedenquist et al., 1994). The former classification scheme is based on the nature of the ore-forming fluids (reduced, neutral-pH and oxidized, acidic, respectively) and the alteration mineralogy associated with each of these systems. By contrast, the classification into high and low sulfidation subtypes is based on the oxidation state of the sulfur, +6 in the case of high sulfidation and -2 for low sulfidation. These terms were originally intended to reflect the oxidation state of sulfur in the hydrothermal fluid, e.g., HSO_4^- , SO_4^{2-} , $\text{SO}_{2(\text{g})}$ versus HS^- and H_2S . However, the terms have evolved to reflect the sulfidation state deduced from the sulfide assemblages formed in these deposits (Cooke and Simmons, 2000; Hedenquist et al., 2000). High sulfidation deposits generally contain pyrite, enargite/luzonite and covellite, whereas low sulfidation deposits contain pyrite, pyrrhotite, arsenopyrite, and low-Fe sphalerite. Hedenquist et al. (2000) later proposed a third class of intermediate sulfidation deposits. This class contains an 'intermediate' sulfidation-state assemblage of pyrite-tetrahedrite/tennantite-chalcopyrite and low-Fe sphalerite. One of the problems with a classification system based on the oxidation state of sulfur is both low- and high-

sulfidation subclasses may contain minerals with the same oxidation state for sulfur, e.g., pyrite, which has an oxidation state of -1.

The high sulfidation epithermal alteration expressed as proximal to distal vuggy silica, advanced argillic and argillic zones is widely interpreted to be the result of interaction of the rocks with highly acidic volcanic vapors (Stoffregen, 1987; Hedenquist and Lowenstern, 1994; White and Hedenquist, 1995). However, whether these vapors are also the source of gold and other ore-metals is heavily debated. Likewise, the timing of the alteration and ore-stage mineralization is also debated, with some researchers proposing a post-alteration timing and others proposing that alteration and ore-formation are contemporaneous (Gray and Coolbaugh, 1994; Ruggieri et al., 1997; Williams-Jones et al., 2002; Mavrogenes et al., 2010; Henley and Berger, 2011; Berger and Henley, 2011). These issues, as well as the physicochemical conditions under which the alteration takes place and how these physicochemical conditions are manifested in changes in mineral assemblage and mineral chemistry, are the focus of this thesis.

1.2. Low- and high- sulfidation epithermal deposits

Low sulfidation, or adularia-sericite, epithermal deposits occur in geothermal environments and are interpreted to form from fluids that have near-neutral pH, low salinity and reduced fO_2 (Cooke and Simmons, 2000; White and Hedenquist, 1995). These deposits have open-space vein-fill character and their gangue mineralogy is dominated by quartz, adularia, fine grained muscovite, illite and calcite; electrum is the principal gold-bearing mineral (White and Herrington, 2000; Cooke and Simmons, 2000). Other minerals found in these deposits are acanthite, silver-sulfosalts, base metal sulfides, and pyrite. The low sulfidation alteration minerals, in order of increasing distance from the gold-ore veins, are adularia, illite or muscovite, and a propylitic assemblage that includes chlorite, calcite, and epidote (Cooke and Simmons, 2000).

High sulfidation, or acid-sulfate, epithermal deposits occur in the upper parts of volcanic edifices. Until recently, these systems were believed to form at temperatures from 150-350 °C (White and Hedenquist, 1995), however recent studies have documented vapor fluid inclusion evidence of formation temperatures in excess of 665

°C (e.g. Mavrogenes et al., 2010; Henley and Berger, 2011). The magmas are oxidized and the local volcanism, by increasing the fracture porosity, enhances the ability of hydrothermal fluids to move within the shallow crust (Tosdal et al., 2009). The extremely acid fluids responsible for mineralization are generally considered to be condensates from magmatic vapors (Stoffregen, 1987; Hedenquist et al., 1994; Arribas 1995; Mavrogenes et al., 2010) that contain elevated concentrations of HCl, and H₂SO₄ produced by the reaction of SO₂ and H₂O (Hedenquist et al., 1994). These fluids can leach even the most immobile elements (e.g., Al), producing rocks consisting dominantly of residual quartz, termed vuggy silica by Stoffregen (1987) because of pores left by the dissolution of phenocrysts in the precursor volcanic rocks. The alteration sequence of vuggy silica to advanced argillic, to argillic and finally to propylitic alteration is interpreted to reflect the progressive neutralization of the fluids by the wall rocks (Steven and Ratté, 1960). In many deposits, the precious metal and associated base metal mineralization postdates the bulk of the wall-rock alteration. For this reason and an assumption that the solubility of metals in vapor is extremely low, many researchers have concluded that the ore fluid is an aqueous liquid, perhaps a hypersaline liquid exsolved from a felsic magma (e.g. Hayaba et al., 1985; White, 1991; Hedenquist and Lowenstern, 1994; Hedenquist et al., 1994; Arribas, 1995; Hedenquist et al., 1998). Nevertheless, there are some high sulfidation epithermal gold-silver deposits, for which there is strong evidence that ore deposition accompanied alteration, thereby implying that the ore fluid may have been a vapor (Chouinard et al., 2005a; King et al., 2010; Mavrogenes et al., 2010; Henley and Berger, 2011; Berger and Henley, 2011). There is also growing evidence that hydrothermal vapors may be able to dissolve metals in concentrations sufficient for them to become ore fluids (Heinrich et al., 1992; 1999; Archibald et al., 2001; 2002; Williams-Jones and Heinrich, 2005).

1.3. Models for the formation of high sulfidation epithermal deposits

The model for the concentration of metals in magmas and their transfer to hydrothermal liquids has been summarized in reviews by Burnham (1979), Burnham and Ohmoto (1981) and White (1981). Such transport is governed by processes that must operate

during crystallization of a magma body. The most important of these is the exsolution of a separate, H₂O-rich phase from the magma. Metal transport via this phase begins with fractional crystallization in the magma chamber which serves to enrich the residual melt in H₂O and in constituents not partitioned into common igneous minerals (e.g., plagioclase, pyroxene). This enrichment process concentrates ore metals, S and Cl in the more hydrous residual melt. Cooling and the resulting crystallization of the melt beyond the point of water saturation causes H₂O to separate from the residual melt by a process called second, or resurgent, boiling. Eventually all the original H₂O in the magma, except that bound structurally in hydrous minerals, must be exsolved as a separate fluid phase (i.e., H₂O-saturated melt → crystal + volatile phase). In addition, the aqueous phase is able to scavenge additional metals from wall rocks in the system. The volatiles that are partitioned into the aqueous phase (e.g., HCl, CO₂, SO₂, and H₂S) may be responsible for part of the argillic alteration in the upper, cooler parts of the fracture systems. Higher in the magmatic system, circulating groundwaters play an integral role in ore-forming processes.

An alternative to the transport of metals in magmatic hydrothermal liquids is via the vapor phase (e.g., review by Williams-Jones and Heinrich, 2005). This alternative was re-evaluated (the notion of the transport of metals by vapor has received consideration since at least the 16th century; Williams-Jones et al. 2009) when Heinrich et al. (1999) demonstrated that the concentrations of Cu and Au are commonly higher in vapor inclusions than they are in coexisting brine inclusions. Also, analyses of fumarolic vapors yield appreciable concentrations of ore metals (ppb to ppm) and these same vapors commonly deposit significant quantities of ore minerals as sublimates (Williams-Jones and Heinrich, 2005 and references therein). In the vapor transport model for magmatic hydrothermal systems, the vapor is defined as an aqueous fluid of any composition with a density lower than its critical density. The starting point for the model is the emplacement of a magma at relatively shallow crustal levels and exsolution of a single-phase supercritical aqueous fluid with vapor-like density. Upon cooling and decompression, the fluid will condense a brine if it passes into the two-phase region or will cool along a path that avoids this region and contract to liquid; the composition of the expanding vapor will not be significantly changed (Williams-Jones

and Heinrich, 2005). This process occurs in the subjacent porphyry environment where vapor and brine (FeCl_2 -rich) reach Cu-Fe sulfide saturation as the two phases cool below 425 °C. The resulting vapor is enriched in H_2S , SO_2 , Au, Cu and As and moves to higher levels where it gives rise to epithermal mineralization. In the epithermal environment, the vapor condenses, producing advanced argillic alteration, residual vuggy quartz and deposits precious metal- and Cu-As-bearing minerals.

In the modern era, transport via a vapor phase has largely been ignored due in part to thermodynamic calculations of Krauskopf (1957; 1964) showing that the solubility of metals in the vapor phase is exceptionally low. These calculations, however, did not consider the possibility that the metals might interact with vapor thereby enhancing their solubility (Williams-Jones et al., 2002), but instead were based entirely on considerations of metal volatility. Recently, however, it has been shown that as the density of water vapor increases with rising pressure along the liquid-vapor equilibrium curve, its ability to hydrate ions and to complex metal species increases dramatically (Liebscher, 2007). Another misconception involves the nature of resurgent boiling during the exsolution of magmatic fluids. Reynolds and Beane (1985) concluded that second boiling can only produce a single-phase supercritical fluid, however, Sourirajan and Kennedy (1962) showed that both liquid and vapor can be stable at the salinity and pressure-temperature conditions of typical porphyry-epithermal ore-forming systems. Thus, instead of the vapor forming by the condensation of a supercritical fluid, it is possible that in some cases the vapor may exsolve directly from the magma. A further common misconception is that the mass of the vapor phase exsolved during magmatic processes is much smaller than that of the co-evolved liquid phase and as such is of little importance in ore-forming processes (Burnham, 1979). This misconception was exposed by Henley and McNabb (1978) who demonstrated that the exsolving magmatic plume is commonly vapor-dominated by mass.

1.4. Aqueous geochemistry of gold

In high temperature magmatic-hydrothermal liquids, gold dissolves mainly as chloride complexes (e.g. AuCl_2^-), whereas bisulfide complexes (i.e., $\text{Au}(\text{HS})_2^-$ and $\text{Au}(\text{HS})^0$) predominate at temperatures below 350 °C (Benning and Seward, 1996; Gammons and

Williams-Jones, 1997; Stefansson and Seward, 2004; Williams-Jones et al., 2009). Thus, at the conditions of high sulfidation epithermal ore deposition (i.e., temperatures up to ~350 °C), gold transport is likely to occur mainly as the species $\text{Au}(\text{HS})_2^-$ and $\text{Au}(\text{HS})^0$.

The transport of gold as chloride complexes is strongly favored by oxidizing conditions (Gammons and Williams-Jones, 1997). By contrast, at high $f\text{O}_2$, H_2S is oxidized to SO_2 and/or aqueous sulfate, sharply decreasing gold mobility as bisulfide complexes (e.g. Shenberger and Barnes, 1989; Renders and Seward, 1989; Hayashi and Ohmoto, 1991; Pan and Wood, 1994; Benning and Seward, 1996; Gammons and Williams-Jones, 1997; Stefansson and Seward, 2004). The actual nature of the bisulfide complex depends on pH; at lower pH (high sulfidation) the complex AuHS^0 predominates, whereas at neutral pH (low sulfidation) $\text{Au}(\text{HS})_2^-$ is the dominant bisulfide complex (Benning and Seward, 1996; Stefansson and Seward, 2004). The stability constants for these species reach maxima at 350 and 250 °C, respectively, because of the association of H^+ and HS^- to form H_2S , which limits the availability of the ligand HS^- (Gammons and Williams-Jones, 1997; Williams-Jones et al., 2009).

1.5. Gold in high sulfidation epithermal systems

High sulfidation epithermal deposits host $\text{Au} \pm \text{Cu} \pm \text{Ag}$ mineralization. The mineralization typically includes enargite (and its low-temperature dimorph luzonite), which is commonly early in the petrogenesis. Gold mineralization generally post-dates enargite and is frequently associated with lower sulfidation state minerals such as tennantite-tetrahedrite, chalcopyrite and tellurides, which overprint enargite (Sillitoe, 1999; Hendequist et al., 2000). The most common Au-bearing minerals are native gold and tellurides, whereas silver commonly occurs in tellurides, Au-Ag alloy and Ag-bearing sulfosalts (Arribas, 1995).

In many high sulfidation epithermal systems, metals, such as Au, Cu and Ag, can also be “invisible” and is thought to be either bound in the structure of pyrite or occur as nanoparticles in pyrite (Chouinard et al., 2005a; Voudouris et al., 2011). This pyrite can also contain other trace elements, notably As, Se, and Te. In some case their distribution and that of Au, Cu and Ag is concentrically and sectorally zoned and their incorporation

into the pyrite structure is controlled crystallographically by the nature of the growth surfaces (Chouinard et al., 2005b). Gold associates with either As or Cu and, if structurally bound, may be in coupled substitutions involving the Fe^{2+} and S^- sites or the Fe^{2+} site alone (Cabri et al., 1989; Cook and Chryssoulis, 1990; Chouinard et al., 2005b). In coupled substitutions, ionic size and charge must be preserved. The As-Au coupled substitution is well-documented (e.g. Cabri et al., 1989; Cook and Chryssoulis, 1990; Fleet et al., 1993; Fleet and Mumin, 1997); Arsenic and Au replace S and Fe, respectively. In the Au-Cu association, Au must enter the pyrite structure as Au^{3+} (99 pm) in a coupled substitution with Cu^+ (91 pm) according to the coupled reaction Au^{3+} (99 pm) + Cu^+ (91 pm) \leftrightarrow 2Fe^{2+} (150 pm). The larger average size of the substituting cations is accounted for by the substitution of Se^- (232 pm) for S^- (219 pm). In contrast to the As-Au coupled substitution, the Au-Cu association which involves Au in the 3^+ state requires low pH and high $f\text{O}_2$, conditions that are associated with the formation of high sulfidation deposits (Chouinard, 2005a).

1.6. Modern analogues of high sulfidation epithermal systems

A major reason that questions surrounding metal transport and deposition in high sulfidation epithermal systems have not been resolved is that researchers are invariably forced to base their interpretations on observations made millions of years after the hydrothermal activity that produced the deposits has ceased. Considering that high sulfidation epithermal systems are volcanic in nature, the study of active volcanoes, specifically the associated magmatic-hydrothermal environment, may provide important insights into the mechanisms by which gold is transported and deposited. Surface expressions of magmatic-hydrothermal systems in the high sulfidation environment include degassing fumaroles, acid springs and acid crater lakes (Giggenbach, 1987; Hedenquist et al., 1993; van Hinsberg et al., 2010b).

A high-temperature, low-density magmatic vapor from the crystallization of a hydrous magma is manifested at active stratovolcanoes through eruptions intermittent with high-temperature fumarolic activity; catastrophic eruptions occur when there is sudden fluid exsolution over a large depth interval (Hedenquist et al., 1993; Taran et al., 1995; Heinrich, 2007). At near-surface lithostatic pressure, the magmatic vapor will

expand rapidly on ascent, and precipitate any salts and metals as sublimates at high temperature. This vapor is rich in acidic volatiles, including SO_2 , H_2S and HCl , although the concentration of salts and ore metals is relatively low compared with metal concentrations in ore-forming liquids. The latter is readily explained by the observation discussed earlier that metal solubility in the vapor is controlled by hydration and that this depends in turn on the density of the vapor. At the very low pressure of fumarolic gases (close to atmospheric pressure) the density is simply too low for significant hydration of ions and aqueous complexes (Williams-Jones et al., 2002; Williams-Jones and Heinrich, 2005).

Even when a volcano appears to have all the characteristics of a high sulfidation epithermal environment, it does not follow that it will be the site of high sulfidation precious metal mineralization. For example, White Island volcano in New Zealand's Taupo Volcanic Zone is the location of a modern high sulfidation epithermal system (Hedenquist et al., 1993); the crater floor contains high-temperature fumaroles (discharges directly from a subjacent degassing magma; Giggenbach, 1987) and acid springs associated with the degassing andesitic magma. Andesitic ejecta from the volcanic vent contain pervasive and fracture-controlled cristobalite-alunite-anhydrite-pyrite alteration assemblages and veins filled with alunite, anhydrite, Al-rich chlorite, and trace pyrite. Furthermore, the magmatic gases discharging from White Island have oxidation potentials near the $\text{SO}_2/\text{H}_2\text{S}$ gas buffer, which is consistent with the oxidized conditions inferred for high sulfidation epithermal deposits (Giggenbach, 1987). The daily flux of copper and gold in the magmatic gas plume is 280 kg Cu/d and 0.1 kg Au/d (Hedenquist et al., 1993); this is equivalent to approximately 30 metric tons of Au accumulating in ~850 years. However, there is no evidence that significant metals have been deposited at the volcano (it is of course possible that there may be unexposed precious metal mineralization at depth).

1.7. Kawah Ijen Volcano

Kawah Ijen is a basaltic-andesite to dacitic stratovolcano and is the only active volcano in the Ijen Caldera Complex, Java, Indonesia (see Chapter 2). The volcano exhibits characteristics similar to those of White Island, and for this reason it is important to

study. Kawah Ijen contains an active, heavily altered solfatara (alunite) with degassing fumaroles that is within an area of extensive hypogene high sulfidation epithermal alteration (vuggy silica, alunite, kaolinite, and pyrite). In addition to the massive alunite-pyrite alteration, there are also pyrite-alunite veins. This area was exposed as a result of a relatively large phreato-magmatic eruption that took place in January, 1817 (Hengeveld, 1920). The crater at Kawah Ijen also contains a hyperacidic crater lake (pH ~-0.5) and thermal springs that emerge directly from the magmatic-hydrothermal system (Palmer, 2009; van Hinsberg et al., 2010a; b). Thus, Kawah Ijen volcano presents a rare opportunity to study an analogue that has most of the features characteristic of environments in which high sulfidation epithermal deposits are considered to form.

1.8. Objectives of the study

The overall objectives of this study were:

- 1) To map the distribution of the different high sulfidation epithermal alteration types at Kawah Ijen, i.e., residual silica, advanced argillic and argillic zones;
- 2) To determine the protolith to the alteration and the physicochemical conditions under which this alteration took place;
- 3) To determine whether there is any precious and/or base metal mineralization at Kawah Ijen and if so to determine:
 - How this mineralization occurs, e.g. whether the acidic volcanic vapors are also the source of gold and other ore-metals or if some other process is responsible;
 - The spatial and temporal relationship of the precious metal mineralization to the alteration;
- 4) To establish how changes in physicochemical conditions are manifested in changes in mineral assemblages and mineral chemistry

1.9. Methods

Since 2007, a multi-disciplinary research group from McGill University (Montreal, QC) and Simon Fraser University (Vancouver, B.C.) has sampled the gases (major and minor gas species, plus trace element in condensates) and mineral precipitates from the active

dome, the crater lake and spring waters beyond the crater, conducted melt inclusion studies of tephra deposits on the volcanic edifice, and carried out gravity and self-potential surveys of the Ijen crater. In addition, the author of this thesis collected rock samples from the alteration center in order to determine the type and extent of high sulfidation alteration and to determine whether the center is mineralized. The data obtained from analysis of these different materials have allowed interpretation of the observed alteration and an assessment of potential associated precious and base metal mineralization.

Fieldwork for this study was conducted at Kawah Ijen volcano from July 16 to August 8, 2009 and August 3 to 15, 2010 and involved collecting gas, condensate and sublimate data from the active dome and sampling the rocks necessary for creating the alteration center map (Fig. 1), establishing the mineral assemblages and ultimately the physicochemical conditions under which the alteration and mineralization formed. In July and August 2009, sampling focused mainly on Valley S of the KISS Alteration Center and on the solfatara (active dome); some preliminary samples were taken from KISS Valleys A, B, and C to establish whether the alteration extended beyond Valley S. In addition, a total of 12 samples were collected from the active dome. The August 2010 field season focused on sample collection from Valleys A, B, and C, and the path up to the crater rim. The crater was also explored for more subtle geologic features missed the previous year, e.g., evidence for the nature of the protolith(s) to the alteration (basaltic lavas, epiclastic and clastic flows, pillow lavas) and boulders in the center of the valleys (to see if there were older generations of alteration), and any post-alteration mineral precipitates (gypsum and sulfur veins).

Analytical techniques employed in the research comprised optical petrography, electron microprobe analysis (conducted at McGill University, Montreal, QC using a JEOL 8900L microprobe), whole rock by ICP and trace elements by ICP-MS at ACME Analytical Laboratories (Vancouver, BC), X-ray diffraction (XRD; conducted at the Université du Québec à Montréal and the Université du Montréal, Montréal, QC on a Siemens D5000 and D8 Advance, respectively), laser-ablation-induced coupled mass spectrometry (LA-ICPMS; Geologic Survey of Canada, Ottawa, ON and Université du Québec à Chicoutimi, Chicoutimi, QC on a Agilent 7700x and Agilent 770x ICP and an

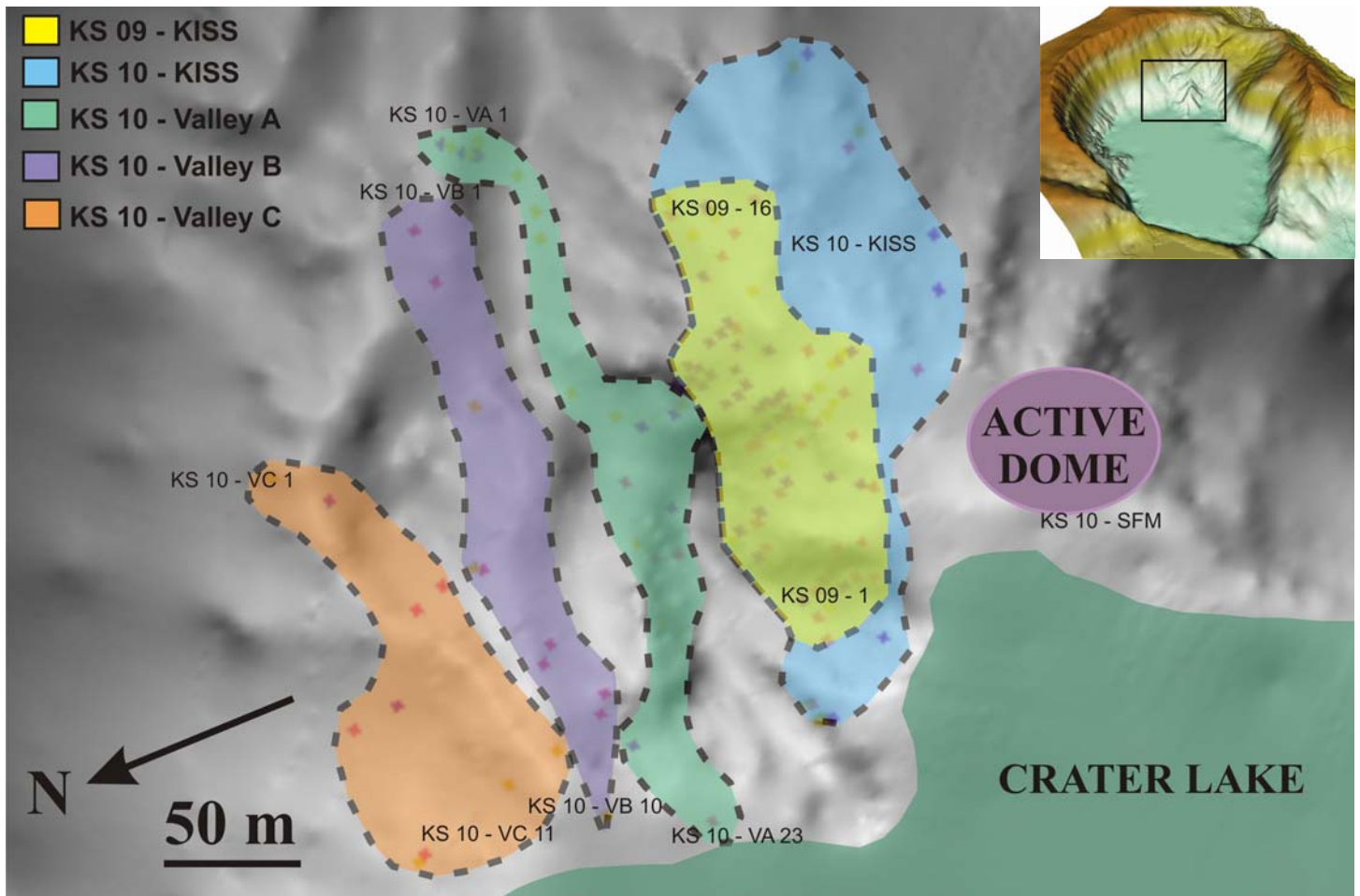


Fig. 1. Shaded relief map showing the sample locations. Yellow represents samples taken from the KISS valley in 2009 and blue, green, purple, and orange are samples taken in 2010 from the KISS, A, B, and C valleys, respectively. A grid system was used to collect the samples in 2009. The first row in the grid, i.e. KS09-1, is at the roughly westernmost point and the last row, i.e. KS09-16 is at the roughly easternmost point. The grid is further broken into columns. There is a base line that trends 163° , all samples here are labeled A. To the north of A, the samples increase in alphabetical order, e.g. from A to H; at the southernmost sample point from A, this sample is called Z and the samples increase alphabetically until reaching the baseline, e.g. from Z to S. The samples in the KISS area from 2010 do not have any particular sampling trend, however those from Valley A, B and C were collected from roughly east to west. The inset in the upper right corner is a digital elevation model (DEM) of the Kawah Ijen crater. The black box in the DEM indicates the study area.

Excimer Resolution M-50 laser, respectively). Results of X-ray diffraction analyses were utilized primarily to determine the nature and proportions (Rietveld analysis using TOPAS software) of the alteration minerals in order to create a three-dimensional model of the alteration center; in many cases thin sections could not be made of these samples (the material was too powdery). Pyrite crystals were analyzed using LA-ICPMS for gold and other trace base in cases where concentrations were below the level of detection of the electron microprobe.

1.10. Thesis organization

This thesis is divided into four chapters: a general introduction, geologic background, a manuscript describing the results of the research, and a general conclusion. The general introduction discusses epithermal systems and details the current hypotheses and debates on the formation of the alteration and mineralization in high sulfidation epithermal systems. The manuscript has been prepared for publication in a peer-reviewed journal and highlights the debates concerning the formation and mineralization of high sulfidation epithermal systems, details the results of the research and provides a genetic model for the formation of the alteration and associated pyrite mineralization in the crater of Kawah Ijen Volcano. Appendices follow the conclusion.

1.11. References

- Archibald, S.M., Migdisov, A.A., Williams-Jones, A.E., 2001. The stability of Au-chloride complexes in water vapor at elevated temperatures and pressures. *Geochimica et Cosmochimica Acta*. 65, 4413-4423.
- Archibald, S.M., Migdisov, A.A., Williams-Jones, A.E., 2002. An experimental study of the stability of copper chloride complexes in water vapor at elevated temperatures and pressures. *Geochimica et Cosmochimica Acta*. 66, 1611-1619.
- Arribas, A. Jr., 1995. Characteristics of high sulfidation epithermal deposits, and their relation to magmatic fluid. In: Thompson JFH (ed) *Magma, fluids and ore deposits*. Mineral Association of Canada Short Course Notes. 23: 419-454.
- Benning, L.G., Seward, T.M., 1994. Hydrosulphide complexes of gold (I) at high pressures and temperatures: equilibrium and kinetic problems. *Mineralogy Magazine*. 58A, 75-76.
- Benning, L.G., Seward, T.M., 1995. AuHSO_4^- An important gold-transporting complex in high temperature hydrosulphide solutions. *Water-Rock Interaction-8*. (ed. Y.K. Kharaka, O.V. Chudakov), 783-786. Balkema Press.
- Benning, L.G., Seward, T.M., 1996. Hydrosulphide complexing of Au (I) in hydrothermal solutions from 150-400 °C and 500-1500 bar. *Geochimica et Cosmochimica Acta*. 60, 1849-1871.
- Berger, B.R., Henley, R.W., 2011. Magmatic-vapor expansion and the formation of high sulfidation gold deposits: Structural controls on hydrothermal alteration and ore mineralization. *Ore Geology Reviews*. 39, 75-90.
- Bernard, A., 1985. Les mécanismes de condensation des gaz volcaniques-chimie minéralogie et équilibre des phases condensées majeures et mineures: Unpublished Ph.D. thesis, University of Brussels, Belgium 195 p.
- Boyle, R.W., 1979. The geochemistry of gold and its deposits. *Geologic Survey of Canada Bulletin*. 280, 30-32.
- Boyce, A.J., Fulignati, P., Sbrana, A., Fallick, A.E., 2007. Fluids in early stage hydrothermal alteration of high sulfidation epithermal systems: A view from the Vulcano active hydrothermal system (Aeolian Island, Italy). *Journal of Volcanology and Geothermal Research*. 166, 76-90.

- Burnham, C.W., 1979. Magmas and hydrothermal fluids. In: H.L. Barnes, Editor, *Geochemistry of Hydrothermal Ore Deposits* (2nd ed.), John Wiley and Sons, New York, pp. 71-136.
- Burnham, C.W., Ohmoto, H. Late Magmatic and Hydrothermal Processes in Ore Formation, 1981. In: *Mineral Resources: Genetic Understanding for Practical Applications*; National Academy Press, Washington, D.C. 1981 pp. 62-73..
- Cabri, L.J., Chryssoulis, S.L., de Villiers, J.P.R., Laflamme, J.H.G., Buseck, P.R., 1989. The nature of “invisible” gold in arsenopyrite. *Canadian Mineralogist*. 27, 353-362.
- Chouinard, A., Paquette, J., Williams-Jones, A.E., 2005a. Crystallographic controls on trace-element incorporation in auriferous pyrite from the Pascua epithermal high sulfidation deposit, Chile-Argentina. *The Canadian Mineralogist*. 43, 951-963.
- Cook, N.J., Chryssoulis, S.L., 1990. Concentrations of “invisible” gold in the common sulfides. *Canadian Mineralogist*. 28, 1-16.
- Cooke, D.R., Simmons, S.F., 2000. Characteristics and Genesis of Epithermal Gold Deposits. *Reviews in Economic Geology: Gold in 2000*. 13, 221-244.
- Eastoe, C.J., 1982. Physics and chemistry of the hydrothermal system at the Panguna porphyry copper deposit, Bougainville, Papua New Guinea. *Economic Geology*. 77, 127-153.
- Fleet, M.E., Chryssoulis, S.L., MacLean, P.J., Davidson, R., Weisener, C.G., 1993. Arsenian pyrite from gold deposits: Au and As distribution investigated by SIMS and EMP, and color staining and surface oxidation by XPS and LIMS. *Canadian Mineralogist*. 31, 1-17.
- Fleet, M.E., Mumin, A.H., 1997. Gold-bearing arsenian pyrite and marcasite and arsenopyrite from Carlin Trend gold deposits and laboratory synthesis. *American Mineralogist*. 82, 182-193.
- Gammons, C.H., Williams-Jones, A.E., 1997. Chemical Mobility of Gold in the Porphyry-Epithermal Environment. *Economic Geology*. 92, 45-59.
- Gemmell, J.B., 1987. Geochemistry of metallic trace elements in fumarole condensates from Nicaraguan and Costa Rican volcanoes. *Journal of Volcanological and Geothermal Research*. 33, 161-181.

- Giggenbach, W.F., 1987. Redox processes governing the chemistry of fumarolic gas discharges from White Island, New Zealand. *Applied Geochemistry*. 2, 143-161.
- Giggenbach, W.F., Matsuo, S., 1991. Evaluation of results from the second and third IAVCEI field workshops on volcanic gases, Mt. Usu, Japan, and White Island, New Zealand. *Applied Geochemistry*. 7, 125-141.
- Gray, J.E., Coolbaugh, M.F., 1994. Geology and geochemistry of Summitville, Colorado; an epithermal acid sulfate deposit in a volcanic dome. *Economic Geology*. 89, 1906-1923.
- Groves, D.I., Beirlein, F.P., 2007. Geodynamic settings of mineral deposit systems. *Journal of the Geological Society*. 164, 19-30.
- Halmer, M.M., Schminke, H.U., Graf, H.F., 2002. The annual volcanic gas input into the atmosphere, in particular into the stratosphere: a global data set for the past 100 years. *Journal of Volcanology and Geothermal Research*. 115, 511-528.
- Hayaba, D.O., Bethke, P.M., Heald, P., Foley, N.K., 1985. Geologic, mineralogic and geochemical characteristics of volcanic-hosted epithermal precious-metal deposits. *Reviews in Economic Geology*. 2, 129-168.
- Hayashi, K., Ohmoto, H., 1991. Solubility of gold in NaCl- and H₂S-bearing aqueous solutions at 250-350 °C. *Geochimica et Cosmochimica Acta*. 55, 2111-2126.
- Heald, P., Foley, N.K., Hayaba, D.O., 1987. Comparative Anatomy of Volcanic-Hosted Epithermal Deposits: Acid-Sulfate and Adularia-Sericite Types. *Economic Geology*. 82, 1-26.
- Hedenquist, J.W., Simmons, S.F., Giggenbach, W.F., Eldridge, C.S., 1993. White Island, New Zealand, volcanic-hydrothermal system represents the geochemical environment of high sulfidation Cu and Au ore deposition. *Geology*. 21, 731-734.
- Hedenquist, J.W., Aoki, M., Shinohara, H., 1994. Flux of volatiles and ore-forming metals from the magmatic-hydrothermal system of Satsuma Iwojima volcano. *Geology*. 22, 585-588.
- Hedenquist, J.W., Lowenstern, J.B., 1994. The role of magmas in the formation of hydrothermal ore deposits. *Nature*. 370, 519-527.

- Hedenquist, J.W., Arribas, A., Jr., Reynolds, T.J., 1998. Evolution of an Intrusion-Centered Hydrothermal System: Far Southeast-Lepanto Porphyry and Epithermal Cu-Au Deposits, Philippines. *Economic Geology*. 93, 373-404.
- Hedenquist, J.W., Arribas, A.R., Gonzalez-Urien, E., 2000. Exploration for epithermal gold deposits. *Reviews in Economic Geology*. 13, 245-277.
- Heinrich, C.A., Ryan, C.G., Mernagh, T.P., Eadington, P.J., 1992. Segregation of ore metals between magmatic brine and vapor; a fluid inclusion study using PIXE microanalysis. *Economic Geology*. 87, 1566-1583.
- Heinrich, C.A., Günther, D., Audétat, A., Ulrich, T., Frischknecht, R., 1999. Metal fractionation between magmatic brine and vapor, determined by microanalysis of fluid inclusions. *Geology*. 27, 755-758.
- Heinrich, C.A., 2007. Fluid-Fluid Interactions in Magmatic-Hydrothermal Ore Formation. *Reviews in Mineralogy & Geochemistry*. 65, 363-387.
- Hengeveld, G.J.N., 1920. De mogelijkheid en de plaats van den bouw van een nieuwe sluis bij het kratemeer Kawah Idjen, in: Mededelingen en rapporten van het departement der burgelijke openbare werken; Geologische onderzoeken ten behoeve van 's lands waterstaat-, gewestelijke- en gemeentewerken in Nederlandsch-Indie, Weltevreden.
- Henley, R.W., McNabb, A., 1978. Magmatic vapor plumes and ground-water interaction in porphyry copper emplacement. *Economic Geology*. 73, 1-20.
- Henley, R.W., Berger, B.R., 2011. Magmatic-vapor expansion and the formation of high sulfidation gold deposits: Chemical controls on alteration and mineralization. *Ore Geology Reviews*. 39, 63-74.
- Jannas, R.R., Bowers, T.W., Petersen, U., Beane, R.E., 1999. High sulfidation deposit types in the El Indio district, Chile, in Skinner, B.J., ed. *Geology and ore deposits of the central Andes: Economic Geology Special Volume 7*, p. 219-266.
- Kesler, S.E., 2005. Ore-Forming Fluids. *Elements*. 1, 13-18.
- Krauskopf, K.B., 1957. Separation of manganese from iron in sedimentary processes. *Geochimica et Cosmochimica Acta*. 12, 61-84.
- Krauskopf, K.B., 1964. The possible role of volatile metal compounds in ore genesis. *Economic Geology*. 59, 22-45.

- Le Guern, F., 1988. Ecoulements gazeux reactifs à hautes températures, mesures et modelisation. Unpublished Ph.D. thesis, University of Paris, 314 p.
- Mavrogenes, J., Henley, R.W., Reyes, A., Berger, B., 2010. Sulfosalt melts: evidence of high-temperature vapor transport of metals in the formation of high sulfidation lode gold deposits. *Economic Geology*. 105, 257-262.
- Menyailov, I.A., Nikitina, L.P., 1980. Chemistry and metal contents of magmatic gases: The new Tolbachik volcanoes gas (Kamchatka). *Bulletin of Volcanology*. 43, 197-207.
- Palmer, S., 2009. Hydrogeochemistry of the upper Banyu Pahit River valley, Kawah Ijen volcano, Indonesia. Unpublished M.Sc. Thesis, McGill University.
- Pan, P., Wood, S.A., 1994. The solubility of Pt and Pd sulfides and Au metal in bisulfide solutions. II. Results at 200-350 C and at saturated vapour pressure. *Mineral Deposita*. 29, 373-390.
- Renders, P.J., Seward, T.M., 1989. The stability of hydrosulido- and sulphide complexes of Au (I) and Ag (I) at 25 C. *Geochimica et Cosmochimica Acta*. 53, 244-253.
- Reynolds, T.J., Beane, R.E., 1985. Evolution of hydrothermal fluid characters at the Santa Rita, New Mexico, porphyry copper deposit. *Economic Geology*. 80, 1328-1347.
- Ruggieri, G., Lattanzi, P., Luxoro, S.S., Dessl, R., Benvenuti, M., Tanelli, G., 1997. Geology, Mineralogy, and Fluid Inclusion Data of the Furtei High sulfidation Gold Deposit, Sardinia, Italy. *Economic Geology*. 92, 1-19.
- Seward, T.M. 1973. Thio complexes of gold in hydrothermal ore solutions. *Geochimica et Cosmochimica Acta*. 37, 379-399.
- Sillitoe, R.H., 1989. Gold deposits in Western Pacific island arcs: The magmatic connection. *Economic Geology Monograph*. 6, 274-291.
- Shenberger, D.M., Barnes, H.L., 1989. Solubility of gold in aqueous sulfide solutions from 150 to 350 °C. *Geochimica et Cosmochimica Acta*. 53, 269-278.
- Stefánsson, A., Seward, T.M., 2004. Gold (I) complexing in aqueous sulphide solutions to 500 °C at 500 bar. *Geochimica et Cosmochimica Acta*. 68, 4121-4143.
- Steven, T.A., Ratte, J.C., 1960. Geology and ore deposits of the Summitville district, San Juan Mountains, Colorado. U.S. Geological Survey Professional Paper 343, 70 p.
- Stoffregen, R., 1987. Genesis of Acid-Sulfate Alteration and Au-Cu-Ag Mineralization at Summitville, Colorado. *Economic Geology*. 82, 1575-1591.

- Sourirajan, S., Kennedy, G.C., 1962. The system H₂O-NaCl at elevated temperatures and pressures. *American Journal of Science*. 260, 115-141.
- Symonds, R.B., Rose, W.I., Reed, M.H., Lichte, F.E., Finnegan, D.L., 1987. Volatilization, transport and sublimation of metallic and non-metallic elements in high temperature gases at Merapi Volcano, Indonesia. 51, 2083-2101.
- Symonds, R.B., Rose, W.I., Bluth, G.J.S., Gerlach, T.M., 1994. Volcanic-gas studies; methods, results, and applications. *Reviews in Mineralogy and Geochemistry*. 30, 1-66.
- Taran, Y.A., Hedenquist, J.W., Korzhinsky, M.A., Tkachenko, S.I., Shmulovich, K.I., 1995. Geochemistry of magmatic gases from Kudryavy volcano, Iturup, Kuril Islands: *GEochimica et Cosmochimica Acta*. 59, 1749-1761.
- Taran, Y.A., Bernard, A., Gavilanes, J-J., Africano, F., 2000. Native gold in mineral precipitates from high-temperature volcanic gases of Colima volcano, Mexico. *Applied Geochemistry*. 15, 33-346.
- Tosdal, R.M., Dilles, J.H., Cooke, D.R., 2009. From Source to Sinks in Auriferous Magmatic-Hydrothermal Porphyry and Epithermal Deposits. *Elements*. 5, 289-295.
- van Hinsberg, V., Berlo, K., van Bergen, M., Williams-Jones, A., 2010a. Extreme alteration by hyperacidic brines at Kawah Ijen volcano, East Java, Indonesia: I. Textural and mineralogical imprint. *Journal of Volcanology and geothermal Research*. 198, 253-263.
- van Hinsberg, V., Berlo, K., Sumarti, S., van Bergen, M., Williams-Jones, A., 2010b. Extreme alteration by hyperacidic brines at Kawah Ijen volcano, East Java, Indonesia: II: Metasomatic imprint and element fluxes. *Journal of Volcanology and Geothermal Research*. 196, 169-184.
- Vigouroux-Caillibot, N., 2011. Tracking the evolution of magmatic volatiles from the mantle to the atmosphere using integrative geochemical and geophysical methods. Unpublished Ph.D. thesis, Simon Fraser University.
- Voudouris, P.G., 2011. Conditions of formation of the Mavrokoryfi high sulfidation epithermal Cu-Ag-Au-Te mineralization (Petrota Graben, NE Greece). *Mineralogy and Petrology*. 101, 97-113.

- Wahrenberger, C., Seward, T.M., Dietrich, V., 2002. Volatile trace element transport in high temperature gases for Kudriavy volcano (Iturup, Kurile Islands, Russia). *Geochemical Society Special Publication* 7, 307-327.
- White, N.C., Hedenquist, J.W., 1995. Epithermal gold deposits: styles, characteristics and exploration. *SEG Newsletter*. 23, 9-13.
- White, D.E., 1981. Active geothermal systems and hydrothermal ore deposits. *Economic Geology* 75th Anniversary, 392-423.
- White, N.C., and Herrington, R.J., 2000, Mineral deposits associated with volcanism, *in* Sigurdsson, H., et al., eds., *Encyclopedia of volcanoes*: San Diego, Academic Press, p. 897–912.
- Williams-Jones, A.E., Migdisov, A.A., Archibald, S.M., Xiao, Z., 2002. Vapor-transport of ore metals. *In: Water-rock Interaction, Ore Deposits, and Environmental Geochemistry: A Tribute to David A. Crear*. Hellmann, R., Wood, S.A. (eds). The Geochemical Society. Special Publication No. 7, 279-305.
- Williams-Jones, A.E., Heinrich, C.A., 2005. Vapor Transport of Metals and the Formation of Magmatic-Hydrothermal Ore Deposits. *Economic Geology* 100th Anniversary, 1287-1312.
- Williams-Jones, A.E., Bowtell, R.J., Migdisov, A.A., 2009. Gold in Solution. *Elements*. 5, 281-287.
- Yudovskaya, M.A., Distler, V.V., Chaplygin, I.V., Mokhov, A.V., Trubkin, N.V., Gorbacheva, S.A., 2006. Gaseous transport and deposition of gold in magmatic fluid: evidence from the active Kudryavy volcano, Kurile Islands. 40, 828-848.
- Zotov, A.V., Baranova, N.N. The solubility of Au₂S and AuAgS in near-neutral sulphide solutions at temperatures of 25 and 80°C and pressures of 1 and 500 bars. *In: Y.K. Kharaka and O.V. Chudaev, Editors, Water-Rock Interaction-8*, Balkema Press (1995), pp. 773–776.

Geologic Setting

Kawah Ijen is an active stratovolcano in the Ijen Volcanic Complex, East Java, Indonesia. The volcano is situated on the western flank of Gunung Merapi, an inactive stratovolcano on the rim of the caldera. The crater of Kawah Ijen volcano is host to an active solfatara, the world's largest hyperacidic crater lake (pH ~0.5), thermal springs that emerge directly from the magmatic-hydrothermal system and a high sulfidation epithermal alteration center.

2.1. Geotectonic setting of Indonesia

Indonesia is situated at a tectonic boundary marking the collision of the northward moving Indo-Australian plate with the Eurasian plate (Fig 1; Handley et al., 2007). The result of this collision was the creation of the Quaternary Sunda Arc (Handley et al., 2007; Katili, J.A., 1989). The Indo-Australian-Eurasian plate boundary is a complex tectonic interface, containing multiple subduction zones that span a distance of over 8,000 km, from the Andaman Sea off the coast of Myanmar to the island of Wetar, Indonesia, and travel around the southern coasts of Sumatra and Java, Indonesia (Katili, 1989). Southwest of Sumatra and Java, the Indian oceanic plate is being subducted beneath the Sundaland continental craton and eastwards beneath oceanic crust east of Java. In the southeast, the Australian continental plate is being subducted beneath the oceanic crust of the Banda Sea (Katili, 1975).

There is a 6,000 to 7000 m deep trench off the coast of Java that is filled by thick packages of sediment derived from oceanic sediments and the accretionary wedge (Hamilton, 1979; Fig. 2). The Indo-Australian plate dips from the trench at a shallow angle (~22.7°; Whittaker et al., 2007) for 200 km, then much more steeply (~65°; Hamilton, 1979) below Java. The active volcanic arc, the Sunda Arc, occurs north of the forearc basin. This zone forms the backbone of Sumatra and Java and makes up most of the islands east of Java (Moore et al., 1980). The volcanism in this zone is most likely

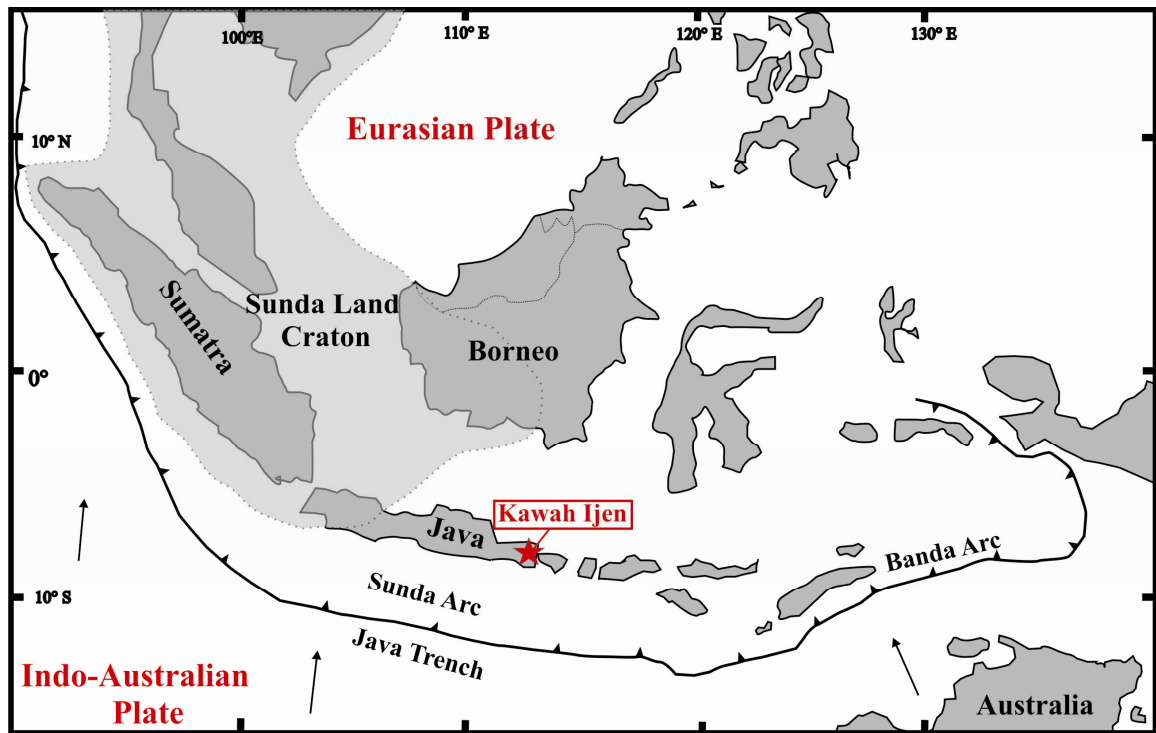


Fig. 1. Tectonic setting of Indonesia (modified from Hoffmann-Rothe et al., 2001), showing the location of Kawah Ijen volcano (red star). Black arrows show the directions of plate movement. The dashed outline of the 'Sunda Land Craton' indicates possible extent of continental lithospheric basement (Hamilton, 1979).

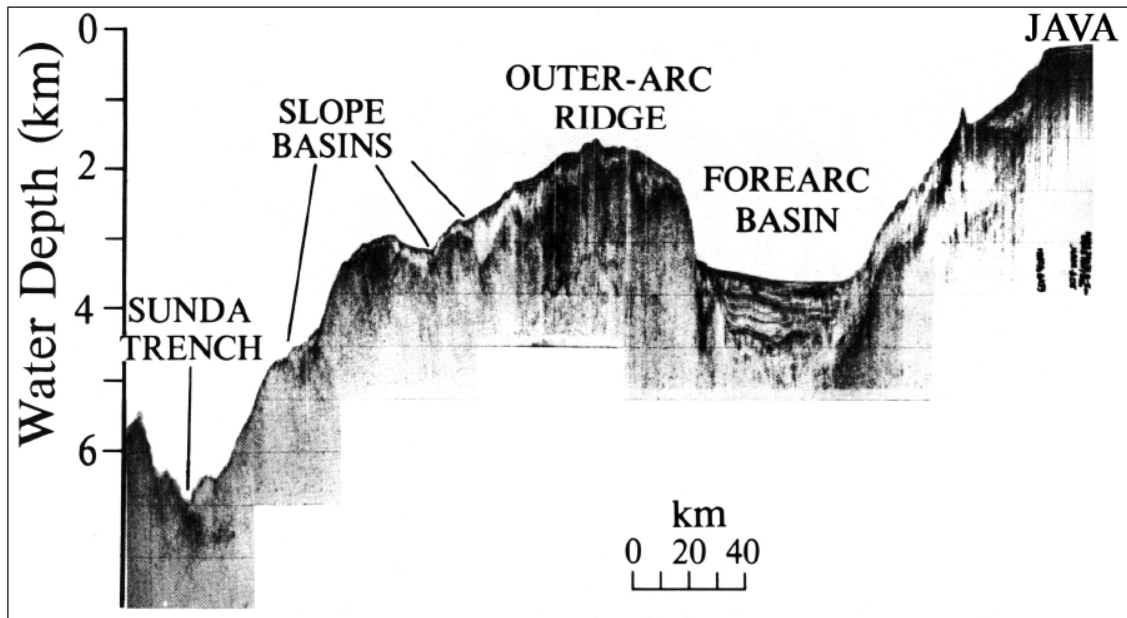


Fig. 2. A single-channel analog seismic reflection profile from north (right) to south (left) across the subduction zone south of Central Java from Moore et al. (1980). The Sunda trench is shown on the left bordered by the accretionary wedge, which is formed by the accumulation of sediments scraped from the subducting plate. To the south of the accretionary wedge, is the forearc basin, which is filled with layered Paleogene to recent sediments. The basin is bordered in the south by the slopes of the island of Java.

being caused mainly by melting of the asthenospheric mantle above the subducting plate, triggered by the release of fluids from the dehydrating down-going slab (Simandjuntak and Barber, 1996). However, the presence of adakites in both western and eastern Java supports slab melting as another magma source (Setijadji et al., 2006).

Magmatism on Java is the result of the subduction of oceanic crust under thick and old continental crust (Katili, 1975); it is more basic than on Sumatra because of the thinning of the underlying crust towards Bali (Edwards et al., 1994). The compositional affinity of the volcanics on Java has shifted from island arc tholeiite and minor shoshonite (Tertiary volcanic arc) to calc-alkaline and minor tholeiite (Quaternary Sunda Arc; Soeria-Atmadja et al., 1994). Quaternary volcanoes located behind the volcanic front are mostly alkalic potassic to ultrapotassic in composition (Soeria-Atmadja et al., 1994). The trend in increasing alkalinity is inferred to have been the result of the diminishing influence of the slab (Edwards et al., 1994) combined with differences in mantle sources or partial melting (Hoogewerff, 1999; 1997). Despite their different composition, there is no clear tectonic association for the rear-arc, alkaline volcanoes, but they are likely associated with some degree of extension that generates decompression-driven melting. Thus, the magmas in Java are not clearly calc-alkaline because melting is a lot drier in the rear-arc. The alkalinity of the magmas is dependent on the fertility of the mantle and the degree of partial melting (N. Vigouroux, pers. comm.).

East Java is underlain by oceanic crust, approximately 20 km-thick. The basement is Mesozoic to Cenozoic in age and is composed of calcareous sediments and basaltic and andesitic volcanic rocks (Hamilton, 1979). Before the Late Neogene, East Java was below sea-level, however, during this period there was a change in the tectonics of the region. The change from divergence to a compressional convergence resulted in the folding of Cenozoic deposits, and uplifted eastern Java above sea-level (Simandjuntak and Barber, 1996). The Ijen Caldera Complex is located on the eastern tip of Java and is part of the present Sunda volcanic arc.

2.2. *Ijen Caldera Complex*

The Ijen Caldera Complex (ICC) is located on the eastern tip of Java, Indonesia between the cities of Banyuwangi, Situbondo and Jember (Fig. 3). The ICC is a 20 km-wide, circular caldera depression that was formed over 50,000 years ago by the collapse of the Ijen stratovolcano (Kemmerling, 1921; van Bemmelen, 1949; Sitorus, 1990). The caldera is bordered by a steep escarpment to the north (Kendeng caldera wall) and volcanic peaks in the north, east and south (Gunungs Ringgih, Merapi, Ranteh, and Djampit respectively). Within the caldera, there are lacustrine sediment deposits in the north (a large lake seems to have occupied the entire north half of the caldera; van Hinsberg et al., 2010a), and plains and smaller volcanic vents that form a roughly east-west lineament through the central-southern half of the caldera.

There are two types of volcanoes in the ICC, caldera rim and intracaldera volcanoes. The caldera rim volcanoes erupt high-Ca magmas of basalt to basaltic andesite composition and the intracaldera volcanoes erupt low-Ca magmas of basaltic andesite to dacite composition. The locations of these volcanoes, i.e., along the caldera rim and on a NE-SW lineament through the caldera, suggest that there are structural controls of magma ascent in the caldera, e.g., ring fractures as magma pathways for the caldera rim and the NE-SW lineament through the caldera along which the intracaldera volcanoes are located. This is further supported by the distinctly different fractionation trends in Ca, which suggest spatial variations in chemistry within the volcanic complex that might be linked to sub-volcanic structure or to differences in the amount of plagioclase fractionation (Handley et al., 2007). Kawah Ijen sits at the intersection of the caldera rim and intracaldera lineation and could tap both shallow and deeply ponded magmas. Indeed, it erupts both high- and low-Ca magmas and, as there is no temporal division in the production of high-Ca and low-Ca lava types at Kawah Ijen (Handley et al., 2007) and no evidence for physical mixing and mingling (Berlo, 2001), this implies separate magmatic pathways for magmas erupted from different depths. Low MgO, and Ni and Cr abundances in ICC volcanic rocks indicate that they are not primary mantle melts, and that magma compositions were modified en route to the surface (Handley et al., 2007).

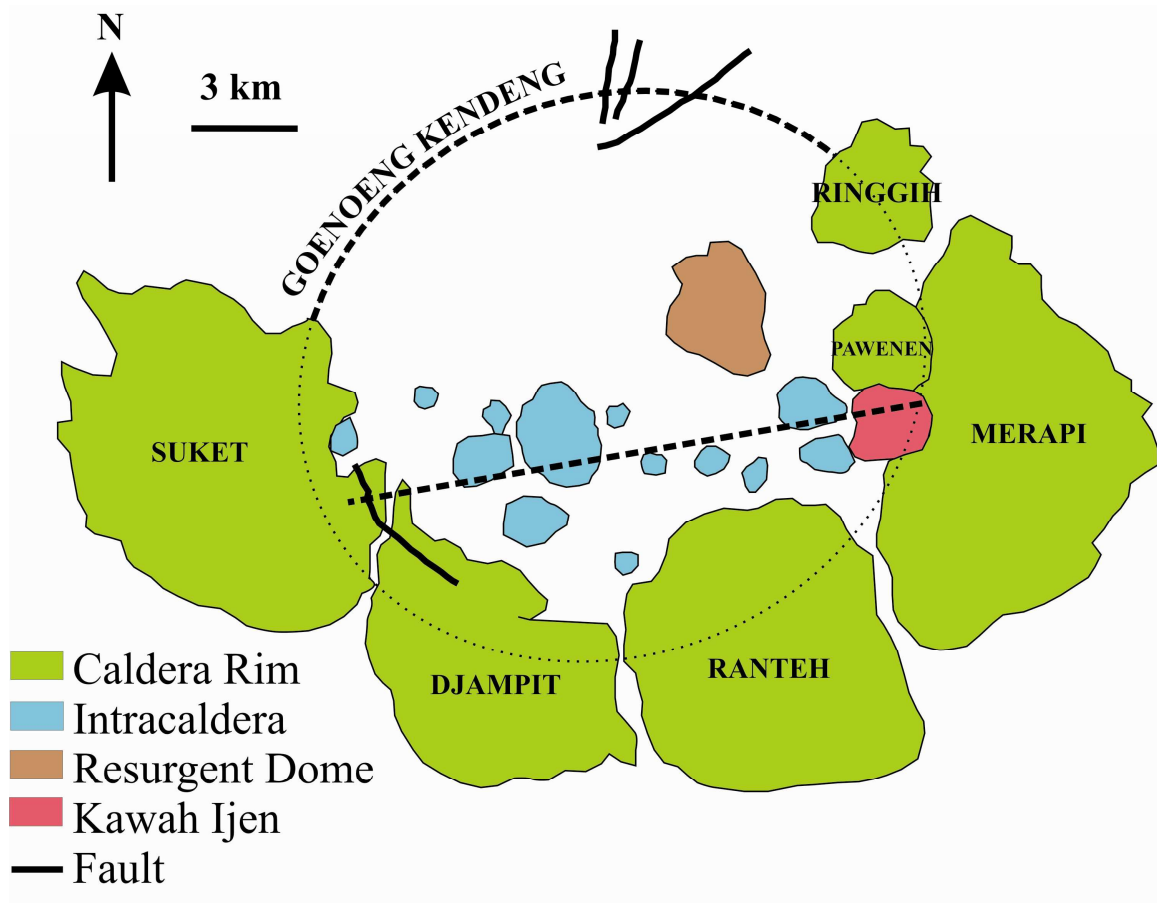


Fig. 3. The distribution of volcanic in and adjacent to the Ijen Caldera. The dashed line highlights the roughly east-west distribution of the intracaldera volcanoes. This also represents a trend of decreasing age of the volcanism. The dashed line in the north that outlines the caldera represents the hypothesized location of the base of the pre-caldera cone (modified from Berlo, 2001).

Gunung Blau, located just to the north of the lineament, is the oldest intracaldera volcano and is thought to represent a separate stage of activity, possibly a resurgent dome to the old Ijen volcano (Berlo, 2001). From east to west, the vents comprise: Kawah Ijen and G. Papak, G. Widadern, G. Telagweru, G. Kukusan, G. Geleman, G. Genteng, G. Pendil, G. Anyar, G. Lingker, G. Mlaten, and G. Cemara. Of these, G. Widodaren, Kawah Ijen, G. Pawenen, and G. Papak are located on the northwestern flank of G. Merapi. Kawah Ijen is located at the junction between the rim volcanoes and the intracaldera volcanoes on the flank of G. Merapi (a caldera rim volcano).

2.3. Kawah Ijen Volcano

Kawah Ijen is situated on the northwest flank of G. Merapi. Continuing down the northwest slope, G. Papak, G. Widodaren and G. Pawenen are clustered about the base of Kawah Ijen. The summit of Kawah Ijen is 2386 m.a.s.l. and the crater rim, on average, is approximately 2340 m.a.s.l. (van Hinsberg, 2001). The summit (Fig. 4) consists of two interlocking craters (van Hinsberg et al., 2010a) and measures approximately 1150 m by 950 m. The crater contains an active degassing dome, the remnants of an older dome and a turquoise-colored lake with dark yellow patches of precipitated sulfur at lake level (van Hinsberg et al., 2010b). The lake is located approximately 150 m below the summit of the volcano, except at its western side where the crater wall extends almost to lake level (van Hinsberg et al., 2010a). On the western edge of the crater, there is a small shore where a Dutch company built a dam in the early 20th century to regulate the outflow of the lake to prevent the acid lake water from destroying their crops (van Hinsberg, 2001).

The formation of present-day Kawah Ijen was controlled by several events. The first was the partial destruction of its twin, G. Merapi. Kawah Ijen formed on the destroyed flank of G. Merapi on the inside of the ICC when that section of G. Merapi was partly destroyed during the major caldera collapse event (G. Merapi formed before the main collapse event; Kemmerling, 1921). The growth of Kawah Ijen occurred in two distinct phases, namely a constructive phase, and destructive phase during which the top of the volcano was blown off. The depression in the crater made during the destructive



Fig. 4. The summit of Kawah Ijen. On the far left is the degassing solfatara (yellow); the alteration center is immediately adjacent to the right of it. The green body is the hyperacidic crater lake. The steam over the lake is from a vent on the lake floor.

phase allowed for the accumulation of meteoric water and the formation of a lake (Hengeveld, 1920). There have been at least two large eruptions in the history of Kawah Ijen as evidenced by field observations of the two interlocking craters.

Kawah Ijen is a composite cone of basaltic-andesite to dacitic composition and is built of alternating layers of basaltic and andesitic lava flows, lahar and pyroclastic flows, and scoria deposits (Whitford et al., 1979; Delmelle et al., 1994; van Hinsberg et al., 2010a). Lava flows are generally half a meter to several meters thick and are parallel to the current slope of the volcano (Delmelle et al., 1994). At present, the crater is occupied by a lake; the more recent phreatic and air fall deposits are the products of eruptions centered beneath the lake. There are poorly-sorted phreatic deposits on the high, outer slopes of the crater, including ash, rock, lava fragments and sulfur particles. The crater also contains four valleys on the southeastern lake shore that host an active solfatara, as well as an exposed feeder system of an older solfatara that was destroyed during an eruption in 1817 (the crater lake was also completely expelled during this eruption). This feeder system is exposed approximately 150 meters below the old surface of the crater occupied by the pre-1817 solfatara (since 1817, activity has shifted approximately 50 m to the southeast where a new solfatara is currently degassing and large quantities of native sulfur are precipitating). Sharing the same location are basaltic lava and epiclastic flows. These rock units have variably been altered and some pyritized. This alteration started developing a long time before the 1817 eruption (conceivably thousands of years earlier) and was exposed following the 1817 eruption. Additionally, there is also extensive silicification, as well as widespread pyrite veining. The mineralogy of the alteration center (i.e., alunite, kaolinite, pyrite, and silica) is the same as that found in high sulfidation epithermal systems.

In addition to the 1817 eruption, there have been numerous other historic eruptions at Kawah Ijen. The other relatively large phreato-magmatic eruptions took place in 1796 (Hengeveld, 1920). Also, there was reported boiling of the lake and a release of thick clouds of white smoke in 1789 and an eruption in 1952 that caused an ash and a sulfur cloud to rise 100 m above the crater. Minor phreatic eruptions occurred in 1917, 1936, and five times from 1990 to 1999 (Hengeveld, 1920; Smithsonian Institute,

2000). Current volcanic activity is expressed by the actively degassing fumaroles (white to yellow fumes). Other indications of activity include the degassing hyperacidic lake and acid-sulfate springs discharging from the volcano's hydrothermal system (van Hinsberg et al., 2010a, b).

On the three kilometer path leading from the base of Kawah Ijen to its summit, there are exposures of layered pyroclastics, scoria deposits, phreatic and phreatomagmatic deposits, and lava flows. Near the summit of the volcano, some of these units display evidence of the acid-sulfate alteration that characterizes high-sulfidation epithermal systems. At the summit, there is second path that leads to the crater floor, some 150m below the elevation of the summit. The path terminates on a flat plain (southeastern shore of the lake) that is bordered by a large hill to the north interpreted to represent the feeder system to the solfatara that erupted in 1817, and an active solfatara to the southeast. The lithologies in the crater include: acid-sulfate altered rock, pyroclastics, lacustrine sediments, debris flows, lava flows, epiclastic flows, and pillow lavas.

The location of the active solfatara (2150 m.a.s.l.) provides evidence for the westward migration of the system, relative to the location of the pre-1817 solfatara. The active solfatara is approximately 20m high and 100m wide, and is covered completely in native sulfur, which gives it a dull yellow color; its fumaroles emit large masses of volcanic gas. The resulting plume transports at least 300 tonnes of S_{total} from the plume daily (Vigouroux et al., 2009). The limits of the solfatara are the crater wall, the lake and a deep gully in front of it. It is dome-shaped, however because it grows against the crater wall, it is more accurately described as a half dome. A large sulfur mining operation has taken place in the crater since the late 1700s. Each day approximately 50 to 100 miners carry between one and two loads of sulfur weighing between 60 and 90 Kg from the crater. This sulfur is condensed from the fumarolic gases along pipes that lead to the base of the dome where liquid sulfur accumulates and solidifies before being broken up into pieces for transport to the base of the volcano.

The active dome is the locus of strong fumarolic activity and precipitation of large amounts of native sulfur. A thin crust of basaltic-andesite composition lies beneath the native sulfur. This crust is the formed by wall rocks falling onto the active dome. Within

this crust, rhyolite globules are observed. As there is no rhyolite in the wall rocks of the volcano (Berlo, 2001), van Hinsberg et al., (2010b) proposed that the dome is rhyolitic in composition. Temperatures of the gases emerging from the dome range from 200 to greater than 600 °C (van Hinsberg et al., 2010b; Vigouroux et al., 2007; Vigouroux et al., 2009). Gas sampling and analysis confirms that Kawah Ijen is emitting H₂O, CO₂, SO₂, H₂S, HCl, and HF¹. Condensate data collected from the fumaroles show that Cu, Te, As, and Se are fluxing daily from the volcano.

North of the active dome the roots of the pre-1817 hydrothermal system are exposed. This feature is referred to as the ‘alteration center’ because of the extensive acid-sulfate alteration of the rocks that occurred before the 1817 eruption and has continued since (the active solfatara is experiencing similar alteration; this study). The alteration center comprises four valleys, the first of which shares the same valley as the active solfatara. The alteration mineralogy is characterized by alunite, natroalunite, kaolinite, dickite, pyrite, gypsum, barite, cristobalite, tridymite, and quartz (this study). The walls of the valleys are very steep and range from a brownish-yellow color to white; these rocks are typically composed of alunite or natroalunite, however kaolinite and dickite are also found; there are rare alunite veins. Additionally, there are black veins and massive black sections of alteration that are composed almost entirely of pyrite. Pyrite veining is a common feature and in a few instances, pyrite-alunite haloes have been found surrounding them. There is also some gypsum veining, although this is found almost exclusively along the lake shore, and is likely due to interaction of the rocks with waters from the lake. On the floors of the valleys, there are large boulders of massive pyrite, vuggy silica, lake sediments, and blocks of altered rocks that provide evidence of another alteration unit from higher up in the crater that may have been destroyed in a debris avalanche or the last major eruption. The aforementioned debris flows lie disconformably on top of the acid sulfate alteration and host large blocks of alunite; this is further evidence for acid-sulfate alteration higher up in the crater. In that same location there could have been zone(s) of vuggy silica, based on the occurrence of two boulders of

¹ "Water-rich year" (2007): >96 wt% H₂O, <2 wt.% CO₂, <1 wt.% SO₂, virtually no H₂S, HCl and HF.
"CO₂-rich year" (2008): 70-75 wt.% H₂O, 18-21 wt.% CO₂, 2-3 wt.% SO₂, 2-4 wt.% H₂S, <0.1 wt.% HCl, <0.01 wt.% HF (unpublished data).

this material on the floor of Valley A. These valleys also contain basaltic lava, pillow lavas and epiclastic flows.

2.4. The hydrothermal system at Kawah Ijen

The magmatic-hydrothermal system at Kawah Ijen has been studied from a hydrogeologic perspective by Palmer (2009) and van Hinsberg et al. (2010a; 2010b). There are numerous surface manifestations of the system, e.g., actively degassing fumaroles on the solfatara, a very low pH river (Banyu Pahit), a hyperacidic crater lake, and three sets of springs discharging hyperacidic water on the western flanks of the volcano, one of which emerges directly from the hydrothermal system, rather than from seepage from the crater lake (Palmer, 2009).

The crater lake at Kawah Ijen represents the largest naturally-occurring body of hyperacid brine in the world (1500 x 900 m diameter by 180-200 m deep; Takano et al., 2004) and has a pH between -0.6 and 0.3 (Delmelle and Bernard, 2000; Neumann van Padang, 1951; Palmer, 2009) and TDS>100 g/kg (Delmelle and Bernard, 1994; 2000). The extremely low pH is the result of the semi-continuous condensation of sulfur-rich magmatic volatiles (SO₂, H₂S, HCl, HF) in the lake. However, the pH is also affected by seasonal rainwater recharge (Palmer, 2009); the bulk of the water is meteoric. The cation chemistry is controlled by the dissolution of rocks falling into the lake, whereas the anions are sourced by magmatic degassing (van Hinsberg, 2010a, b). The temperature of the lake ranges from 31 to 52 °C (this study).

2.5. References

- Berlo, K. The Magmatic Evolution of the Ijen Caldera Complex. Drs thesis (unpublished), Utrecht 2001.
- Delmelle, P., Bernard, A., Kusakabe, M., Fischer, T.P., Takano, B., 2000. Geochemistry of the magmatic-hydrothermal system of Kawah Ijen volcano, East Java, Indonesia. *Journal of Volcanology and Geothermal Research*. 97, 31-53.
- Delmelle, P., Bernard, A., 1994. Geochemistry, mineralogy, and chemical modeling of the acid crater lake of Kawah Ijen Volcano, Indonesia. *Geochimica et Cosmochimica Acta*. 58, 2445-2460.
- Edwards, C.M.H., Menzies, M.A., Thirlwall, M.F., Morris, J.D., Leeman, W.P., Harmon, R.S., 1994. The transition to potassic island arcs: the Ringgit-Besar complex, East Java, Indonesia. *Journal of Petrology*. 35, 1557-1595.
- Handley, H.K., MacPherson, C.G., Davidson, J.P., Berlo, K., Lowry, D., 2007. Constraining Fluid and Sediment Contributions to Subduction-Related Magmatism in Indonesia: Ijen Volcanic Complex. *Journal of Petrology*. 48, 1155-1183.
- Hamilton, W., 1979. Tectonics of the Indonesian Region. *Geological Survey Professional Paper*, 1078, Washington.
- Heald, P., Foley, N.K., Hayba, D.O., 1987. Comparative Anatomy of Volcanic-Hosted Epithermal Deposits: Acid-Sulfate and Adularia-Sericite Types. *Economic Geology*. 82, 1-26.
- Hengeveld, G.J.N., 1920. De mogelijkheid en de plaats van den bouw van een nieuwe sluis bij het kratemeer Kawah Idjen, in: Mededelingen en rapporten van het departement der burgerlijke openbare werken; Geologische onderzoeken ten behoeve van's lands waterstaat-, gewestelijke- en gemeentewerken in Nederlandsch-Indie, Weltevreden.
- Hoogewerff, J.A., van Bergen, M.J., Vroon, P.Z., Hertogen, J., Wordel, R., Sneyers, A., Nasution, A., Varekamp, J.C., Moens, H.L.E., Mouchel, D., 1997. U-series, Sr-Nd-Pb isotope and trace-element systematics across an active island arc-continent collision zone: Implications for element transfer at the slab-wedge interface. *Geochimica et Cosmochimica Acta*. 61, 1057-1072.

- Hoogewerff, J.A., 1999. Magma genesis and slab-wedge interaction across an island arc-continent collision zone, east Sunda Arc, Indonesia. Ph.D. Thesis University Utrecht, The Netherlands 178.
- Katili, J.A., 1975. Volcanism and Plate Tectonics in the Indonesia Island Arcs. *Tectonophysics*. 26, 165-188.
- Katili, J.A., 1989. Review of past and present geotectonic concepts of eastern Indonesia, in: J.E. von Hinte, T.C.E. van Weering, A.R. Fortuin, J.G. Baretta-Becker and J.H. Stel, *Geology and geophysics of the Banda arc and adjacent areas. I proceedings of the Snellius II Symposium*, *Netherlands Journal of Sea Research*. 24, 103-129.
- Kemmerling, G.L.L., 1921b. Het Idjen Hoogland de geologie en geomorphologie van den Idjen. Batavia. Dr. H. Woudstra, *Analyse van merkwaardige watersoorten op het Idjen-Hoogland*.
- Moore, G.F., J.R. Curray, D.G. Moore, and D.E. Karig, 1980. Variations in the Geological Structure along the Sunda Fore Arc, Northeastern Indian Ocean. *The Tectonic and Geologic Evolution of Southeast Asian Seas and Island*, D.E. Hayes (editor), *Geophysical Monograph* 23.
- Neumann van Padang, M., 1951. Catalogue of the active volcanoes of the world including solfatara fields, Pt. I, Indonesia: Naples, International Volcanologic Association, 271 p.
- Palmer, S. Hydrogeochemistry of the upper Banyu Pahit River valley, Kawah Ijen volcano, Indonesia. M.Sc. thesis (unpublished), McGill University 2009.
- Setijadji, L.D., Imai, B.A., Watanabe, C.K., 2006. Adakitic rocks from Sunda Arc, Indonesia. *Geophysical Research Abstracts*, Vol. 8.
- Simandjuntak, T.O., Barber, A.J. Contrasting tectonic styles in the Neogene orogenic belts of Indonesia, in: R. Hall and D. Blundell, *Tectonic evolution of Southeast Asia*, *Geological Society Special Publication* No. 106, 185-202, London 1996.
- Soeria-Atmadja, R., Maury, R.C., Bellon, H., Pringgoprawiro, H., Polve, M., Priadi, B., 1994. Tertiary magmatic belts in Java. *Journal of Southeast Asian Earth Sciences*. 9, 13-27.
- Takano, B., Suzuki, K., Sugimori, K., Ohba, T., Fazlullin, S.M., Bernard, A., Sumarti, S., Sukhyar, R., Hirabayashi, M., 2004. Bathymetric and geochemical investigation of

- Kawah Ijen crater lake, east Java, Indonesia. *Journal of Volcanology and Geothermal Research*. 135, 299-329.
- van Hinsberg, V. Hyperacid Crater Lake and the Banyu Pait River, East Java, Indonesia. Drs thesis (unpublished), Utrecht 2001.
- van Hinsberg, V., Berlo, K., van Bergen, M., Williams-Jones, A., 2010a. Extreme alteration by hyperacidic brines at Kawah Ijen volcano, East Java, Indonesia: I. Textural and mineralogical imprint. *Journal of Volcanology and geothermal Research*. 198, 253-263.
- van Hinsberg, V., Berlo, K., Sumarti, S., van Bergen, M., Williams-Jones, A., 2010b. Extreme alteration by hyperacidic brines at Kawah Ijen volcano, East Java, Indonesia: II Metasomatic imprint and element fluxes. *Journal of Volcanology and Geothermal Research*. 196, 169-184.
- Vigouroux, N., G. Williams-Jones, A.E. Williams-Jones, V.J. van Hinsberg. Tracking volatile ratios through the magmatic and hydrothermal system of Kawah Ijen Volcano, Indonesia. 2009 Portland GSA Annual Meeting, 18-19 October. Paper No. 155-11.
- Vigouroux, N., Mauri, G., Williams-Jones, G. van Hinsberg, V., Willis-Jones, A.E., Nasution, A., 2007. Ijen (Indonesia): 2007 field visit found degassing and increasing fumarole temperatures. *Bulletin of the Global Volcanism Network*, 32:09.
- Whitford, D.J., Nicholls, I.A., Taylor, S.R., 1979. Spatial Variation in the Geochemistry of Quaternary Lavas across the Sunda Arc in Java and Bali. *Contributions to Mineralogy and Petrology*. 70, 341-356.
- Whittaker, J.M., Muller, R.D., Sdofias, M., Heine, C., 2007. Sunda-Java trench kinematics, slab window formation and overriding plate deformation since the Cretaceous. *Earth and Planetary Science Letters*. 255, 445-457.

Introduction to Chapter 3

The main chapter of this thesis is a scientific article that has been submitted for publication to Economic Geology. The chapter provides new insights into the relationship between acid-sulfate alteration and the formation of high-sulfidation epithermal precious metal deposits. Using data from analyses of the compositions of gases and fresh and altered rocks from the crater of Kawah Ijen volcano, Indonesia, the case is made that metals (Cu, Ag and Au) transported by aqueous vapors passing through the crater floor are being concentrated by incorporation in pyrite during acid sulfate alteration.

Chapter 3

Fumarolic Activity, Acid-Sulfate Alteration and High-Sulfidation Epithermal Precious Metal Mineralization in the Crater of Kawah Ijen Volcano (Java, Indonesia)

S. Scher, A.E. Williams-Jones, and G. Williams-Jones.

Manuscript to be submitted to Economic Geology

Abstract

High-sulfidation epithermal deposits occur in the eroded edifices of arc volcanoes and, although there is general agreement that the hydrothermal alteration accompanying the ores is the product of volcanic degassing, there is much less agreement on the nature and origin of the ore fluid. Opinion is divided over whether the ore fluid is a vapor or a liquid, and whether it is entirely volcanic or of mixed volcanic-meteoritic origin. Kawah Ijen, an active stratovolcano (mainly andesitic in composition) located in the Ijen Caldera Complex in Java, Indonesia, is an excellent setting in which to address these issues.

The Kawah Ijen crater is approximately one kilometer in diameter and hosts the world's largest hyperacidic lake (pH ~ 0). On the lake edge is a small and actively degassing solfatara, which is surrounded by a much larger area of acid-sulfate alteration that was exposed during a phreato-magmatic eruption in 1817 that excavated the crater to a depth of 250 m. The altered area comprises zones of residual silica, alunite-pyrite and dickite/kaolinite. Based on the fractionation of ^{34}S and ^{32}S between alunite and pyrite, it formed at a temperature between 200 and 300°C. High sulfidation epithermal mineralization occurs in this area in the form of massive and vein-hosted pyrite that contains up to 192 ppb Au, 9.2 ppm Ag, 6,800 ppm Cu, and 3,430 ppm As; these elements are invisible at the highest resolution of scanning electron microscopy, and thus occur either in the form of nano-particles or are in solid solution in the pyrite. Condensed fumarolic gases released from the solfatara and sampled at temperatures between 330 and 495 °C contain up to 3 ppm Cu and 3.8 ppm As; the concentrations of Au and Ag were below detection. The pH of the condensed gas (water vapor) was ~ -0.5.

These observations support a model in which highly acidic gases condensed ~ 250 m beneath the floor of the crater. Depending on the fluid/rock ratio, the condensed liquids altered the andesitic host rocks by leaching them to leave behind a residue of “vuggy silica” (high fluid/rock ratio), by replacing the primary minerals with alunite and pyrite (intermediate fluid/rock ratio) or by converting them to dickite/kaolinite (lower fluid/rock ratio). Gold- silver- and copper-bearing phases were undersaturated in the condensed liquids. However, they were able to concentrate

by adsorbing on the surfaces of the growing pyrite crystals, which developed p-type conductive properties as a result of the uptake of arsenic. The metals were incorporated in the pyrite either by their electrochemical reduction to form native metal nano-particles or through coupled substitutions with arsenic for iron and sulfur. The results of this study provide compelling evidence that high sulfidation epithermal precious metal mineralization can form directly from condensed magmatic gases.

Keywords: Acid-sulfate alteration, epithermal, high-sulfidation, vapor transport of metals, “invisible” copper, silver and gold in pyrite

1. Introduction

The nature of the ore fluid in high-sulfidation epithermal precious metal systems continues to be a topic of debate, in large part, because researchers are forced to base their interpretations on observations made long after the hydrothermal activity that produced the deposits has ceased. Currently, opinion is divided over whether the ore fluid is a liquid or a vapor. The observation that the alteration of the volcanic rocks in these systems is the product of their interaction with an extremely acid fluid (Steven and Ratté, 1960) has led to a consensus that this fluid is a condensed vapor (Stoffregen, 1987; Hedenquist et al., 1994; Arribas, 1995; Hedenquist et al., 1998; Chouinard et al., 2005b; Mavrogenes et al., 2010; Henley and Berger, 2011; Berger and Henley, 2011). However, as deposition of the ore minerals commonly postdates alteration (Gray and Coolbaugh, 1994; Ruggieri et al., 1997), many researchers have concluded that the ore fluid is a liquid of volcanic or mixed volcanic-meteoric origin that was introduced later (e.g. Hedenquist and Lowenstern, 1994; Hedenquist et al., 1994; Arribas, 1995; Hedenquist et al., 1998). This interpretation is strongly influenced by the widely held view that only a liquid can transport metals in concentrations sufficient to form economic deposits (Krauskopf 1957; 1964). Nevertheless, there are some high sulfidation epithermal gold-silver deposits, for which there is strong evidence that ore deposition accompanied alteration, thereby implying that the ore fluid may have been a vapor (Chouinard et al., 2005b; Mavrogenes et al., 2010; Voudouris, 2010; Henley and Berger, 2011; Berger and Henley, 2011). There is also growing evidence that hydrothermal vapors may be able to dissolve metals in concentrations sufficient for them to become ore fluids (Heinrich et al., 1992; 1999; Archibald et al., 2001; 2002; Williams-Jones and Heinrich, 2005; Zevin et al. 2007, 2011).

In many high sulfidation epithermal gold-silver deposits, the precious metals are concentrated due to saturation of the ore fluid with a mineral such as electrum, but in some deposits, the ore metals occur as microscopically invisible inclusions in pyrite or within the structure of this mineral (Chouinard et al., 2005a). Deposits in which the precious metals are invisible in pyrite do not form through saturation of the fluid in a gold- or silver-bearing phase. Instead, the precious metals are

incorporated in the pyrite through surface adsorption mechanisms, and their concentrations may be well below the levels required for saturation (Chouinard et al., 2005a; King et al., 2010).

As high sulfidation epithermal systems are considered to form relatively high in the edifices of calc-alkaline stratovolcanoes, the craters of active examples of such volcanoes should provide excellent opportunities for gaining further insight into the processes by which gold and silver are transported and deposited in these systems. Kawah Ijen volcano in Java, Indonesia, is a particularly good location at which to gain such insight. The crater of this volcano, which is approximately 1 km in diameter, contains well-developed surface expressions of a magmatic-hydrothermal system, namely a solfatara with high temperature fumaroles, a hyperacidic lake, and an extensive area of acid-sulfate alteration. The alteration zone records a potentially long-lived hydrothermal system that was excavated to a depth of approximately 250 m by a phreato-magmatic eruption in 1817, which destroyed the solfatara active at that time (Hengeveld, 1920). Significantly, the current solfatara is located within this alteration zone. As a result of the 1817 eruption, we have been afforded a rare opportunity to investigate the nature and origin of an altering and precious metal mineralizing hydrothermal system that has most of the characteristics of high sulfidation epithermal systems, i.e., zones of residual (vuggy) silica, intense alunitization, pyritization, and elevated concentrations of copper, silver and gold. The purpose of this study is to carefully characterize the alteration and mineralization, reconstruct their evolution, determine the role of volcanic degassing in these processes and use the observations that can be made to constrain a genetic model applicable to high sulfidation epithermal precious metal deposits.

2. Geological Setting

Kawah Ijen is an active basaltic to dacitic stratovolcano located on the southeast rim of the Ijen Caldera Complex (ICC), East Java, Indonesia, which forms part of the Sunda volcanic arc that developed as a result of the subduction of the Indo-Australian plate beneath the Eurasian plate (Fig. 1). Magmatism on Java is the result of the subduction of oceanic crust under thick and old continental crust

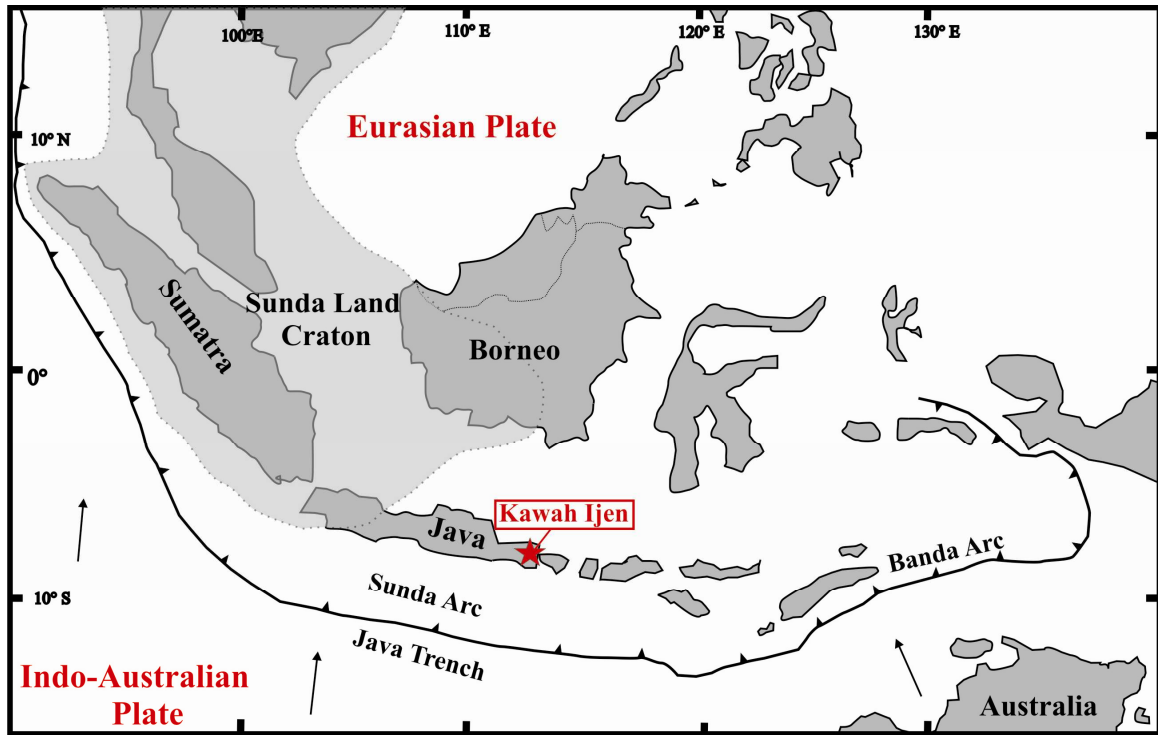


Fig. 1. Tectonic setting of Indonesia (modified from Hoffmann-Rothe et al., 2001), showing the location of Kawah Ijen volcano (red star). Black arrows show the directions of plate movement. The dashed outline of the ‘Sunda Land Craton’ indicates the possible extent of continental lithospheric basement (Hamilton, 1979).

(Katili, 1975); it is more basic than on Sumatra because of the thinning of the underlying crust towards Bali (Edwards et al., 1994). The chemical affinity of volcanism on Java has shifted from that of island arc tholeiites with minor K-enrichment (Tertiary volcanic arc) to mainly calc-alkaline volcanism (Quaternary Sunda Arc; Soeria-Atmadja et al., 1994).

The Ijen Caldera Complex is a 20 km-wide, circular caldera depression that formed over 50,000 years ago as a result of the collapse of the Ijen stratovolcano (Hengeveld, 1920 and Kemmerling, 1921, as reported in van Hinsberg et al. 2010; Sitorus, 1990). The caldera is bordered by a steep escarpment to the north (Kendeng caldera wall) and volcanic peaks in the north, east and south (Gunungs Ringgih, Merapi, Ranteh, Djampit, and Suket; Fig. 2). Within the caldera, there are lacustrine sediment deposits in the north (a large lake seems to have occupied the entire northern half of the caldera; van Hinsberg et al., 2010a), and plains and smaller volcanic vents that form a roughly east-west lineament through the central-southern half of the caldera.

There are two types of volcanoes in the ICC, caldera rim and intracaldera volcanoes. Together with Merapi, a much larger flanking volcano, Kawah Ijen lies at the junction between the caldera rim volcanoes and the easternmost end of a linearly distributed group of intra-caldera volcanoes (these volcanoes trend NE-SW across the caldera; Fig. 2). The caldera rim volcanoes erupt high-Ca magmas of basalt to basaltic andesite composition and the intra-caldera volcanoes erupt low-Ca magmas of basaltic andesite to dacite composition (Fig. 3; Handley et al., 2007). The locations of these volcanoes, i.e., along the caldera rim and on a NE-SW lineament through the caldera, suggest that there are structural controls of magma ascent in the caldera, e.g., ring fractures and intra-caldera planar fractures that act as magma pathways. This is supported by the observation that the rocks of the rim and intra-caldera volcanoes display distinctly different fractionation trends, which suggests spatial variations in chemistry that might be linked to sub-volcanic structures and different reservoir depths (Handley et al., 2007).

Kawah Ijen is unique in the caldera; it erupts both the high- and low-Ca magmas, presumably due its location at the junction of the caldera rim and intracaldera

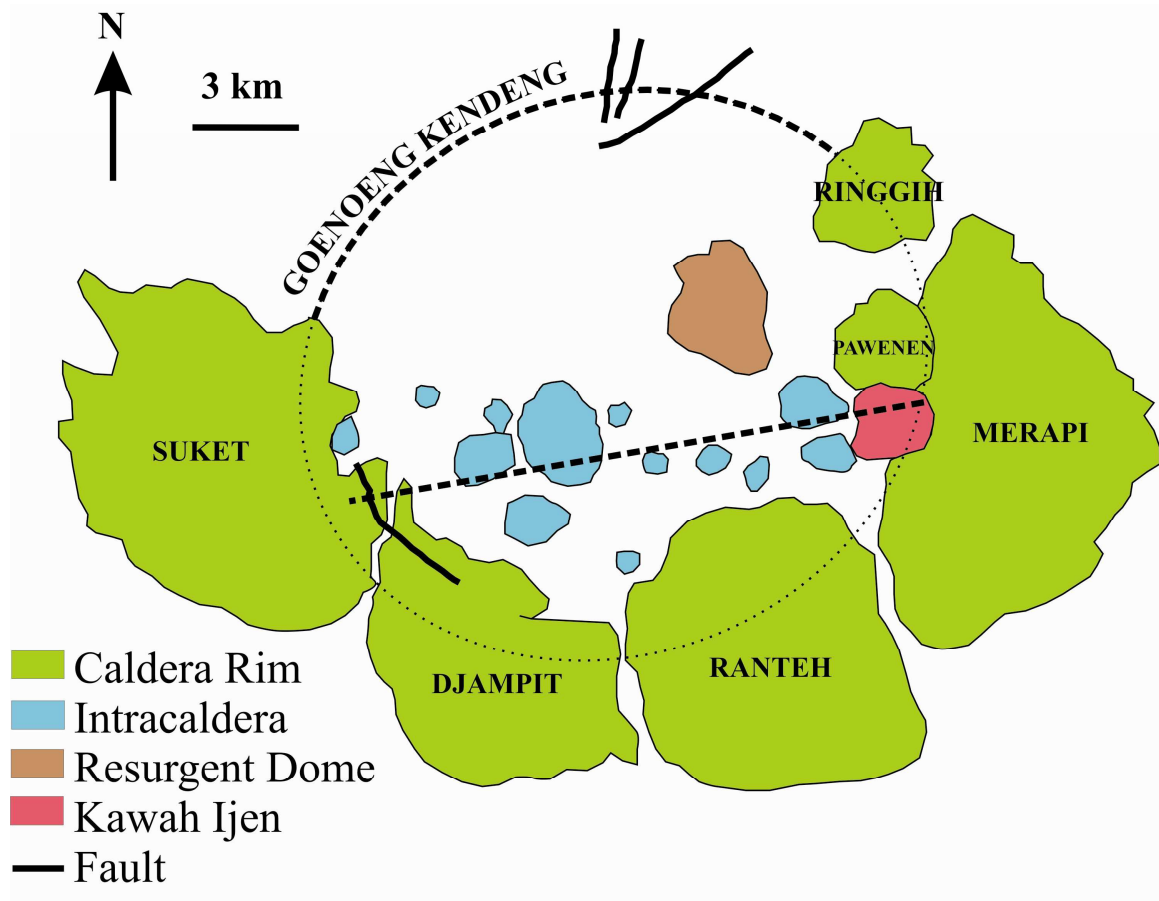


Fig. 2. The distribution of volcanoes in and adjacent to the Ijen Caldera. The dashed line highlights the roughly east-west distribution of the intra-caldera volcanoes. This line also represents a trend of decreasing age of volcanism. The dashed curve in the north indicates the limit of the caldera and represents the inferred location of the base of the pre-caldera cone (modified from Berlo, 2001).

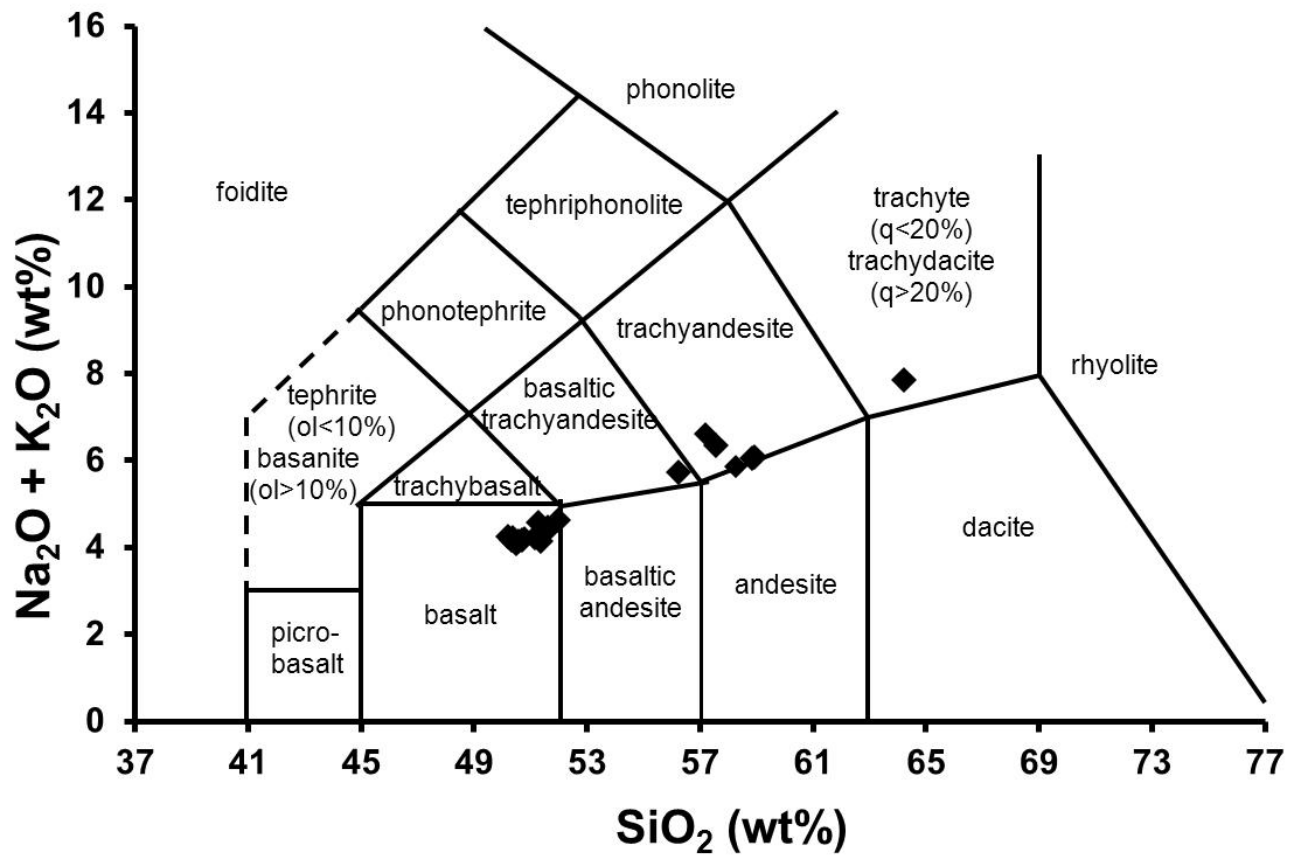


Fig. 3. Total Alkali-Silica (TAS) diagram for samples taken from Kawah Ijen deposits in the caldera. Volcanic rocks range from basalt to dacite in composition and straddle the subalkaline/alkaline boundary. The data are from Sitorus (1990) and Berlo (2001).

volcanoes. Prior studies by Sitorus (1990) and Berlo (2001) sampled 21 Kawah Ijen lava flow deposits (Fig. 3). Of these 14 were basalt, one was a basaltic andesite, five were andesites, and one was a dacite. Tephra deposits (scoria, ash, pumice, bombs), pyroclastic and epiclastic flows and pillow lavas (only seen in the crater) are also found at Kawah Ijen.

3. Eruptive History

Kawah Ijen is a composite cone, which is currently in a destructive phase that commenced with a summit disrupting explosion and resulted in a lava flow to the south of the volcano. The summit of Kawah Ijen consists of an east-west oriented elliptical crater that is nearly 1 km wide. The crater rim is about 2340 meters above sea level (asl) on average, however, it extends locally up to 2386 meters asl. The crater at Kawah Ijen is host to an active dome, a center of acid-sulfate alteration and the world's largest hyperacidic crater lake. The crater lake has a pH of \sim -0.2 to 0.5 and is 800 x 600 meters in area and 180 meters deep (BGVN 32:02; van Hinsberg et al., 2010b; Takano et al., 2004). The composition is controlled by rocks that fall into the lake, which provide the cations, and by fumaroles on the lake floor, which supply the anions (van Hinsberg et al., 2010a). Finally, there are thermal springs that emerge along the flank of the volcano that are sourced by the magmatic-hydrothermal system (Palmer et al., 2011).

Current volcanic activity has shifted to the west side of the crater where a depression in the rim is located. Here, numerous lava flows descended into the volcano. These flows range from basalt to dacite in composition, although the only dacite flow is found west of the depression and could represent a dome facies (van Hinsberg, 2001). During the past two decades, the volcano has had numerous phreatic eruptions and produced air-fall deposits of ash, rock and lava fragments, as well as sulfur particles.

The oldest recorded eruption at Kawah Ijen was in 1796 (Hengeveld, 1920 and Kermmerling, 1921, as reported in van Hinsberg et al., 2010a). However, in 1789, a Dutch commander visited the crater and described it as being 180 m deep with a boiling lake that was releasing thick clouds of white smoke (Kemmerling, 1921, as

reported in van Hinsberg et al., 2010a). In 1817, the crater was visited by a local villager who reported the mining of several sulfur fumaroles and observed that the crater was only 18 m deep. There was no crater lake. That same year, from January to February, the volcano entered an eruptive phase, the largest eruption occurring in late January when the crater floor was ejected, and a 250 m-deep crater was excavated (Kemmerling, 1921, as reported in van Hinsberg et al., 2010a). In 1820, the crater was again visited and a lake was reported to be present (Kemmerling, 1921). The next recorded activity was in 1917 and was accompanied by a rapid decrease in water level in the lake following an earthquake in Bondowoso, Java (Hengeveld, 1920; Kemmerling, 1921). In 1952, an ash and sulfur cloud rose above the crater (Smithsonian Institute, 2000) and in the 1990s there were five small phreatic eruptions (van Hinsberg, 2001).

The current volcanic activity, is centered on a small magmatic dome that is the site of large numbers of high temperature fumaroles (Vigouroux-Caillibot, 2011), and is located within an area of acid-sulfate alteration measuring over 500 m in diameter, extending from the southeast shore of the crater lake towards the crater wall. The dome is blanketed by native sulfur deposits, is rhyolitic in composition (van Hinsberg et al., 2010b) and measures ~100 m in diameter and 20 m in height. Fumarolic temperatures vary from less than 200 °C to greater than 600 °C. The presence of a large area of altered rocks and the location of the active dome within it suggests that there has been long-lived hydrothermal activity in this part of the crater and that the center of this activity (currently the active dome) has moved with time. The present location of the active dome at the western edge of the altered area and the fact that the alteration extends right up to the dome, suggest that there has been a westward migration of the hydrothermal system. Furthermore, the location of the active dome in the area of altered rocks indicates that the centers of extrusive igneous activity and hydrothermal activity are coincident.

4. Methodology

Fieldwork for this study was conducted at Kawah Ijen volcano from July 16 to August 8, 2009 and August 3 to 15, 2010, and involved collecting gas, condensate

and sublimate samples from the active dome and rocks from the alteration center and active dome. The gases were collected in both closed and open systems; the open system sampled the condensable gases by condensing them to liquid and the closed system sampled the entire gas, including the incondensable fraction, using Giggenbach bottles (van Hinsberg et al., in prep.). The fumarolic gases were analyzed at the University of New Mexico. A gas chromatographic system (GOW MAC), equipped with a thermal conductivity detector (TCD) and flame ionization detector (FID), was used to determine concentrations of H₂, Ar, N₂, O₂, H₂, CO₂, CO, CH₄. Wet chemical methods, involving the use of an automatic titrator, specific ion electrodes and gravimetric techniques were employed to determine the concentrations of CO₂, SO₂, H₂S, HCl, HF. The concentrations of the major and trace elements in the condensates were analyzed using ICP-AES and ICP-MS, respectively by GeoLabs (Vancouver, B.C.).

Thin sections of fresh and altered rock were examined at McGill University with an Olympus BH2 microscope and a Hitachi S-3000N FEGSEM scanning electron microscope (SEM) equipped with an energy dispersive detector (EDS). These instruments were used to identify the minerals and determine the textural relationships amongst them. As the altered samples are very fine-grained and contain minerals that are difficult to identify, microscopic examination was complemented by X-ray diffraction (XRD) analyses conducted at the Université du Québec à Montréal and the Université du Montréal (Montréal, QC) on a Siemens D5000 and D8 Advance, respectively. Minerals were identified using DIFFRAC^{plus} EVA (Bruker ASX), and semi-quantitative mineral proportions were determined from Rietveld analysis using the program DIFFRAC^{plus} TOPAS (Bruker ASX). The composition of alunite and pyrite was analyzed using a JEOL 8900L electron microprobe (EMP) at McGill University. Pyrite was also analyzed using laser-ablation-induced coupled mass spectrometry (LA-ICP-MS) at the Geologic Survey of Canada, Ottawa (GSC) and at the Université du Québec à Chicoutimi, Chicoutimi (UQAC). The LA-ICP-MS at the GSC comprises an Analyte.193 laser ablation sampler (LA) coupled to an Agilent 7700x quadrupole ICP-MS; at UQAC, the laser is an Excimer Resolution M-50 (Resonetics) and the ICP-MS is an Agilent

7700x. Major and trace element compositions of whole-rock samples were analyzed by ICP-AES and ICP-MS, respectively, at ACME Analytical Laboratories (Vancouver, BC).

The operating conditions for electron microprobe analysis of alunite (K, Na, S, Fe, Ca, Al) were a 15 kV acceleration voltage, a 1 nA beam current, and a 20 μm spot size. The standards used in the calibration were natural albite for Na, synthetic Al_2O_3 for Al, natural orthoclase (Cameca standard) for K, Astimex BaSO_4 for S and natural pyrope (Smithsonian standard) for Fe and Ca. Electron microprobe analyses of pyrite were limited to As, Cu, Fe, and S, and were carried out using a 20 kV acceleration voltage, a 3 nA beam current and a focused beam. The instrument was calibrated for these elements using a synthetic arsenic standard, chalcopyrite (Cu) and pyrite (Fe, S). Detection limits were approximately 460, 215, 220, and 200 ppm for As, Cu, Fe, and S, respectively; uncertainties for Fe and S were less than 1% and uncertainties for As and Cu were approximately 40 and 75 ppm, respectively. After EMP analysis of pyrite, the carbon coating was removed and the samples were cleaned in an ultrasonic bath. They were then analyzed for Fe, S, Co, Ni, Cu, Zn, As, Se, Mo, Ag, Cd, Sn, Sb, Te, Au, Hg, Tl, Pb, and Bi using LA-ICP-MS. The operating conditions for the laser at the GSC were a 193 nm wavelength, 10 Hz repetition rate, 5 J/cm^2 energy density, and a pulse duration of 4 ns, and for the ICP-MS, the conditions were 1150 kW forward power, 7 mm sampling depth, ThO^+/Th^+ of <0.3%, and carrier (He) and make up (Ar) gas flows of 0.6 L/min and 1.08 L/min, respectively. The data acquisition protocol was time resolved, the scanning mode was peak hopping, 1 point per peak, 10 ms dwell time per isotope, 120 s analysis time, and the quadrupole settling time was 1 to 5 ms depending upon mass jump. The same operating conditions were used at UQAC except that the repetition rate was 15 Hz, the forward power, 1250 kW, the sampling depth, 3 to 4 mm, ThO^+/Th^+ of <1%, and the carrier (He) and make up (Ar) gas flows of 0.65 L/min and 0.85 to 0.95 L/min, respectively. The analytical procedure was also the same except that dwell time per isotope was 5 ms, and the analysis time 90 s. Several samples, including two calibration standards and a synthetic pyrrhotite standard, which were used for quality control, were mounted in the sample cell. The United

States Geologic Survey (USGS) synthetic sulfide standard, MASS-1 (Wilson et al., 2002), was the primary calibration standard. However, a USGS basaltic glass standard (USGS GSE-1G, Guillong et al., 2005) was used to extend the range of elements that could be quantitatively analyzed. The Calibration standards were analyzed twice and the quality control standard once approximately every 20 analyses. Analyses were performed as spot ablations or as line ablations using nominal spot diameters ranging mainly from 21 to 69 μm , but spot diameters were as large as 138 μm where grain size permitted. The counts measured for the isotopes of the elements of interest were converted into concentrations using GLITTERTM, an on-line data reduction program for LA-ICP-MS (Griffin et al., 2008). The detection limit for As and Se was approximately 100 ppb, for Cu, Ni, Zn, Te, and Hg was approximately 10 ppb and for Mo, Ag, Cd, Sn, Sb, Au, Tl, Pb, and Bi was less than 5 ppb. For each pyrite grain, the trace metals analyses were considered reliable if the concentrations measured were 1σ deviation above the detection limit.

Sulfur ($\delta^{34}\text{S}$, $\delta^{33}\text{S}$ and $\delta^{36}\text{S}$) isotope compositions of alunite-pyrite pairs were analyzed at McGill University on a Thermo-Finnigan MAT 253 dual inlet IRMS; the precision of the instrument is 0.01‰. Samples of alunite and pyrite were crushed to a fine powder using a mortar and pestle and were then cleaned in a toluene bath in order to remove any relict native sulfur precipitated on the samples from the active dome. Sulfate and sulfide from alunite and pyrite were subsequently extracted from the sample using Thode (for sulfate) and chromium reduction solution (CRS; for sulfide) reagents. Once sufficient sulfate and sulfide had been extracted from each sample, silver nitrate was added to convert the sulfur to silver sulfide for analysis in the mass spectrometer. The results are reported in δ notation relative to V-CDT and the internal reference material was IAEA-S-1.

5. The Alteration Center

As mentioned earlier, the alteration center covers an area approximately 500 m in diameter, extending from the southeast shore of the crater lake towards the crater wall, and includes the active dome (Fig. 4). Within this center, pyroclastic and

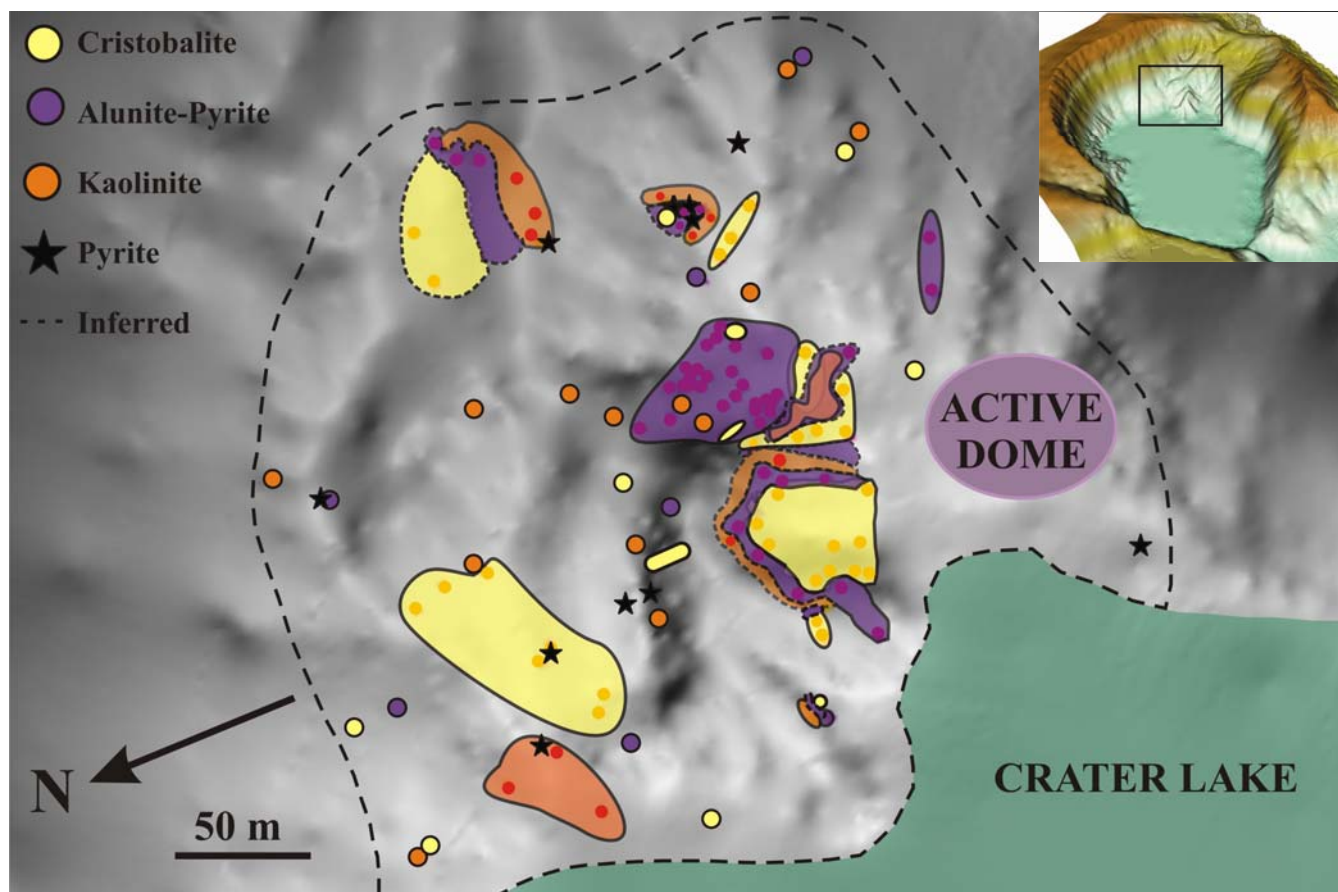


Fig. 4. Shaded relief map showing the distribution of cristobalite (residual silica), alunite-pyrite and kaolinite alteration zones. Each zone was identified by outlining areas (solid lines) distinguished by a predominant mineral as determined by Rietveld analysis of X-ray diffractograms. Yellow represents the cristobalite zone, purple the alunite-pyrite zone, and orange the kaolinite zone. Black stars show the locations of pyrite veins or areas of massive pyrite. Dashed lines indicate inferred extent of alteration. Small circles indicate sample locations for cristobalite, alunite-pyrite and kaolinite alteration (yellow, purple and reddish-orange, respectively). The active dome is shaded in purple as XRD analysis confirms that its predominant alteration is alunitic. The inset in the upper right corner is a digital elevation model (DEM) of the Kawah Ijen crater. The black box in the DEM indicates the study area.

epiclastic rocks (Fig. 5a) of unknown initial composition and lavas that are vesicular and plagioclase-rich (Fig. 5b), including pillowed varieties (Fig. 5c), have experienced intense acid-sulfate alteration (Fig. 5d-f) that has left few relicts of the original mineralogy. This alteration is continuing at the active dome. The altered rock consists of variable proportions of alunite, natroalunite (the sodic, high-temperature end-member of the alunite group of minerals), cristobalite, quartz, kaolinite, dickite, diaspore, gypsum and pyrite. Although cristobalite is metastable at the conditions of alteration, it commonly forms during acid-sulfate alteration, e.g., in the Nansatsu District, Japan (Hedenquist et al., 1994) and Comstock District, Nevada (Hudson, 2003); gypsum, which fills fractures, is only seen near the lake shore and likely formed due to the evaporation of lake water. Native sulfur is also present in the altered rocks, although it is unclear whether it is part of the hydrothermal assemblage or infiltrated fissures during subsequent condensation of native sulfur originating from the active dome. The minerals listed above are also found in the altered rocks of high-sulfidation epithermal precious metal deposits, i.e., cristobalite occurs in the residual silica facies, the assemblage alunite-natroalunite-pyrite forms the advanced argillic alteration facies and kaolinite/dickite forms the argillic alteration facies.

Alunite is typically massive, having pervasively replaced pyroclastic or epiclastic rocks, and less commonly occurs as bladed crystals, typically < 20 microns in diameter (Fig. 6a). Frequently, it is observed intergrown with pyrite in large masses that are exposed on a scale of meters or tens of meters (Fig. 5d and e), in which the two minerals are evidently in textural equilibrium (Fig. 6b). Nonetheless the distribution of the pyrite in these masses is quite heterogeneous (Fig. 5e). Less commonly, alunite occurs as monomineralic outcrops or outcrops in which it is intergrown with cristobalite (Fig. 5d and e). In addition to having replaced its volcanic hosts, alunite also forms veins that cross-cut these rocks. These veins generally contain pyrite and commonly are zoned from pyrite at their margins to alunite in their cores (Fig. 5f and 6a). Kaolinite is locally observed in the alunite-pyrite-bearing rocks, although not in textural equilibrium with these minerals (Fig. 6a). Commonly, kaolinite is observed to have replaced feldspar

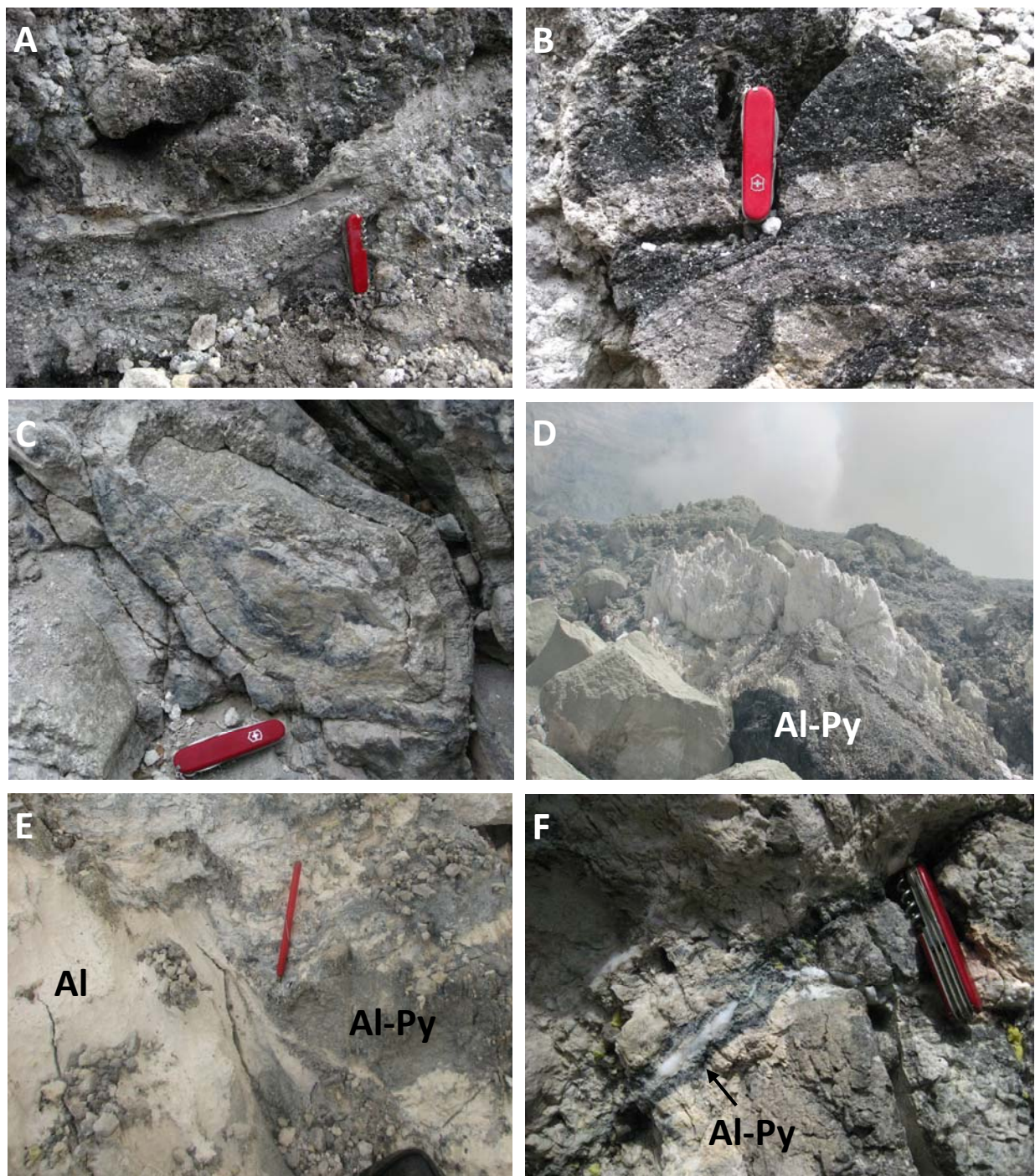


Fig. 5. Macroscopic features of variably altered volcanic rocks in the Kawah Ijen crater; (a) kaolinite-altered epiclastic flow, (b) vesicular and plagioclase-rich lava partly altered to alunitic (white), (c) strongly leached, cristobalite-rich pillow lava, (d) alunitic-cristobalite spine (white) and patch of alunitic-pyrite altered rocks in the foreground, (e) contact between alunitic and alunitic-pyrite, (f) pyrite-alunitic vein (alunitic is in the center) cross-cutting alunitic-altered lava. Pocket knife and magnet for scale, except in “d” which has a field of view of 30 m.

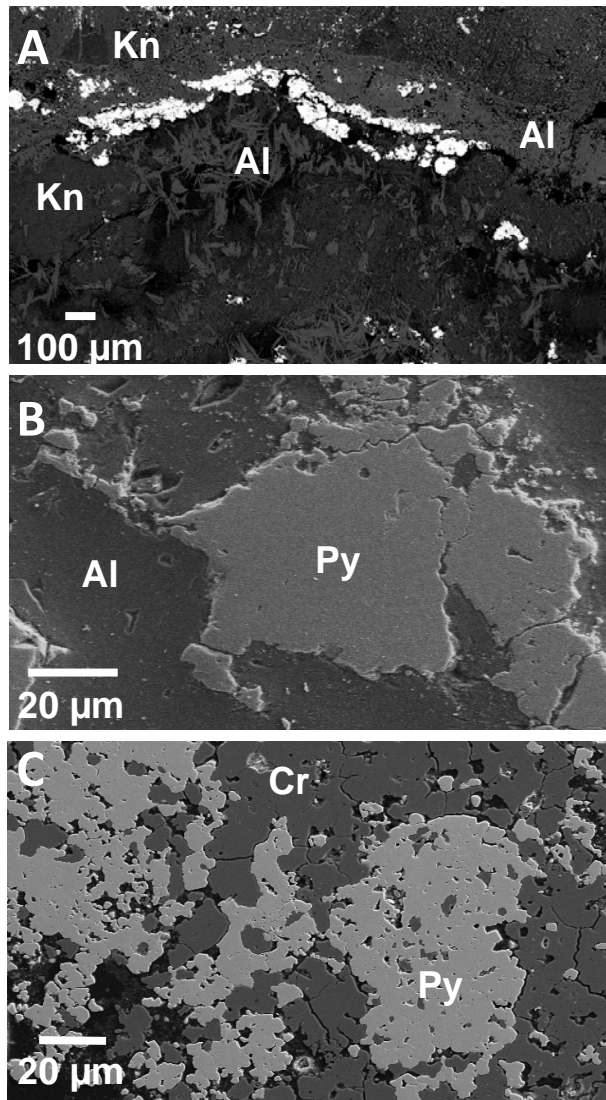


Fig. 6. Back-scattered electron microprobe images showing; (a) alunite-pyrite halo surrounding a vug bordered by pyrite and partly filled by bladed alunite crystals overprinting kaolinite; (b) irregularly shaped pyrite crystals in a matrix of alunite from an area of extensive alunite-pyrite alteration; (c) intergrown cristobalite-pyrite aggregates. The abbreviations are: Kn for kaolinite, Py for pyrite, Al for alunite, and Cr for cristobalite. Note different scales.

phenocrysts in weakly altered rocks. Cristobalite occurs mainly as crystal aggregates and is commonly intergrown with pyrite (Fig. 6c). Pyrite occurs mainly in association with alunite. The grains are mostly sub-rounded cubes that range up to ~150 microns in diameter. In weakly altered rocks, pyrite is commonly observed as a secondary phase after relict titanomagnetite.

The proportions of minerals in the altered rocks were determined using Rietveld analysis (Appendix I) of the XRD diffractograms. This information was used to create a map showing the distribution of the principal alteration minerals (Fig. 4). Although alunite and natroalunite were distinguished on the basis of their chemical composition, and some crystals had close to end-member composition, most were of intermediate composition. Consequently, it was only possible to map the distribution of a single alunite phase. As pyrite was heterogeneously distributed in most samples, it was removed prior to XRD analysis, and its proportion in samples was not established quantitatively using Rietveld analysis. Cristobalite is the dominant mineral in the majority of samples, followed by alunite and kaolinite (Appendix I). The solid black lines in Figure 4 delineate areas in which the dominant mineral has been identified in a relatively large number of samples; areas surrounded by dashed black lines infer mineral dominance based on a small number of samples. There are four relatively large areas of cristobalite predominance, three of which are surrounded concentrically by areas of alunite and kaolinite dominance. There is an additional, albeit small, area of concentrically-zoned cristobalite-alunite-kaolinite in the southwest part of the map. This area also includes three pyrite-alunite veins (KS09-P1, P2, P3) all of which contain pyrite grains with elevated levels of Cu and Ag (Table 1 and Appendix II).

Two rock samples were collected to represent the active dome. One of these samples, (KS10-SFM-1) consists predominantly of alunite followed by kaolinite and cristobalite (64% alunite, 23% kaolinite, 13% cristobalite) and the other (KS10-SFM-2) is composed of nearly equal proportions of kaolinite and cristobalite and a relatively small proportion of alunite (45% cristobalite, 39% kaolinite and 16% alunite; Appendix I). The active dome samples referred to above also contain a significant proportion of Cu-As-bearing pyrite (Table 1 and Appendix II).

Table 1: Representative trace element compositions (ppm) of pyrite grains from the alteration center at Kawah Ijen. Analyses were performed using LA-ICPMS.

	Co	Ni	Cu	Zn	As	Se	Mo	Ag	Cd	Sn	Sb	Te	Au	Hg	Tl	Pb	Bi
KS10-VB-5B	75.07	31.66	147.93	54.90	98.91	86.07	3.54	0.49	1.05	17.22	4.98	n.d.	0.02	1.12	1.22	30.17	0.93
KS10-VA-3	130.83	73.77	2917.58	594.58	285.60	2.61	24.14	0.10	4.95	8.92	0.33	n.d.	0.02	2.56	109.30	27.38	0.19
KS09-P3	n.d.	20.88	540.66	26.50	145.98	63.94	26.13	0.27	0.61	4.16	3.62	20.98	0.01	0.87	12.31	45.96	22.39
KS09-VA-9	n.d.	27.37	246.17	2.47	140.47	59.83	18.91	0.07	1.22	5.48	3.40	6.46	0.00	0.52	16.71	25.91	14.78
KV08-2	n.d.	1.58	938.50	0.94	26.60	17.44	14.75	0.22	0.01	0.30	2.08	2.09	0.01	14.66	5.51	1.38	3.83
KS10-VA-20	57.68	95.51	485.77	245.87	570.48	65.49	10.79	1.25	10.10	47.69	3.86	n.d.	0.04	1.23	148.96	466.55	17.17
KS10-KISS-7	127.30	37.01	993.86	45.03	388.62	139.33	95.17	0.60	2.04	6.43	3.15	n.d.	0.02	6.87	18.83	78.08	7.87
KS10-VC-2	227.88	22.23	1555.85	115.44	25.20	17.87	8.65	0.85	1.06	4.60	1.43	n.d.	0.07	1.32	10.72	11.57	8.11
KS10-SFM-1	81.33	29.29	134.75	14.74	63.16	106.48	5.98	0.84	0.83	8.49	4.10	n.d.	0.02	8.91	24.63	44.47	5.73
KS09-W2	n.d.	2.33	73.65	1.08	117.21	40.48	113.03	0.30	0.30	6.80	0.30	53.87	0.00	0.85	1.97	5.89	4.94
KS09-W4	n.d.	152.17	1328.33	1385.76	14811.61	648.37	511.56	4.31	15.32	1204.69	321.32	81.66	0.10	685.10	321.38	546.39	1914.55
KS09-P2	n.d.	26.59	1203.11	19.53	392.34	91.39	100.79	0.52	1.47	6.68	7.15	45.27	0.01	2.11	49.31	157.78	46.33
KS09-W6	n.d.	15.66	201.99	4.26	316.73	438.25	12.42	0.22	0.51	1.17	0.73	32.31	0.00	1.61	79.30	532.74	10.86
KV08-204A	n.d.	0.39	458.57	6.84	13.55	16.84	1.67	0.14	0.20	0.18	1.46	1.74	0.01	2.00	1.51	8.48	1.24
KV08-204C	n.d.	45.81	121.74	7.65	3.94	172.10	25.53	0.83	0.05	0.29	0.30	0.40	0.01	<0.21	0.18	53.39	0.47
KV08-203	n.d.	6.60	78.24	4.19	68.43	17.44	58.36	0.51	0.10	0.26	1.32	46.33	0.08	3.99	2.32	4.40	4.12
KV08-X	n.d.	143.10	1102.46	2.60	749.43	70.75	240.71	2.34	0.18	1.12	1.77	32.54	0.02	10.48	2.99	385.50	2.24

n.d. indicates that the element was not detected and n.a. indicates that the element was not analyzed

5.1. *Mass changes accompanying alteration*

From the previous section, it is evident that alteration of the volcanic rocks was accompanied by large compositional changes; these rocks now consist dominantly of cristobalite and/or alunite and/or kaolinite and/or pyrite. In order to quantitatively evaluate these compositional changes, the bulk concentrations of major and trace elements in the altered rocks were compared to those of potential unaltered precursors. As all the rocks in the crater have undergone some alteration, the compositions of the unaltered precursors were taken from samples outside the crater, which were analyzed by Berlo (2001). Based on the compositions of unaltered Kawah Ijen volcanics, the precursors to the altered rocks could have been trachydacites, andesites/trachyandesites, or basalts (Fig. 3). In order to identify the protolith, the concentrations of potentially immobile major and trace elements pairs in unaltered trachydacite, andesite/trachyandesite and basalt (Table 2 and Appendix III) were compared to the corresponding concentrations of these elements in the altered rocks (Table 3 and Appendix IV). Given that the ratio of an immobile element pair is by definition constant, a binary plot of these elements for altered and unaltered rocks should yield a linear distribution for a single protolith or a set of lines, in the case of multiple protoliths, that pass through the protolith compositions and the origin (Maclean and Kranidiotis, 1987). Only the pairs Nb-Zr and TiO_2 -Zr met these criteria and the scatter about the line was much smaller for Nb-Zr than for TiO_2 -Zr (Fig. 7a, b); in plots involving Al (commonly an immobile element), the data display a high degree of scatter, indicating that Al was mobile during alteration; Al is enriched in the pyroclastic/epiclastic volcanics and depleted in the lavas (Fig. 8). Somewhat surprisingly, the three potential protolith compositions (basalt, andesite and dacite) all lie on the line defined by the altered rocks in the Nb-Zr plot (Fig. 7a), suggesting that the phases controlling fractionation of these elements (probably titanomagnetite and zircon) were on the liquidus at the same time. Consequently, this plot could not be used to identify the precursor. By contrast, the compositions of the three potential protoliths are widely separated on a plot of TiO_2 vs Zr (Fig. 7b) and, with a few exceptions, most of the altered samples lie close to a line passing from the origin through the composition of

Table 2: Average whole rock compositions for unaltered Kawah Ijen volcanic rocks. Major element oxides are reported in wt% and trace elements in ppm. The data are from Berlo, 2001.

	Basalt	Andesite	Dacite
SiO₂	50.96	57.92	64.23
TiO₂	1.00	0.79	0.49
Al₂O₃	19.83	17.95	17.42
Fe₂O₃	9.91	7.50	4.04
MnO	0.18	0.14	0.09
MgO	3.59	2.74	1.12
CaO	9.44	6.57	4.17
Na₂O	3.07	3.53	4.03
K₂O	1.19	2.51	3.80
P₂O₅	0.25	0.20	0.11
Co	27.58	19.25	7.00
Ni	9.92	7.00	5.00
Cu	114.42	46.75	32.00
Zn	82.17	70.25	48.00
Zr	131.83	87.00	184.00
Nb	6.00	4.25	11.00
Pb	6.00	9.75	17.00

Table 3: Major (wt%) and trace element (ppm) whole rock compositions of altered rocks from the Kawah Ijen crater.

	SiO ₂	Al ₂ O ₃	Fe ₂ O ₃	MgO	CaO	Na ₂ O	K ₂ O	TiO ₂	P ₂ O ₅	MnO	Co	Ni	Cu	Zn	Zr	Nb	Pb
KS09-1B	47.64	14.09	0.28	0.18	7.22	0.34	2.84	0.64	0.24	<0.01	<0.2	0.2	0.3	<1	153.1	6.3	7.3
KS09-2B	58.38	20.22	0.59	0.13	0.15	0.17	2.05	0.79	0.11	0.03	0.9	1.2	4.1	15	175.1	8.1	83.2
KS09-3E	37.8	8.19	0.66	0.31	15.38	0.2	1.66	0.58	0.16	<0.01	1.3	2.1	6.7	76	108.1	5.2	24
KS09-3F	44.75	14.36	2	0.15	4.26	0.69	1.87	0.7	0.08	<0.01	3.9	3.8	9.6	150	136.7	6.4	19.8
KS09-7F	33.47	23.51	0.16	0.03	0.1	0.13	4.14	0.44	0.15	<0.01	<0.2	0.7	0.3	<1	103	4.2	26.3
KS09-7TB	33.01	23.04	0.73	0.06	0.73	1.05	4.93	0.44	0.24	<0.01	5.7	1.6	10.7	54	89.9	3.9	26.1
KS09-7U	82.81	3.49	0.55	0.05	0.17	0.3	0.6	0.98	0.09	<0.01	1.3	8.9	7.2	12	234	10.1	33
KS09-7V	36.48	19.86	0.18	0.01	0.45	1.32	3.04	0.51	0.25	<0.01	0.4	1.2	1.9	3	116.9	3.7	51.7
KS09-8H	90.93	2.36	0.85	0.02	0.07	0.08	0.21	1.07	0.07	<0.01	1.9	2.5	4	<1	332.3	11.5	2.6
KS09-8Y	71.93	10.42	1.51	<0.01	0.04	0.19	0.95	0.49	0.18	<0.01	0.7	0.5	1.2	<1	312.8	12.9	40.8
KS09-8ZB	24.86	26.87	11.62	0.03	0.09	0.29	2.38	0.3	0.23	<0.01	11.3	4.7	46.1	4	73.8	3.3	18.1
KS09-10B	19.5	29.03	0.89	0.05	1.75	1.41	2.04	0.29	0.25	<0.01	2.7	0.9	31.2	3	50.7	2.9	33.5
KS09-11B	32.55	22.18	0.16	0.01	0.32	0.63	4.26	0.32	0.21	<0.01	0.9	0.3	9.4	2	96.7	3.3	4.9
KS09-11C	39.45	22.61	0.15	0.02	0.13	0.41	5.72	0.38	0.16	<0.01	0.6	0.7	8	1	129.2	4.2	5.4
KS09-11Y	36.14	19.82	0.86	0.02	0.05	1.83	3.09	0.43	0.07	<0.01	3.1	1.6	13.4	52	197.2	5.3	22.9
KS09-13B	80.84	2.82	2.96	0.06	0.13	0.09	0.46	0.54	0.06	<0.01	6.5	2.4	55.4	<1	315	13	7.1
KS09-14W	34.8	16.74	3.93	0.02	0.09	0.97	3.34	0.38	0.03	<0.01	19	4.6	129.8	1	125.6	5	12.4
KS09-15W	8.62	19.66	19.5	0.01	0.26	2.58	1.54	0.12	0.1	<0.01	26.8	4.1	39.1	2	36.7	1.1	4.4
KS09-16EX	0.43	0.05	<0.04	<0.01	<0.01	<0.01	<0.01	<0.01	<0.01	<0.01	0.5	0.1	1.2	2	7.2	0.2	0.2
KS10-KISS-6	80.95	2.08	0.86	0.09	0.12	0.15	0.11	1.24	0.05	0	2.8	1.6	8	2	239.5	10.6	3.5
KS10-KISS-7	2.49	0.42	48.55	<0.01	0.07	0.04	0.08	0.21	0.02	0.02	159.5	33.1	1110.1	23	21.8	2.3	49.9
KS10-KISS-8	85.35	1.45	0.66	0.07	0.07	0.12	0.11	0.96	0.05	0	1.5	0.9	5.2	1	245.4	11.2	81.5
KS10-KISS-15	31.42	1.82	22.3	0.13	0.22	0.16	0.21	0.52	0.06	0.01	110.2	26.8	328.9	9	289.9	5	7.1
KS10-KISS-17	76.51	4.37	4.09	0.08	0.2	0.11	0.55	0.95	0.06	0.01	15.6	4.8	79.8	4	257.6	10.9	83.4
KS10-KISS-19	60.77	1.72	8.95	0.04	0.08	0.07	0.35	0.82	0.1	0	9.8	5.4	148.4	6	174.1	7.3	108.8
KS10-VA-3	59.61	11.82	4.7	0.38	0.94	0.88	3.01	0.78	0.18	0.06	11	6.8	34.5	8	180.5	7.7	6.5
KS10-VA-4	50.66	19.48	3.89	0.38	1.09	2.29	3.19	0.53	0.16	0.04	3.3	1.9	9	6	165.3	7.6	7
KS10-VA-7	62.09	6.79	10.54	0.34	0.89	0.36	1.84	0.95	0.11	0.05	85.5	20.5	76.4	21	204.1	7.8	36.4
KS10-VA-9	59.18	17.98	1.37	0.11	0.31	0.39	2.36	0.71	0.18	0.02	1.4	0.9	13.9	2	186	8.1	6.6
KS10-VA-13	76.76	2.61	7.06	0.11	0.18	0.09	0.33	0.94	0.04	0.05	6.5	4.1	163.2	13	285.1	11.3	15.7
KS10-VA-15	43.38	11.19	11.15	0.02	0.03	0.32	2.83	0.49	0.2	0	23.3	6.4	164.8	2	148.8	5.5	26.2
KS10-VA-23	47.17	4.31	20.08	0.02	0.07	0.04	0.08	0.54	0.06	0	39.1	9.4	55.5	6	237.8	6.2	4
KS10-VB-1	79.08	7.14	2.15	0.28	0.77	0.24	1.97	0.85	0.08	0.04	3.8	2.1	11.2	2	206.1	10.7	5.3
KS10-VB-2	75.27	8.67	2.43	0.25	0.72	0.17	2.05	0.87	0.08	0.04	4	2.1	10	3	254.7	11.2	5
KS10-VA-10B	74.52	2.47	4.06	0.04	0.15	0.12	0.32	1.08	0.05	0	4.7	2	20.7	3	231.6	10.3	5.1
KS10-VC-2	82.1	2.26	1.38	0.14	0.26	0.21	0.48	0.74	0.05	0.02	3.2	1.8	30.7	2	134.6	7.9	2.6
KS10-VC-3	84.95	1.24	0.68	0.11	0.13	0.09	0.14	0.24	0.03	0.01	2.5	1.2	5.2	2	80.4	3.7	1.2
KS10-VC-4	87.17	1.57	1.5	0.03	0.09	0.17	0.23	0.48	0.03	0	10.1	1.9	47.8	1	390.6	13.4	2.9
KS10-VC-5	80.51	5.16	1.31	0.05	0.29	0.04	0.81	1.23	0.1	0.02	2.7	2.3	25.6	3	241.4	12	2.1
KS10-VC-9	87.9	0.36	0.63	0.05	0.05	0.05	0.07	0.23	0.04	0	3.6	1.7	12.2	2	191.3	10.4	34.4
KS10-VC-11	81.14	1.95	0.6	0.06	0.07	0.07	0.42	1.59	0.06	0	2.8	2.7	18.9	2	386.7	11	7.7

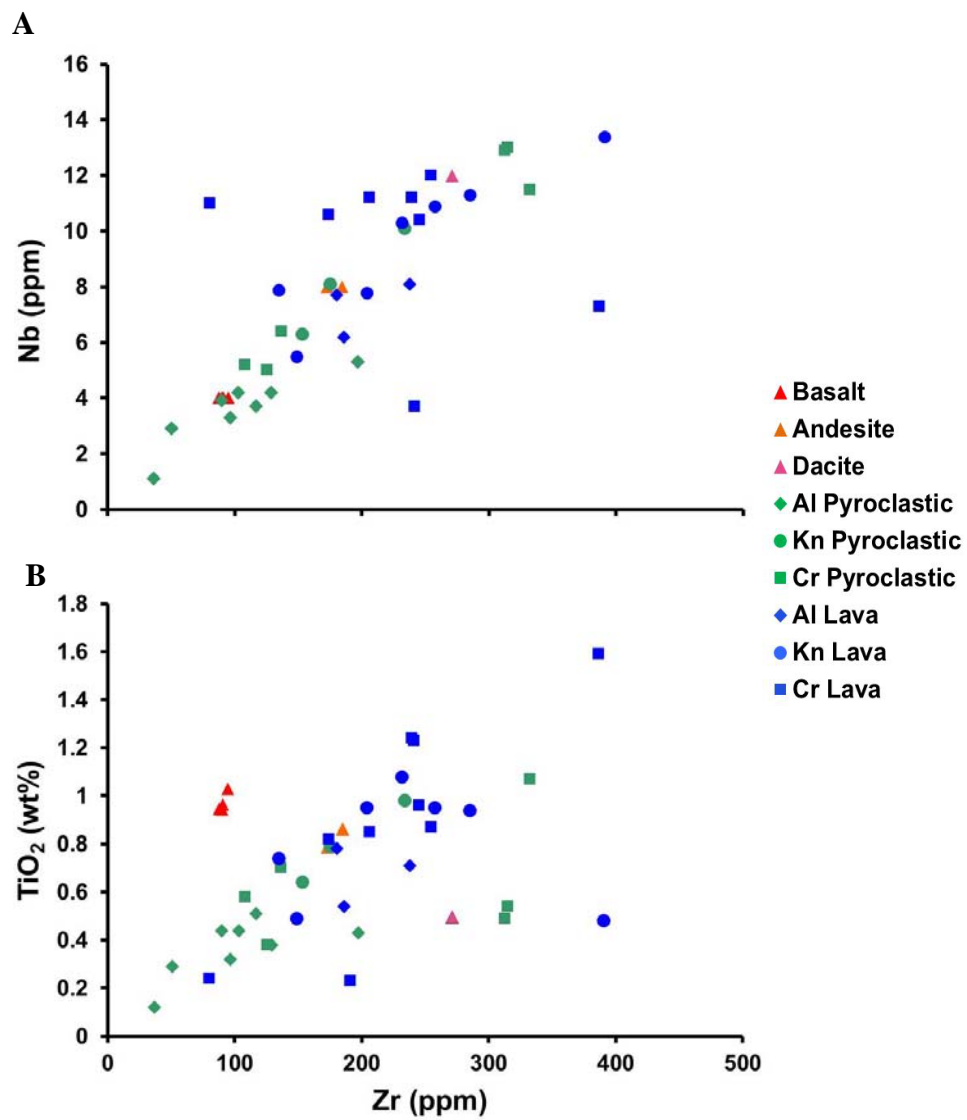


Fig. 7. Plots of (a) Nb vs Zr and (b) TiO₂ vs Zr showing the compositions of altered and unaltered volcanic rocks from the Kawah Ijen crater. Both diagrams illustrate broad linear distributions of the data that pass through the origin, suggesting that the element pairs were immobile, and that their ratios were therefore unaffected by alteration. However, whereas the compositions of unaltered basalt, andesite and dacite all form part of this linear distribution in (a), among these samples only the composition of unaltered andesite is part of the distribution in (b). The latter distribution therefore identifies andesite as the protolith for most of the altered rocks. A few samples lie close to a line that passes from the origin through the composition of dacite, indicating that this rock was the protolith for some altered samples. Finally, none of the altered samples have compositions along a line passing from the origin through the composition of basalt, demonstrating that this rock did not act as a protolith for any of the altered samples. The abbreviations in the legend are as follows: 'Al' for alunite, 'Kn' for kaolinite, and 'Cr' for cristobalite; 'pyroclastic' and 'lava' refer to rocks with either pyroclastic or lava protolith. See the main text for further details.

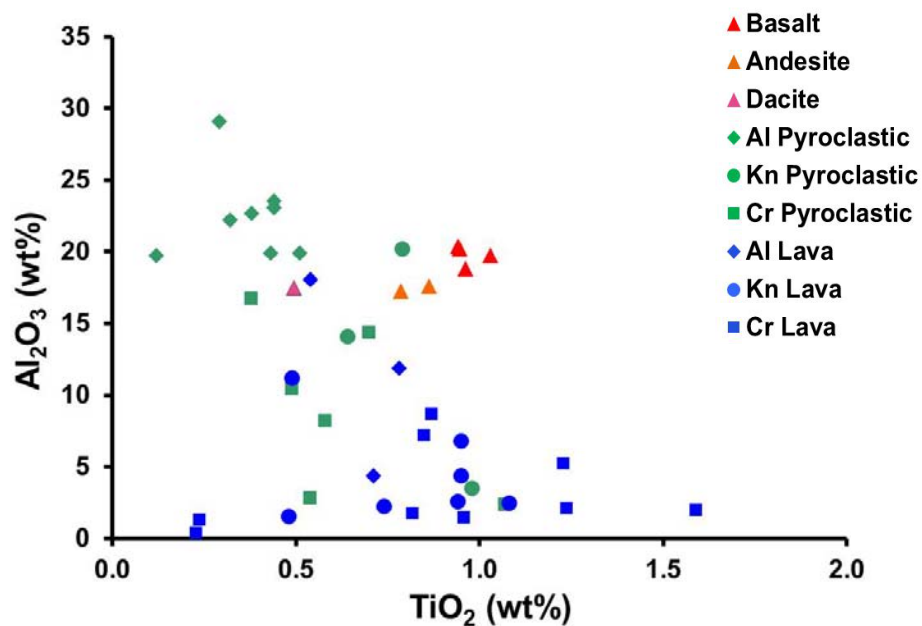


Fig. 8. A plot of the content of Al_2O_3 versus that of TiO_2 in altered and unaltered volcanic rocks from the Kawah Ijen crater. The data define a trend of broadly increasing Al_2O_3 with decreasing TiO_2 and therefore indicate that Al_2O_3 was not immobile during alteration. Samples with low Al_2O_3 content are dominantly cristobalite-altered, whereas those with high Al_2O_3 content are dominantly alunite-pyrite-altered, suggesting that Al was leached from the residual silica (cristobalite) zone and re-concentrated in the alunite-pyrite. The abbreviations are the same as in Figure 7.

andesite/trachyandesite; a few of these samples plot close to the corresponding line for trachydacite.

Mass losses and gains were calculated by normalizing the concentration of all elements in the altered rocks to a constant Zr concentration corresponding to that of the unaltered andesite (Zr was selected because it is less mobile than Ti), or in a few cases dacite (four altered samples were determined to have a dacite protolith). The absolute mass gain or loss of an element was determined from the difference between this corrected concentration and its concentration in the unaltered rock. Percentage enrichment and depletion was also calculated. With a few exceptions, there were major depletions in all major element oxides and trace metals (Co, Ni, Cu, Zn, and Pb) in the three alteration facies of lava (Fig. 9a). The exceptions were an enrichment in SiO₂ in the cristobalite facies (30%) and Fe₂O₃ (30%) in the alunite facies, a somewhat stronger enrichment in Cu (46%) in the kaolinite/dickite facies and strong enrichments in Pb in the cristobalite (141%) and kaolinite/dickite (95%) facies; for a few elements the mass change in particular facies was close to zero. Like the lavas, the pyroclastic/epiclastic rocks were depleted in most elements and on a similar scale, with the important exception of the alunite facies (Fig. 9b). This facies is marked by strong enrichments in Al₂O₃ (202%), Fe₂O₃ (69%), K₂O (163%) and P₂O₅ (117%). As in the lavas, Pb was strongly enriched in the cristobalite (79%) and particularly the kaolinite facies (287%) and, in addition, was also very strongly enriched in the alunite facies (330%); Zn was significantly enriched in the cristobalite facies (49%) and Co in the alunite facies (22%).

5.2. *Alunite chemistry*

Most of the alunite grains were too small for reliable analysis with the electron microprobe (they were generally less than 20 microns in diameter) and, where large enough in plan view, they commonly were not thick enough to analyze reliably (many were so thin that the polishing process had produced holes in them). Furthermore, none of the thin sections that were prepared contained a mono-mineralic alunite groundmass, thereby further limiting analysis of alunite composition. Consequently, analyses were restricted to a small number of relatively

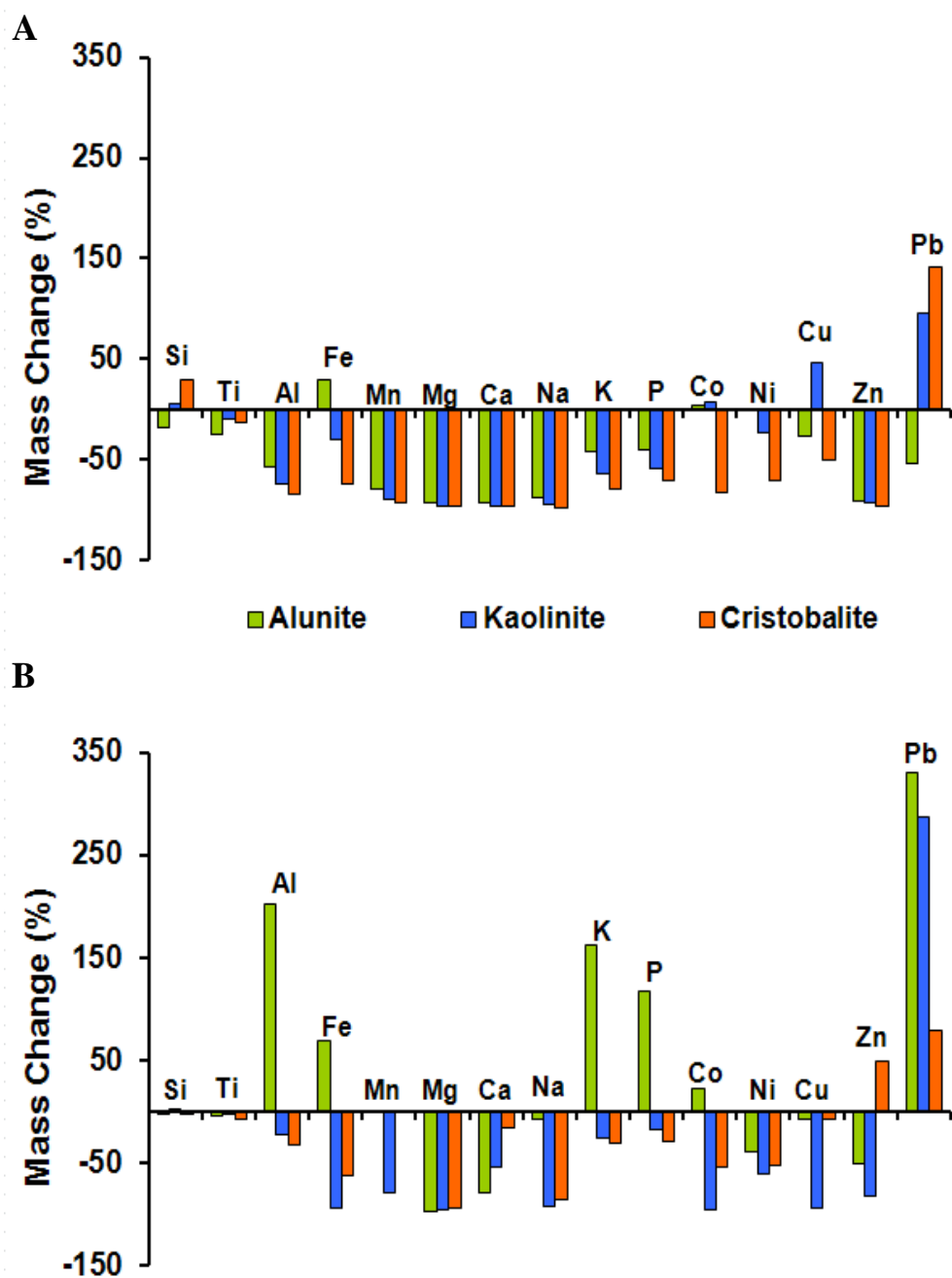


Fig. 9. Diagrams showing relative mass changes for cristobalite-, alunite-pyrite- and kaolinite-altered rocks; a) altered lavas; b) altered pyroclastic rocks.

thick, bladed crystals (Fig. 6a). A total of 20 crystals were analyzed in two thin sections (KV08-204C and KV08-2). The crystals contain between 1.68 and 5.59 wt% Na, 2.02 and 7.78 wt% K, <0.07 wt% Fe, and <0.3 wt% Ca (Table 4). Except for five crystals, the K/Na ratio of the alunite is >1. Significantly all the Na-rich alunite crystals (five crystals) occur in the same sample (KV08-2); five other alunite crystals in this sample were shown to be K-rich; none of the crystals in this sample have intermediate compositions. This indicates that there were separate generations of natroalunite and alunite.

5.3. *Pyrite chemistry*

A total of 255 pyrite crystals in 11 thin sections were analyzed with the electron microprobe for Fe, S, As, and Cu (Table 5 and Appendix V) and shown to contain detectable concentrations of these elements. Based on these results a further 228 grains in 14 thin sections were analyzed for Co, Ni, Cu, Zn, As, Se, Mo, Ag, Cd, Sn, Sb, Te, Au, Hg, Tl, Pb, and Bi using LA-ICP-MS (Table 1 and Appendix II). The analyzed grains were cubic or ovoid in shape and ranged from ~20 μm to 138 μm in diameter. They were analyzed by spot ablation or by ablating tracks across the surface of the grain.

Pyrite, whether it is disseminated or occurs in veins, contains detectable concentrations of all the trace metals analyzed. Moreover, the concentration levels are independent of the mode of occurrence of the pyrite. Copper and As are the elements in highest concentration (up to 6,800 ppm and 3,430 ppm, and on average, 1,335 ppm and 515 ppm, respectively). The contents of Se and Te are also relatively high, on average 113 ppm and 26 ppm, and up to 1476 ppm and 274 ppm, respectively. Most significantly for this study, the pyrite has detectable concentrations of Ag and Au. These reach up to 9.2 ppm and 192 ppb, and average 0.6 ppm and 20 ppb, respectively. Several metals, notably Mo, Bi, Pb, and Zn, produced large spikes in some of the laser profiles, likely reflecting the presence of inclusions of molybdenite, bismuthinite, galena, and sphalerite. These minerals were not found in thin section, which does not mean that they are not present in the altered rocks or pyrite veins, but rather that their grains are so small that they

Table 4: Composition (wt%) of alunite crystals from the alteration center at Kawah Ijen based on EMP analyses.

	Na ₂ O	Al ₂ O ₃	K ₂ O	SO ₃	FeO	CaO	Total
KV08-204C	1.79	34.6	7.63	36.0	0.036	0.075	80.06
	2.46	34.2	7.10	35.7	0.037	0.070	79.51
	2.16	34.2	7.12	35.7	0.007	0.080	79.21
	1.93	34.6	7.60	36.7	0.030	0.064	80.84
	1.68	34.4	7.78	36.6	0.000	0.121	80.58
	2.61	34.0	6.48	35.2	0.000	0.133	78.39
	1.79	34.5	7.75	36.7	0.016	0.098	80.85
	1.80	34.1	7.64	35.4	0.000	0.306	79.20
	1.71	34.3	7.76	35.7	0.046	0.127	79.63
	1.55	34.4	7.78	35.5	0.041	0.154	79.48
KV08-2	2.75	34.8	7.01	36.5	0.000	0.028	81.15
	2.74	34.9	6.97	36.4	0.019	0.000	81.05
	2.44	34.7	7.16	36.2	0.010	0.037	80.54
	2.45	34.8	7.62	36.7	0.067	0.020	81.61
	2.87	35.1	6.86	37.3	0.012	0.023	82.21
	4.85	35.5	3.27	37.4	0.036	0.143	81.24
	5.59	36.0	2.25	38.4	0.058	0.067	82.36
	4.47	34.9	3.35	37.5	0.051	0.234	80.48
	4.85	35.5	3.13	36.3	0.045	0.313	80.18
	4.62	32.2	2.02	33.3	0.043	0.248	72.44

Table 5: Representative compositions of pyrite grains from the altered rocks at Kawah Ijen based on EMP analyses. Major element oxides are reported in wt% and trace elements in ppm.

	As	Cu	Se	Te	SO ₃	FeO
KS09-VA9	705	500	n.d.	n.d.	53.1	46.5
KS09-C4	530	480	n.d.	n.d.	52.1	46.2
KS09-C5	620	1208	233	n.d.	52.8	46.5
KS09-C2	520	1060	n.d.	n.d.	53.4	46.5
KS09-C3	726	627	332	426	52.5	45.6
KS10-KISS-7	410	633	n.d.	n.d.	53.7	46.2
KS10-VA20	315	430	2000	n.d.	52.7	46.5
KS10-VA15	490	1019	n.d.	n.d.	53.6	45.9
KS10-VA23	n.d.	500	n.d.	n.d.	54.0	46.5
KS10-VB5A	530	n.d.	n.d.	n.d.	53.8	46.4
KS10-SFM-1	n.d.	n.d.	n.d.	n.d.	52.6	46.0

*n.d. indicates that the element was not detected.

escaped identification even with the electron microprobe. Considering that As, Cu, Te, and Se have been interpreted to control incorporation of Au and Ag in pyrite, the data for these elements were analyzed for inter-element correlations (e.g. Chouinard et al., 2005a; Deditius et al., 2008). From Figure 10, it is evident that Au correlates positively with Cu, As and Ag. Silver correlates positively with Cu and As, and Cu correlates positively with As (Fig. 11).

5.4. Sulfur isotopes

The sulfur isotopic composition of pyrite and alunite was analyzed in four samples (KS09-11A, KS10-VC7, KS10-13W, and KS10-SFM-1). Values of $\delta^{33}\text{S}$, $\delta^{34}\text{S}$ and $\delta^{36}\text{S}$ for pyrite range from -0.02 to -0.03, -3.99 to -6.40 and -0.64 to -0.81, respectively; the average values are -0.02, -4.97 and -0.71, respectively. The corresponding ranges of $\delta^{33}\text{S}$, $\delta^{34}\text{S}$ and $\delta^{36}\text{S}$ for alunite are -0.02 to -0.06, 18.02 to 21.74 and -0.05 to -0.60, respectively; they average -0.04, 19.28 and -0.41, respectively (Table 6). It should be noted that as natroalunite and alunite may be both present in the same sample (e.g., KV08-2, see above), it is possible that the isotopic compositions reported here for alunite, represent compositions for a mixture of alunite and natroalunite.

6. Gas and Sublimate Composition

The composition of the volcanic gas collected from six fumaroles located on top of the active dome (their temperature ranged from 330 to 495 °C) was analyzed for H_2O , CO_2 , SO_2 , H_2S , N_2 , HCl , HF , He , H_2 , Ar , O_2 , and CH_4 (Table 7 and Appendix VI). The concentrations of the major species, i.e., H_2O , CO_2 , SO_2 , H_2S , and N_2 , ranged from 94.92 to 98.75 wt%, 0.92 to 3.88 wt%, 0.27 to 0.74 wt%, 0.021 to 0.71 wt%, and 0.014 to 0.117 wt%, and averaged 95.28, 3.51, 0.49, 0.689, and 0.022 wt%, respectively. The minor gas species, i.e., HCl , HF , He , H_2 , Ar , O_2 , and CH_4 , ranged in concentration from 64 to 219 ppm, 0.67 to 9.9 ppm, 5 to 19 ppb, 0.07 to 0.24 ppm, 1.7 to 12.6 ppm, 0.08 to 3.44 ppm, and 1 to 79 ppb and averaged 113, 2, 0.015, 0.2, 1.8, 0.2, and 0.01 ppm, respectively. In addition to the sampling of the fumarolic gases, the total SO_2 flux from the crater (mainly from the active dome)

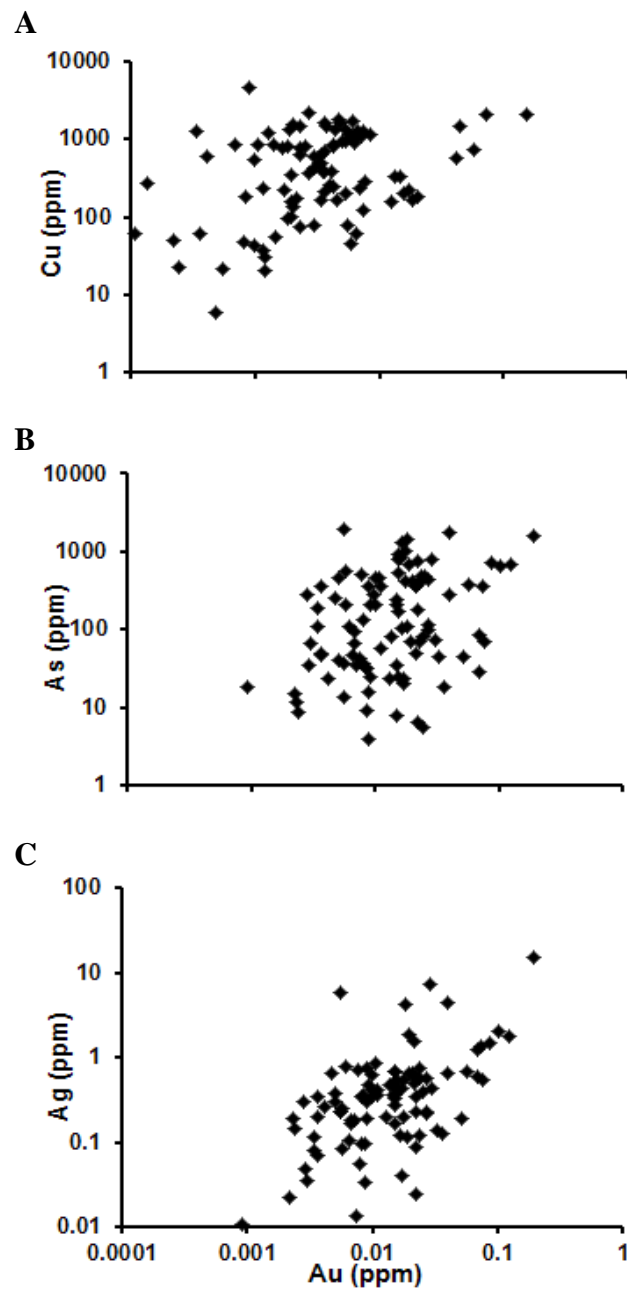


Fig. 10. Binary diagrams showing the distribution of Au, Ag, Cu, and As in pyrite; a) Au vs. Cu, b) Au vs. As, c) Au vs. Ag.

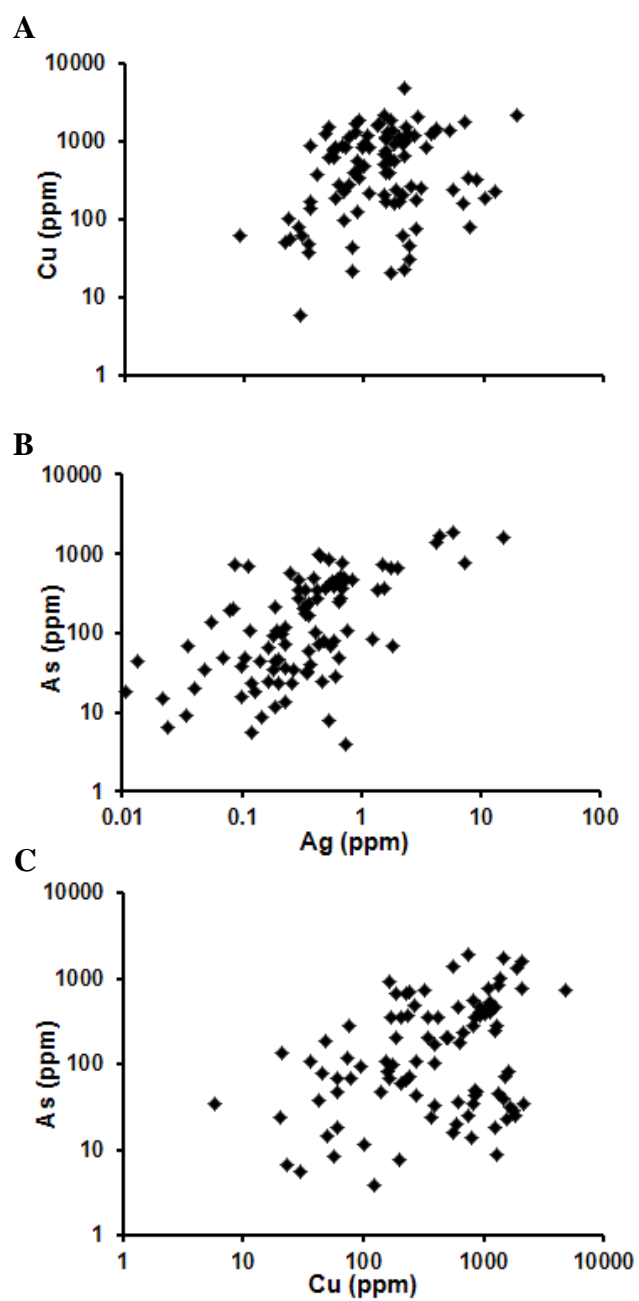


Fig. 11. Binary diagrams showing the distribution of Ag, Cu and As in pyrite;
a) Ag vs. Cu, b) Ag vs. As, c) Cu vs. As.

Table 6: Sulfur isotope compositions of alunite-pyrite pairs in altered rocks from the Kawah Ijen crater. Temperatures were calculated based on the geothermometer of Ohmoto and Rye (1979).

Sample	Mineral	$\delta^{34}\text{S}$	$\delta^{33}\text{S}$	$\delta^{36}\text{S}$	Temperature
KS09-11A	Pyrite	-4.34	-0.03	-0.64	199.9
KS09-11A	Alunite	25.47	-0.02	-0.17	
KS09-13W	Alunite	18.02	-0.05	-0.60	242.5
KS09-13W	Pyrite	-6.40	-0.03	-0.71	
KS10-VC7	Alunite	21.74	-0.06	-0.05	211.6
KS10-VC7	Pyrite	-5.16	-0.02	-0.68	
KS10-SFM1	Alunite	18.09	-0.02	-0.58	301.7
KS10-SFM1	Pyrite	-3.99	-0.02	-0.81	

Table 7: Compositions of fumarolic gases and their condensates at the active dome in the Kawah Ijen crater.

Sample no.	KV07-402	KV07-411	KV07-421	KV08-003	KV08-010	KV08-014	Best estimate	1 σ
Year	2007	2007	2007	2008	2008	2008	2007-2008	
Gas collected (g)	9.61	13.38	9.88	3.86	4.88	8.81		
Temperature (°C)	495	330	335	490	>400	>400		
Major species	g/kg gas	g/kg gas	g/kg gas	g/kg gas	g/kg gas	g/kg gas	g/kg gas	g/kg gas
H ₂ O	987.5	973.5	983	966.8	956.4	949.2	952.8	5.1
CO ₂	9.2	18.8	13.1	25	31.4	38.8	35.1	5.3
SO ₂	2.7	7.4	3.6	3.5	5.3	4.5	4.9	0.5
H ₂ S	0.21	n.d.	0.08	3.5	6.6	7.1	6.89	0.4
N ₂	0.17	0.14	0.14	1.17	0.22	0.22	0.22	0.4
Minor and traces	mg/kg gas	mg/kg gas	mg/kg gas	mg/kg gas	mg/kg gas	mg/kg gas	mg/kg gas	mg/kg gas
HCl	219	115	76	64	134	92	113	29.4
HF	9.9	5.5	2.2	9.7	3.3	0.67	2	0.8
He	0.009	0.009	0.005	0.012	0.012	0.019	0.015	0
H ₂	0.07	0.15	0.1	0.15	0.15	0.24	0.2	0.1
Ar	12.6	6.3	6.23	9.7	1.9	1.7	1.8	0.1
O ₂	0.11	3.44	0.18	0.2	0.08	0.32	0.2	0.2
CH ₄	0.079	0.001	0.001	0.01	0.001	0.019	0.01	0
Si	8.3	132	97	n.a.	n.a.	n.a.	114	25
Na	17	40	66	n.a.	n.a.	n.a.	53	19
Ca	6.5	37	29	54	32	22	32	12
Fe	7.2	11	26	25	17	8	17	8
Al	5.2	16	21	n.d.	n.d.	9	16	6
K	2.4	3.8	15	n.a.	n.a.	n.a.	9.5	8
Mg	1.6	3.3	6.3	10	6.6	2.9	6.3	3
P	1.6	5.4	6.8	n.a.	n.a.	n.a.	6.1	1
As	0.82	3.5	3.8	3.1	2.1	0.9	3.1	1
Cu	1	2	3	3	2	2	2	1
Se	0.36	2.3	2.1	2	2	1	2	1
Ti	0.24	2.6	1.8	2.3	1.6	1	1.8	1
Ni	0.41	1	1.7	1.7	1.3	0.5	1.3	1
Zn	0.28	1	1.3	1.4	1	0.45	1	1
Mn	0.14	n.d.	0.84	2.3	0.68	0.31	0.76	0.9
Te	0.12	0.52	0.61	n.a.	n.a.	n.a.	0.56	0.3
Pb	0.01	0.06	0.07	0.09	0.05	0.03	0.06	0
Trace elements	µg/kg gas	µg/kg gas	µg/kg gas	µg/kg gas	µg/kg gas	µg/kg gas	µg/kg gas	µg/kg gas
Hg	12	56	124	n.a.	n.a.	n.a.	90	48
Sb	10	36	41	39	30	12	36	12
Zr	1	13	8	30	32	31	30	11
Mo	3	43	29	33	20	8	29	13
Tl	2	35	20	34	22	12	22	10
Sn	3	28	18	30	16	17	18	7
Nb	n.d.	5	5	5	4	2	5	1
Co	n.d.	176	48	0.9	1.6	1.4	1.6	76
W	75	62	52	0.2	0.6	0.1	0.6	31

was measured using a portable UV spectrometer (FLYSPEC; Horton et al., 2006) at the crater rim, and was determined to be ~250 tonnes/day (Vigouroux et al., 2009). However, as considerable native sulfur precipitates within the crater, likely as a result of the disproportionation reaction $2\text{SO}_2 + 2\text{H}_2\text{O} \leftrightarrow \text{S} + 2\text{H}_2\text{SO}_4$, the initial SO_2 flux was undoubtedly much higher.

The condensed gases contain ppm to ppb concentrations of As, Cu, Ni, Cr, Pb, and Zn detected (Table 7). Their concentrations ranged from 0.82 to 3.8 ppm, 1 to 3 ppm, 0.41 to 1.7 ppm, 0.91 to 3.1 ppm, 0.01 to 0.09 ppm, and 0.28 to 1.4 ppm and averaged 2.37, 2.17, 1.10, 1.97, 0.05, 0.91 ppm, respectively. Selenium and Te were also detected, ranging in concentration from 0.36 to 2.3 ppm and 0.12 to 0.61 ppm, and averaging 1.63 and 0.42 ppm, respectively.

Quartz tubes were inserted into the high temperature fumaroles in order to induce precipitation of minerals from the gases along their inner walls. The main phase precipitated was native sulfur. There were also subordinate to minor proportions of a variety of sulfate, sulfide, oxide and hydroxide minerals (e.g., alunite: $\text{KAl}_3(\text{SO}_4)_2(\text{OH})_6$, natroalunite: $\text{NaAl}_3(\text{SO}_4)_2(\text{OH})_6$, diaspore: $\alpha\text{-AlO}(\text{OH})$ and pyrite: FeS_2), and halite, together with rare native bismuth.

7. Discussion

7.1. Introduction

The crater of Kawah Ijen volcano, as has already been discussed, is the site of an area of hydrothermal alteration measuring ~500 m in diameter, which has many of the characteristics of the acid-sulfate alteration associated with high sulfidation epithermal precious metal deposits. In addition, pyrite, which is part of an alunite-pyrite alteration facies and also occurs in veins, has elevated concentrations of copper, arsenic, silver and gold. The altered area was exposed after a phreatomagmatic in 1817, which destroyed an active solfatara located vertically above the area of altered rocks, and is now the site of an actively degassing dome. This spatial association of the altered rocks with a paleo-solfatara and an actively degassing dome provide direct evidence that the alteration has been the product of a long-lived interaction of the rocks with condensed volcanic gases. Moreover, as the copper,

silver and gold are hosted by pyrite that formed contemporaneously with advanced argillic alteration (alunite), it also follows that the volcanic gases were responsible for metal transport.

In the sections that follow, we will evaluate the physicochemical conditions that accompanied the alteration, the processes which brought about this alteration and the mechanisms that are leading to the concentration of Cu, Ag and Au. Based on this evaluation, we will then develop a model that will satisfactorily explain the alteration and associated metallic mineralization and, in turn, contribute new understanding of the genesis of acid-sulfate/high sulfidation epithermal systems.

7.2. Pressure – temperature

Reliable estimates of the pressure attending alteration can be made using the observation that the altered rocks are located approximately 230 m below the crater floor present prior to the 1817 eruption. Assuming purely lithostatic conditions, the pressure corresponding to this depth is approximately 75 bars and assuming purely hydrostatic conditions is approximately 25 bars. Given the pervasive nature of the alteration, it is likely that the pressure was generally close to lithostatic, although locally hydrostatic and even vaporstatic conditions would have prevailed, as is evident from the occurrence of fumaroles on the active dome.

Insight into the probable temperature of alteration is provided by the temperatures of the fumaroles on the active dome. These temperatures range from < 200 °C to > 600 °C, but are mainly in the range 250 °C to 350 °C. Additional insight is provided by the stability of the alteration minerals. For example, dickite is stable at temperatures up to 250 °C; kaolinite transforms to dickite in the range 120 °C to 200 °C (Hemley et al., 1980; Reyes, 1989). Evidence that alunite and natroalunite may be present in the same sample places an upper temperature limit for the alteration of <350 °C; at higher temperature, there is a complete solid-solution between alunite and natroalunite, thereby precluding crystallization of more than one alunite phase (Stoffregen and Cygan, 1990).

As alunite and pyrite have been shown to be in textural equilibrium (Fig. 6b), and isotopic equilibrium was demonstrated by the high degree of correlation

between $\delta^{34}\text{S}$ and $\delta^{33}\text{S}$ in samples of the two minerals (within error, $\Delta^{33}\text{S}$ values are the same for both minerals; Farquhar and Wing, 2003) it was possible to estimate the temperature of alteration directly from the sulfur isotopic fractionation between these minerals. The alunite-pyrite geothermometer of Ohmoto and Rye (1979) was used for this purpose and yielded temperatures ranging from 200 to 302 °C; the average temperature estimated for these samples is 249 °C, however, three of the four samples analyzed yielded temperatures between 200 and 243 °C (Table 6). Based on the above discussion, we conclude that the pressure and temperature conditions of alteration were approximately 50 bar and 225 °C, respectively.

7.3. $f\text{O}_2$ and pH

Oxygen fugacity and pH were estimated by evaluating stability relationships among the principal alteration minerals, assuming conservation of alumina (some error will have been introduced because of the demonstrated mobility of Al; Fig. 8) and saturation of the system with silica (cristobalite). The values for the total sulfur content (ΣS) and the concentration of K^+ were taken to be 0.14 m and K^+ 0.0002 m based on the composition of the volcanic gas sampled at fumaroles. Thermodynamic data for the minerals, aqueous species and water were taken from the HCh Unitherm database (Helgeson et al., 1978; Johnson et al., 1992; Robie and Hemingway, 1995; Shock et al., 1997; Holland and Powell, 1998; Stoffregen et al., 2000). The pressure-temperature conditions used in the calculations were 50 bars and 225 °C. Using the above assumptions and data sources, a log $f\text{O}_2$ -pH diagram (Fig. 12 and Appendix VII) was constructed showing the stability fields of pyrite, pyrrhotite, hematite, magnetite, native sulfur, alunite, kaolinite, muscovite, and K-feldspar.

The pH and $f\text{O}_2$ conditions at which the advanced argillic and argillic alteration zones formed can be inferred from the stability fields for the corresponding minerals. Although the conditions of formation of residual silica cannot be estimated directly, the pH needed to leach elements including Al can be assumed to have been less than that of alunite-pyrite stability. It can likewise be assumed that kaolinite formed at higher pH than alunite-pyrite. From Figure 12, it is evident that

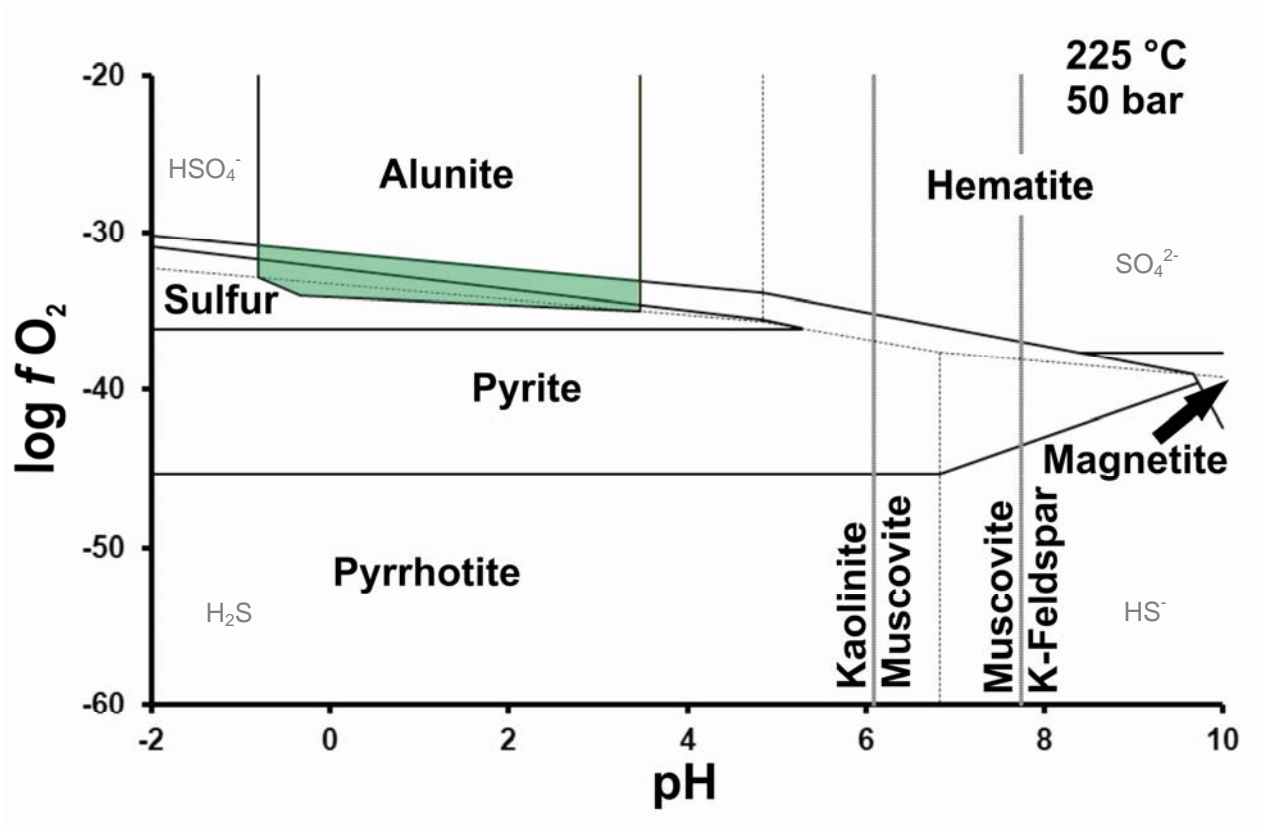


Fig. 12. $\log fO_2$ -pH diagram showing stability relationships for minerals in the system K-Al-Si-O-H and Fe-S-O at Kawah Ijen at 225 °C, 50 bar, $K^+ = 0.0002$ and $\Sigma S = 0.14$ (based on the measured composition of condensed vapor; Table 6). Thermodynamic data for the minerals were taken from Holland and Powell (1998), Stoffregen et al. (2000), Helgeson et al. (1978) and Robie and Hemingway (1995) and the aqueous species from Johnson et al. (1992) and Shock et al. (1997). The green area identifies the conditions at which alunite and pyrite can coexist. See the main text for further details.

the assemblage alunite-pyrite is stable at a pH between -0.8 and +3.7 and a $\log f\text{O}_2$ between -30.8 and -35. However, as the pH of the fumarolic gases is ~ -0.5 , and these gases likely record the fluid-buffered pH, it is reasonable to conclude that this value represents the lowest pH attained during alteration, i.e., that of residual silica alteration. The advanced argillic alteration must therefore have occurred at higher pH and argillic alteration at even higher pH; kaolinite and dickite are stable from a pH < 6.07 . The overall conclusion from this analysis of the alteration is that conditions were extremely acidic, as low as -0.5 and very oxidizing, above those of the hematite-magnetite buffer.

7.4. *Fluid-rock interaction*

We consider the extreme leaching represented by the cristobalite zones mapped in Figure 4 to be the product of a condensed vapor similar in composition to the gas currently being expelled at the active dome. These zones are therefore interpreted to represent conduits for condensing vapors, around which the fluids interacted with the rock at progressively lower fluid/rock ratio and correspondingly higher pH to produce proximal alunite-pyrite and distal kaolinite alteration zones (Fig. 4).

The fluid-rock interaction led to the removal of Al, Fe, Mg, Ca, Mn, Na, K, P, Co, Ni, and Cu from the residual silica (cristobalite) zone and the addition of Al, Fe, K, P, Co, and Pb in the alunite-pyrite alteration zone, Co, Cu, and Pb in the kaolinite alteration zone and Zn and Pb in the residual silica zone; other elements were either leached in these latter zones or underwent no significant mass change (Fig. 9). The rocks that experienced mass gain were predominantly of pyroclastic origin (exceptions are restricted to a mass gain in Fe in alunite-pyrite-altered lavas, Cu and Pb in kaolinite-altered lavas and Si and Pb in cristobalite-altered lavas). The considerable enrichment of Al, Fe, K and P in pyroclastic rocks of the alunite-pyrite zone and their depletion in the residual silica zone provide clear evidence of the mobilization of these elements from the latter zone into the alunite-pyrite zone where they were re-deposited as alunite and pyrite (Fe), largely as a result of the higher pH that accompanied the lower fluid/rock ratio. The lack of a similar enrichment in the kaolinite zone indicates that the alunite-pyrite zone was an

effective sink for these elements, and that the activity of species involving them was therefore low in fluids entering the more distal kaolinite facies. Significantly, the large enrichment of Al, Fe, K and P in pyroclastic rocks of the alunite-pyrite zone was not duplicated by lavas subjected to alunite-pyrite alteration. The reason for this is not clear, but may reflect the very much lower porosity and permeability of the lavas compared to the pyroclastic rocks.

The behavior of the ore metals, Cu, Zn and Pb is curious. As might be expected, Pb was added to all alteration zones and its concentration was highest in the alunite-pyrite and kaolinite zones (much of the Pb added from the fluid in the residual silica zone would have been remobilized to the surrounding alteration zones). However, it is surprising that Zn and particularly Cu was not added to the alunite-pyrite zone. We believe that this is an artifact of our decision to remove the heterogeneously distributed pyrite from the rock prior to analysis. This pyrite would have contained most of the Cu that was added to the alunite-pyrite zone and likely much of the Zn (large spikes in Zn were observed during LA-ICP-MS analyses of pyrite and are attributed to sphalerite inclusions). We therefore believe that there was a large transfer of Cu and a small transfer of Zn (absolute Zn concentrations in all bulk rocks are very low; Table 2 and Appendix III) from the fluid to the rock and that this occurred largely in the alunite-pyrite zone where conditions were appropriate for the deposition of pyrite. The large addition of Pb to both the alunite-pyrite and kaolinite alteration zones indicates that it was concentrated in a mineral other than pyrite; alunite, which has been reported elsewhere to contain significant Pb (Dill, 2003) is a possibility for the alunite-pyrite zone.

In order to better understand the effects of progressive fluid-rock interaction on the changing alteration mineralogy, (cristobalite, alunite, dickite, and pyrite), the alteration process was simulated by adding ~1 millimole aliquots of aqueous liquid with the composition of the condensed fumarolic gas to 1 kilogram of rock with the composition of Kawah Ijen andesite and dacite (separate simulations). The system was brought to equilibrium after the addition of each aliquot of liquid (the composition of the fluid and rocks are reported in Table 8). The simulation was carried out using HCh modeling software (Shvarov, 2008) and assumed a pressure

Table 8: Composition of the fluid and rocks used in the simulation of fluid-rock interaction presented in Figure 13.

Species	Fluid (mmol)	Andesite (wt%)	Dacite (wt%)
H ₂ O	9.53E-01	-	-
CO ₂	3.51E-02	-	-
H ₂ S	2.50E-03	-	-
SO ₂	2.50E-03	-	-
HCl	1.80E-04	-	-
SiO ₂	-	58.47	64.23
TiO ₂	-	0.80	0.49
Al ₂ O ₃	-	17.34	17.42
Fe ₂ O ₃	-	7.67	4.04
MnO	-	0.15	0.09
MgO	-	2.85	1.12
CaO	-	6.34	4.17
Na ₂ O	-	3.50	4.03
K ₂ O	-	2.65	3.80
P ₂ O ₅	-	0.19	0.11

of 50 bar and a temperature of 225 °C (the thermodynamic data sources for the minerals were Robie and Hemingway, 1995; Holland and Powell, 1998 and Stoffregen et al., 2000; for the aqueous species data was taken from Robie and Hemingway, 1995 and Robie et al., 1978). As cristobalite is metastable at the assumed conditions of alteration, it was replaced by quartz in the simulation.

Results of the fluid/rock interaction model are presented in Figure 13 and illustrate the alteration of andesite (Fig. 13a) and dacite (Fig. 13b) in plots of the number of moles of secondary minerals produced as a function of reaction progress (the number of aliquots with which the rock has reacted). As fluid was added to rock, the fluid/rock ratio increased with reaction progress. Consequently, conditions at the conduit, (i.e., the residual silica or cristobalite zone) are represented by the right side of the diagrams and those most distal from it, i.e., the kaolinite/dickite zone by the left side.

According to the above model and consistent with field observations and Rietveld analysis of X-ray diffractograms, quartz (cristobalite) was the dominant mineral to crystallize in the residual silica zone (Fig. 13a and b). It was also the dominant mineral in the other zones, although as expected its proportion decreased progressively through the alunite-pyrite and kaolinite zones. Somewhat surprisingly, kaolinite and alunite were also predicted to form in the residual silica zone and even more surprisingly kaolinite was predicted to form in even greater proportions than alunite. However, the predicted proportions are very much smaller than those of quartz, and both these minerals are observed in small proportions in Rietveld analyses of the X-ray diffractograms for samples from the residual silica zones. Very surprisingly, the proportions of alunite and kaolinite predicted to form at more advanced stages of alteration remain low. On the other hand, as expected, alunite formation was predicted to be restricted to very low pH in both andesite and dacite, i.e., from -0.5 (the starting pH of the fluid) to 1.7. Kaolinite (also as expected) was predicted to persist to relatively high pH.

The model predicted pyrite to form only after fluid-rock interaction had driven pH to a value of 0.41 in andesite and 0.89 in dacite. This is because a_{H_2S} was initially too low to permit pyrite to form and had to be driven to higher values by

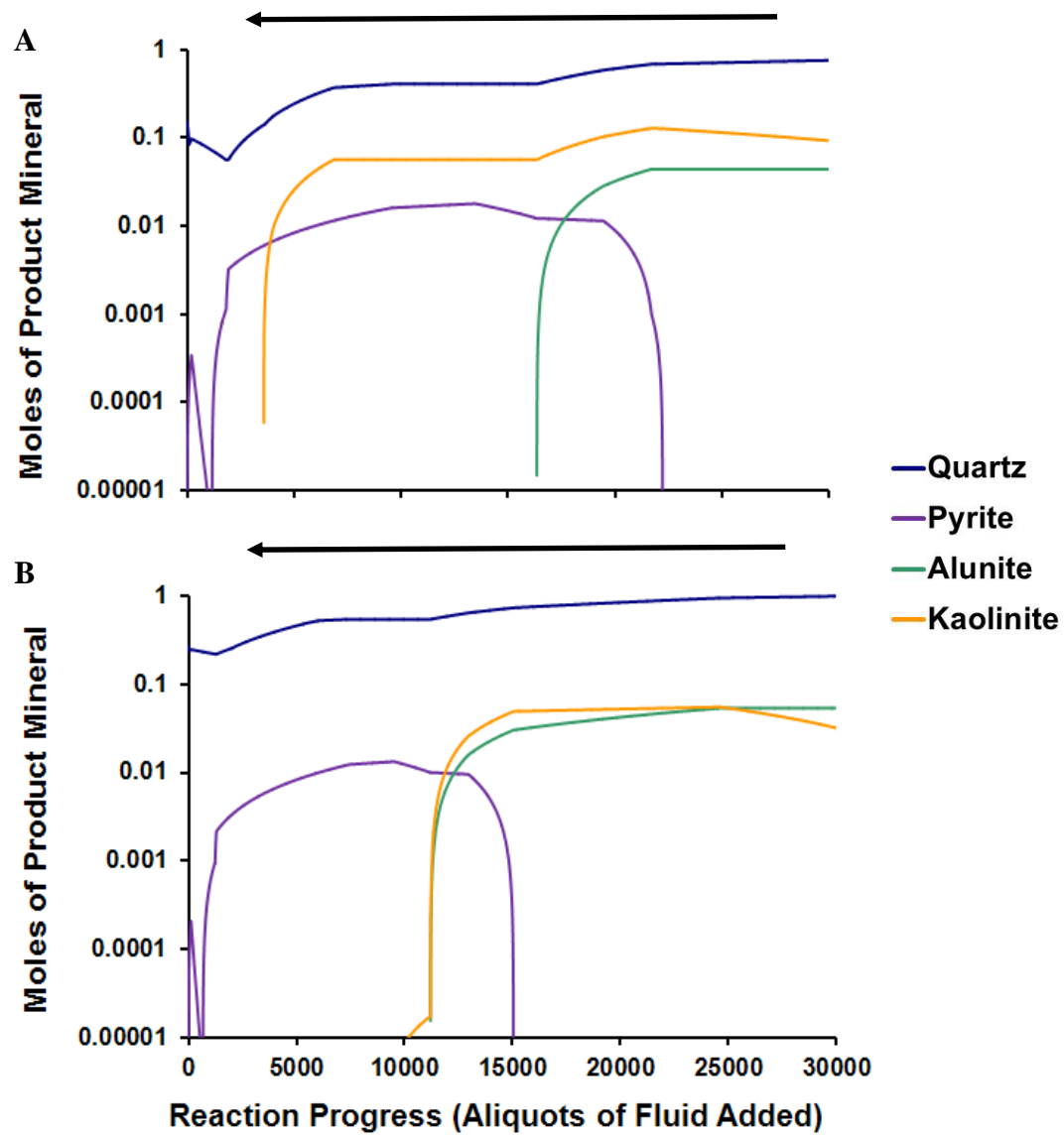


Fig. 13. A plot of the moles of minerals produced versus reaction progress (measured by the number of aliquots of fluid added to the rock) based on a simulation of the interaction of condensed vapor with andesite (a) and dacite (b) at a temperature of 225°C and 50 bar pressure. The simulation was carried out using HCh modeling software (Shvarov, 2008). Thermodynamic data for pyrite was taken from Robie and Hemingway (1995), for quartz and kaolinite from Holland and Powell (1998) and for alunite was taken from Stoffregen et al. (2000). Corresponding data for the aqueous species HCl, H₂S and SO₂ were taken from Robie and Hemingway (1995) and for H₂O and CO₂ from Robie et al. (1978). One millimole aliquots of fluid were added progressively to one mole of rock. The left side of the diagram therefore illustrates the mineralogy of the altered rock at low fluid/rock ratio and high pH, and the right side the mineralogy at high fluid/rock ratio and low pH. The starting composition of the andesite, dacite and condensed vapor are reported in Table 8.

buffering the fluid to lower $f\text{O}_2$ through interaction with ferrous iron in the rock. Indeed, the relatively high content of ferrous iron in andesite relative to dacite explains why pyrite formation occurred earlier in the andesite than in the dacite. Although pyrite was predicted to form at significantly higher pH than the starting pH of the fluid, this pH is nevertheless very low and reflects conditions when leaching would have been dominant, i.e., conditions favorable for the formation of residual silica. This predicted formation of pyrite at low pH is consistent with the observation that despite its much greater importance in the alunite-pyrite alteration facies, pyrite is also commonly observed in textural equilibrium with cristobalite. The model successfully predicts the observed overlap of alunite and pyrite. However, the predicted proportions of both minerals are considerably lower than was expected from the observation that these are the dominant minerals in the alunite-pyrite zone. Moreover, the model predicts a much greater overlap of pyrite with kaolinite, whereas pyrite is a minor mineral in kaolinite-altered rocks.

In summary, the model successfully predicted formation of the main alteration minerals quartz (cristobalite), alunite, pyrite and kaolinite, but although it partly explained their distribution in the different alteration facies, it greatly overestimated the importance of quartz in the alunite-pyrite and kaolinite zones. Most importantly, it failed to explain the dominance of alunite and pyrite in the alunite-pyrite zone and the increasing importance of kaolinite with increasing buffering of the fluid by the rock. We believe the explanation for these failures lies in our assumption of a constant temperature and the very narrow range of $f\text{O}_2$ over which alunite and pyrite are stable (Fig. 12). Our measurement of the temperatures of individual fumaroles showed that they could vary by more than 100 °C over a period of hours to days. Furthermore fluid fluxes varied greatly from one fumarole to the next. These variations make it likely that the field of stability of alunite-pyrite varied considerably in size and that in turn, conditions may have favored alunite-pyrite formation more strongly than predicted by a fixed set of starting conditions. Finally, we note that temperature would have decreased as the fluid moved from the residual silica conduit to the proximal alunite-pyrite zone and particularly the distal kaolinite zone. Nonetheless, we cannot rule out the possibility that the failure to predict high

concentrations of alunite and pyrite and an increase in kaolinite formation with decreasing fluid/rock ratio may be an artifact of the thermodynamic data employed in the model.

7.5. *Transport and deposition of metals*

In addition to altering the rocks at Kawah Ijen, the condensed vapors also served as the agent for metal transport (concentrations of Cu and As in condensed fumarolic vapors sampled at the active dome reached 3 ppm and 3.8 ppm, respectively). We propose that the metal-bearing vapors transported Au, Cu and Ag as hydrated sulfide or chloride gas species and condensed ~ 250 m beneath the floor of the pre-1817 crater. Given the extreme acidity of the condensed liquid, the metal speciation in this fluid is likely to have been dominated by negatively charged or neutral species, e.g., AuCl_2^- or AuHS^0 in the case of gold (Williams-Jones et al., 2009).

Although Au-, Ag- and Cu-bearing phases were undersaturated in the condensed liquids, these metals were able to concentrate in the rocks by adsorbing onto the surface of the growing pyrite crystals in the alunite-pyrite alteration zone. Adsorption was facilitated by the uptake of As, which caused pyrite crystals to develop p-type semi-conductive properties (Prokhorov and Lu, 1971; Mironov et al., 1981; Starling et al., 1989; Möller and Kerten, 1994). The negatively charged species would have been attracted to the positively charged pyrite surfaces. There they would have incorporated in the pyrite, either by electrochemical reduction of the positively charged metal in the species, to form native metal nano-particles or perhaps through coupled substitution of Cu^+ , Ag^+ and Au^+ with As^{3+} for Fe^{2+} . Neutral species would have been in more random contact with the pyrite surfaces but once there the incorporation mechanisms would have been the same. Both these mechanisms are consistent with the positive correlation of Cu, Ag and Au concentrations in pyrite with that of As (Figs. 10 and 11). However, the coupled substitution mechanism, although satisfactorily explaining the uptake of Ag and Au, does not explain that of Cu. The extreme enrichment of Cu (up to 6,800 ppm), and the much lower concentration of As (up to 3,430 ppm) make it more likely that Cu

would have been incorporated as Cu^{2+} through direct substitution for Fe^{2+} , as suggested by Chouinard et al. (2005a).

7.6. Model for alteration and pyrite enrichment at Kawah Ijen

Highly acidic and oxidizing volcanic vapors exsolved from a magma body at depth were responsible for the acid-sulfate alteration and high sulfidation mineralization exposed in the crater of Kawah Ijen volcano. Upon reaching the epithermal environment (at a depth of 250 m or a pressure of 50 bar), the vapors condensed at a temperature of $\sim 225^\circ\text{C}$, generating a highly acidic liquid (pH ~ -0.5), which subjected the dominantly andesitic volcanic rocks to extreme leaching and left behind a residue of silica around the fluid conduits. Only Ti, Zr and Nb were immobile in the residual silica rocks of the conduit. Alunite-pyrite alteration developed proximal to these conduits and kaolinite alteration distal to them as a result of the interaction of the fluid with the rock at progressively lower fluid/rock ratios, which buffered the pH of the fluid to progressively higher pH. Elements like Al, Fe, K, and P, which were leached in the immediate vicinity of the conduits, were re-deposited in the adjacent alunite-pyrite zone as a result of the increase in pH.

The magmatic vapors also transported Cu, Ag and Au, from the magma body at depth, either as hydrated sulfide or chloride species; Arsenic, which is known to have very high volatility, was probably transported in elemental state (Williams-Jones et al., 2002). Gold-, silver- and copper-bearing solids were undersaturated in the condensed vapors, but these metals were able to concentrate in the rocks (alunite-pyrite zone) through adsorption as negatively charged or neutral species onto the surfaces of growing pyrite crystals, which had acquired p-type semiconductive character due to incorporation of As. Once adsorbed, the metals were incorporated into the pyrite either as native metal nano-particles formed as a result of electrochemical reduction of the positive charge of the metals in the adsorbed species or into the pyrite structure via coupled substitutions with As for Fe in pyrite and, in the case of Cu, through direct exchange for Fe.

8. Conclusions

The results of this research provide direct evidence that the magmatic vapors, which are generally considered responsible for acid-sulfate alteration in high sulfidation epithermal Cu-Au-Ag ore deposits, can transport significant concentrations of ore metals. Although the gold and silver concentrations are well below the levels that would be deemed economic (gold concentrations in pyrite reached a maximum of 192 ppb and averaged 20 ppb and Ag concentrations reached 9.2 ppm and averaged 0.6 ppm), it should be noted that the mineralization was emplaced at very shallow depth. Indeed, there is every reason to believe that, if the mineralization had been emplaced at somewhat greater depth, the vapor would have been of significantly greater density and been able to transport significantly more metal (Williams-Jones et al., 2005). Under such conditions, it is reasonable to conclude that the resulting deposit would have had substantially higher concentrations of metals. Irrespective of whether there is gold-silver mineralization of economic grade at any depth below Kawah Ijen, the study provides incontrovertible evidence that magmatic vapors are capable not only of producing the acid-sulfate alteration accompanying high sulfidation precious metal deposits but also transporting the metals needed to form these deposits. Passively degassing volcanoes, such as Kawah Ijen, should therefore be viewed as the surface expressions of high-sulfidation epithermal systems and in turn of underlying porphyry copper ore-forming systems.

References

- Anovitz, L.M., Perkins, D., Essene, E.J., 1991. Metastability in near-surface rocks of minerals in the system $\text{Al}_2\text{O}_3\text{-SiO}_2\text{-H}_2\text{O}$. *Clays & Clay Minerals*. 39, 225-233.
- Archibald, S.M., Migdisov, A.A., Williams-Jones, A.E., 2001. The stability of Au-chloride complexes in water vapor at elevated temperatures and pressures. *Geochimica et Cosmochimica Acta*. 65, 4413-4423.
- Archibald, S.M., Migdisov, A.A., Williams-Jones, A.E., 2002. An experimental study of the stability of copper chloride complexes in water vapor at elevated temperatures and pressures. *Geochimica et Cosmochimica Acta*. 66, 1611-1619.
- Arribas, A., Jr., 1995. Characteristics of high sulfidation epithermal deposits, and their relation to magmatic fluids. Mineralogical Association of Canada Short Course Notes. 23, 419-454.
- Berger, B.R., Henley, R.W., 2011. Magmatic-vapor expansion and the formation of high-sulfidation gold deposits: Structural controls on hydrothermal alteration and ore mineralization. *Ore Geology Reviews*. 39, 75-90.
- Berlo, K. The Magmatic Evolution of the Ijen Caldera Complex. Drs thesis (unpublished), Utrecht 2001.
- Chouinard, A., Paquette, J., Williams-Jones, A.E., 2005a. Crystallographic controls on trace-element incorporation in auriferous pyrite from the Pascua epithermal high-sulfidation deposit, Chile-Argentina. *The Canadian Mineralogist*. 43, 951-963.
- Deditius, A.P., Utsunomiya, S., Renock, D., Ewing, R.C., Ramana, C.V., Becker, U., Kesler, S.E., 2008. A proposed new type of arsenian pyrite: Composition, nanostructure and geological significance. *Geochimica et Cosmochimica Acta*. 72, 2919-2933.
- Delmelle, P., Bernard, A., 1994. Geochemistry, mineralogy, and chemical modeling of the acid crater lake of Kawah Ijen Volcano, Indonesia. *Geochimica et Cosmochimica Acta*. 58, 2445-2460.
- Dill, H.G., 2003. A comparative study of APS minerals of the Pacific rim fold belts – with special reference to South American argillaceous deposits. *Journal for South American Earth Sciences*, 16, 301-320.

- Farquhar, J., Wing, B.A., 2003. Multiple sulfur isotopes and the evolution of the atmosphere. *Earth and Planetary Science Letters*. 213, 1-13.
- Gray, J.E., Coolbaugh, M.F., 1994. Geology and geochemistry of Summitville, Colorado; an epithermal acid sulfate deposit in a volcanic dome. *Economic Geology*. 89, 1906-1923.
- Griffin, W.L., Powell, W.J., Pearson, N.J., O'Reilly, S.Y., 2008. GLITTER: Data reduction software for laser ablation ICP-MS. *Laser Ablation-ICP-Mass Spectrometry in the Earth Sciences: Current Practices and Outstanding Issues* (Sylvester, P., Ed.), Mineralogical Association of Canada (MAC) Short Course Series. 40, 308-311.
- Guillong, M., Hametner, K., Reusser, E., Wilson, S.A., Günther, D., 2005. Preliminary characterization of new glass reference materials (GSA-1G, GSC-1G, GSD-1G and GSE-1G) by laser ablation-inductively coupled plasma-mass spectrometry using 193 nm, 213 nm and 266 nm wavelengths. *Geostandards and Geoanalytical Research*. 29, 315-331.
- Handley, H.K., Macpherson, C.G., Davidson, J.P., Berlo, K., Lowry, D., 2007. Constraining Fluid and Sediment Contributions to Subduction-Related Magmatism in Indonesia: Ijen Volcanic Complex. *Journal of Petrology*. 48, 1155-1183.
- Hedenquist, J.W., Lowenstern, J.B., 1994. The role of magmas in the formation of hydrothermal ore deposits. *Nature*. 370, 519-527.
- Hedenquist, J.W., Matsushita, Y., Izawa, E., White, N.C., Giggenbach, W.F., Oaki, M., 1994. Geology, geochemistry and origin of high-sulfidation Cu-Au mineralization in the Nanasatsu district, Japan. *Economic Geology*. 89, 1-30.
- Hedenquist, J.W., Arribas, A., Jr., Reynolds, T.J., 1998. Evolution of an Intrusion-Centered Hydrothermal System: Far Southeast-Lepanto Porphyry and Epithermal Cu-Au Deposits, Philippines. *Economic Geology*. 93, 373-404.
- Heinrich, C.A., Ryan, C.G., Mernagh, T.P., Eadington, P.J., 1992. Segregation of ore metals between magmatic brine and vapor; a fluid inclusion study using PIXE microanalysis. *Economic Geology*. 87, 1566-1583.

- Heinrich, C.A., Günther, D., Audétat, A., Ulrich, T., Frischknecht, R., 1999. Metal fractionation between magmatic brine and vapor, determined by microanalysis of fluid inclusions. *Geology*. 27, 755-758.
- Helgeson, H.C., Delany, J.M., Nesbitt, H.W., Bird, D.K., 1978. Summary and critique of the thermodynamic properties of rock-forming minerals. *American Journal of Science*. 278A, 220 pp.
- Hemingway, B.S., Haas, J.L., Robinson, G.R., 1982. Thermodynamic properties of selected minerals in the system $\text{Al}_2\text{O}_3\text{-CaO-SiO}_2\text{-H}_2\text{O}$ at 298.15 K and 1 bar (10^5 pascals) pressure and at higher temperatures. *U.S. Geological Survey Bulletin* 1544.
- Hengeveld, G.J.N., De mogelijkheid en de plaats van den bouw van een nieuwe sluis bij het kratermeer Kawah Idjen, in: Mededelingen en rapporten van het departement der burgelijke openbare werken; Geologische onderzoeken ten behoeve van 'slands waterstaat-, gewestelijke- en gemeentewerken in Nederlandsch-Indie, Weltevreden, 1920
- Henley, R.W., Berger, B.R., 2011. Magmatic-vapor expansion and the formation of high-sulfidation gold deposits: Chemical controls on alteration and mineralization. *Ore Geology Reviews*. 39, 63-74.
- Holland, T.J.B., Powell, R., 1998. An internally consistent thermodynamic data set for phases of petrological interest. *Journal of Metamorphic Geology*. 16, 309-343.
- Hudson, D.M., 2003. Epithermal Alteration and Mineralization in the Comstock District, Nevada. *Economic Geology*. 98, 367-385.
- Johnson, J.W., Oelkers, E.H., Helgeson, H.C., 1992. SUPCRT 92: A software package for calculating the standard molal thermodynamic properties of minerals, gases, aqueous species, and reactions from 1 to 5000 bars and 0° to 1000°C . *Computers and Geosciences*. 18, 899-947.
- Katili, J.A., 1975. Volcanism and plate tectonics in the Indonesian island arcs. *Tectonophysics*. 26, 165-188.
- Kemmerling, G.L.L., 1921b. Het Idjen Hoogland de geologie en geomorphologie van den Idjen. Batavia. Dr. H. Woudstra, Analyse van merkwaardige watersoorten op het Idjen-Hoogland.

- King, J.J., Williams-Jones, A.E., van Hinsberg, V.J., 2010. Finding Invisible Gold in Pyrite Using Crystallography. Québec Exploration, 164.
- Maclean, W.H., Kranidiotis, P., Immobile elements as monitors of mass transfer in hydrothermal alteration; Phelps Dodge massive sulfide deposit, Matagami, Quebec. *Economic Geology*. 82, 951-962.
- Krauskopf, K.B., 1957. The heavy metal content of magmatic vapor at 600 °C. *Economic Geology*. 52, 786-807.
- Krauskopf, K.B., 1964. The possible of volatile metal compounds in ore genesis. *Economic Geology*. 59, 22-45.
- Mavrogenes, J., Henley, R.W., Reyes, A., Berger, B., 2010. Sulfosalt melts: evidence of high-temperature vapor transport of metals in the formation of high-sulfidation lode gold deposits. *Economic Geology*. 105, 257-262.
- Mironov, A.G., Zhmodik, S.M., Maksimova, E.A., 1981. An experimental investigation of sorbtion of gold by pyrites with different thermoelectric properties. *Geochemistry International*. 18, 153-160.
- Möller, P., Kerten, G., 1994. Electrochemical accumulation of visible gold on pyrite and arsenopyrite surfaces. *Mineralium Deposita*. 29, 404-413.
- Ohmoto, H., Rye, R.O., 1979. Isotopes of sulfur and carbon. In: Barnes, H.L. (Ed.), *Geochemsitry of Hydrothermal Ore Deposits*, 2nd ed. Wiley, New York, pp. 509-567.
- Palmer, S., 2009. Hydrogeochemistry of the upper Banyu Pahit River valley, Kawah Ijen volcano, Indonesia. Unpublished M.Sc. Thesis, McGill University.
- Pankratz, L.B., 1982. Thermodynamic properties of elements and oxides. *Bulletin U.S. Bureau of Mines*, 672.
- Prokhorov, V.G., Lu, L.V., 1971. Electrochemical and thermoelectric properties of pyrite as a criterion of the conditions of mineral formation. In *Mineralogiya I mineralogicheskaya kristallografiya (Mineralogy and Mineral Crystallography)*, Sverdlovsk, 115.
- Robie, R.A., Hemingway, B.S., Fisher, J.R., 1978. Thermodynamic properties of minerals and related substances at 298.15 °K and 1 bar (10⁵ Pascals) pressure and higher temperatures. *Geological Survey Bulletin*, 1452.

- Robie, R.A., Hemingway, B.S., 1995. Thermodynamic properties of minerals and related substances at 298.15 K and 1 Bar (10^5 Pascals) pressure and at higher temperatures. U.S. Geological Survey Bulletin, 2131.
- Ruggieri, G., Lattanzi, P., Luxoro, S.S., Dessl, R., Benvenuti, M., Tanelli, G., 1997. Geology, Mineralogy, and Fluid Inclusion Data of the Furtei High-Sulfidation Gold Deposit, Sardinia, Italy. *Economic Geology*. 92, 1-19.
- Shock, E.L., Sassani, D.C., Willis, M., Sverjensky, D.A., 1997. Inorganic species in geological fluids: Correlations among standard molal thermodynamic properties of aqueous ions and hydroxide complexes. *Geochimica et Cosmochimica Acta*. 61, 907-950.
- Shvarov, Y.V., 2008. HCh: New Potentialities for the Thermodynamic Simulation of Geochemical Systems Offered by Windows. *Geochemistry International*. 46, 834-839.
- Simon, G., Huang, H., Penner-Han, J.E., Kesler, S.E., Kao, L., 1999. Oxidation state of gold and arsenic in gold-bearing arsenian pyrite. *American Mineralogist*. 84, 1071-1079.
- Sitorus, K., 1990. Volcanic stratigraphy and geochemistry of the Idjen Caldera Complex, East-Java, Indonesia. Unpublished MSc thesis, University of Wellington, New Zealand.
- Soeria-Atmadja, R., Maury, R.C., Bellon, H., Pringgoprawiro, H., Polve, M., Priadi, B., 1994. *Journal of Southeast Asian Earth Sciences*. 9, 13-27.
- Starling, A., Gilligan, J.M., Carter, A.H.C., Foster, R.P., Saunders, R.A., 1989. High-temperature hydrothermal precipitation of precious metals on the surface of pyrite. *Nature*. 340, 298-300.
- Steven, T.A., Ratté, J.C., 1960. Geology and ore deposits of the Summitville district, San Juan Mountains Colorado. U.S. Geological Survey Professional Paper 343, 70 p.
- Stoffregen, R., 1987. Genesis of Acid-Sulfate Alteration and Au-Cu-Ag Mineralization at Summitville, Colorado. *Economic Geology*. 82, 1575-1591.
- Stoffregen, R., Cygan, G., 1990. An experimental study of Na-K exchange between alunite and aqueous sulfate solutions. *American Mineralogist*. 75, 209-220.

- Stoffregen, R.E., Alpers, C.N., Jambor, J.L., 2000. Alunite-Jarosite Crystallography, Thermodynamics, and Geochronology. *Reviews in Mineralogy and Geochemistry*. 40, 453-479.
- Symonds, R.B., Rose, W.I., Gerlach, T.M., Briggs, P.H., Harmon, R.S., 1990. Evaluation of gases, condensates, and SO₂ emissions from Augustine volcano, Alaska: the degassing of a Cl-rich volcanic system. *Bulletin of Volcanology*. 52, 355-374.
- Symonds, R.B., Mizutani, Y., Briggs, P.H., 1996. Long-term geochemical surveillance of fumaroles at Showa-Shinane dome, Usu volcano, Japan. *Journal of Volcanology and Geothermal Research*. 73, 177-211.
- Taran, Y.A., Bernard, A., Gavilanes, J.-C., Luneheva, E., Cortes, A., Armienta, M.A., 2001. Chemistry and mineralogy of high-temperature gas discharges from Colima volcano, Mexico. Implications for magmatic gas-atmosphere interaction. *Journal of Volcanology and Geothermal Research*. 108, 245-264.
- Takano, B., Suzuki, K., Sugimori, K., Ohba, T., Fazlullin, S.M., Bernard, A., Sumarti, S., Sukhyar, R., Hirabayashi, M., 2004. Bathymetric and geochemical investigation of Kawah Ijen crater lake, east Java, Indonesia. *Journal of Volcanology and Geothermal Research*. 135, 299-329.
- van Bemmelen, R.W. The geology of Indonesia, 2nd Ed., Den Haag, 1949.
- van Hinsberg, V. J., 2001. Water-rock Interaction and Element Fluxes in the Kawah Ijen Hyperacid Crater Lake and the Banyu Pait River, East Java, Indonesia. Unpublished M.Sc. Thesis, Universiteit Utrecht.
- van Hinsberg, V., Berlo, K., van Bergen, M., Williams-Jones, A., 2010a. Extreme alteration by hyperacidic brines at Kawah Ijen volcano, East Java, Indonesia: I. Textural and mineralogical imprint. *Journal of Volcanology and Geothermal Research*. 198, 253-263.
- van Hinsberg, V., Berlo, K., Sumarti, S., van Bergen, M., Williams-Jones, A., 2010b. Extreme alteration by hyperacidic brines at Kawah Ijen volcano, East Java, Indonesia: II: Metasomatic imprint and element fluxes. *Journal of Volcanology and Geothermal Research*. 196, 169-184.

- van Hinsberg, V.J., Vigouroux, N., Palmer, S.J., Berlo, K., Scher, S., Mauri, G., McKenzie, J., Williams-Jones, G., Williams-Jones, A.E., unpublished. Volcanogenic pollution: assessing the total element flux to the environment of Kawah Ijen volcano, Indonesia.
- Vigouroux, N., G. Williams-Jones, A.E. Williams-Jones, V.J. van Hinsberg. Tracking volatile ratios through the magmatic and hydrothermal system of Kawah Ijen Volcano, Indonesia. 2009 Portland GSA Annual Meeting, 18-19 October. Paper No. 155-11.
- Vigouroux-Caillibot, N., Williams-Jones, G., Berlo, K., van Hinsberg, V., Palmer, S., Scher, S., Williams-Jones, W., Wallace, P.J. Integrated geochemical modeling of magmatic degassing and hydrothermal interaction: a case study from Kawah Ijen volcano, Indonesia. American Geophysical Union, Fall Meeting 2010, abstract #V53B-2250.
- Voudouris, P.G.; 2010. Conditions of formation of the Mavrokoryfi high-sulfidation epithermal Cu-Ag-Au-Te mineralization (Petrota Graben, NE Greece). *Mineralogy and Petrology*. 101, 97-113.
- Williams-Jones, A.E., Migdisov, A.A., Archibald, S.M., Xiao, Z., 2002. Vapor-transport of ore metals. *Geochemical Society Special Publication* 7, p. 279-305.
- Williams-Jones, A.E., Heinrich, C.A., 2005. Vapor Transport of Metals and the Formation of Magmatic-Hydrothermal Ore Deposits. *Economic Geology* 100th Anniversary, 1287-1312.
- Williams-Jones, A.E., Bowell, R.J., Migdisov, A.A., 2009. Gold in Solution. *Elements*. 5, 281-287.
- Wilson, S.A., Ridley, W.I., Koenig, A.E., 2002. Development of sulfide calibration standards for the laser ablation inductively-coupled plasma mass spectrometry technique. *Journal of Analytical Atomic Spectrometry*. 17, 406-409.
- Zezin, D., Migdisov, A.A., Williams-Jones, A.E., 2007. The solubility of gold in hydrogen sulfide gas: An experimental study. *Geochimica et Cosmochimica Acta*. 71, 3070-3081.

Zezin, D., Migdisov, A.A., Williams-Jones, A.E., 2011a. The solubility of gold in H₂O-H₂S vapour at elevated temperature and pressure. *Geochimica et cosmochimica Acta*. In press.

Chapter 4: Conclusions and Contributions to Knowledge

1. Main Findings

1. At Kawah Ijen, the protoliths to alteration are either andesite or dacite rocks. The vapors responsible for the alteration are analogous to those sampled on the active dome; the dome is within the limits of the alteration center, thus the gases sampled reflect the composition of the hydrothermal fluid at depth and are responsible for the alteration. The cristobalite-altered zones were created in a fluid-buffered environment and that as the distance from the fluid source increased, the fluids became less acidic as evidenced by the presence of the alunite- and kaolinite-altered zones. This decrease in acidity is due to rock-buffering of the fluid. Furthermore, elements were extremely mobile during alteration. In opposition to the literature, which supports that once leached from the precursor rocks elements completely exit the system, there was element mass gains in the alunite- and kaolinite-alteration zones.
2. Highly acidic and oxidized vapors exsolve from a magma body at depth. These vapors transport significant quantities of trace metals and are responsible for the concurrent alteration and mineralization at Kawah Ijen volcano.
3. At Kawah Ijen, Au, Ag, Cu, and other trace metals are located solely in pyrite. The metals are transported in the vapor phase by condensed volcanic gases. Upon reaching the alunite-alteration zone, the metal-rich vapors condense and the metals are adsorbed onto the growing pyrite surface. The metals are incorporated as nano-particles or are substituted into the pyrite structure via coupled substitutions.
4. Acidic fumarolic systems of passively degassing volcanoes, such as Kawah Ijen, can be viewed as the surface expression of high-sulfidation epithermal systems and possibly of deeper porphyry copper systems during their early stages of development.

2. Contributions to Knowledge

The most significant findings in this thesis are that volcanic vapors are capable of transporting significant quantities of metals, including Au, Ag and Cu, and that the processes of alteration and mineralization are concurrent. Previous models for these systems have generally ignored vapor transport of metals simultaneous with alteration, in favor of post-alteration liquid transporting and depositing metals. Also important is the finding that there is element mass gains in the different alteration zones, in opposition to ubiquitous mass loss of elements in all alteration zones during alteration formation. Finally, the association with metals in pyrite is an emerging field of study. Research on high-sulfidation epithermal deposits, e.g. Pascua (Chile-Argentina; Chouinard et al., 2005a), Yanacocha (Peru; Deditius et al., 2008) and Binebase and Bowone (Sangihe Island, Indonesia; King et al., 2010), demonstrate that Au, As and Cu are bound in the structure of the pyrite. While further research into the pyrite at Kawah Ijen is necessary, at this point the conclusion that metals are adsorbed on the growing pyrite surface is an important idea that merits further examination in high-sulfidation epithermal deposits. Finally, the link that has been established between high-sulfidation epithermal systems and the volcanic-hydrothermal environment also contributes to the evolution of our understanding of the dynamics of subduction zone environments.

References

- Chouinard, A., Paquette, J., Williams-Jones, A.E., 2005a. Crystallographic controls on trace-element incorporation in auriferous pyrite from the Pascua epithermal high-sulfidation deposit, Chile-Argentina. *The Canadian Mineralogist*. 43, 951-963.
- Deditius, A.P., Utsunomiya, S., Renock, D., Ewing, R.C., Ramana, C.V., Becker, U., Kesler, S.E., 2008. A proposed new type of arsenian pyrite: Composition, nanostructure and geological significance. *Geochimica et Cosmochimica Acta*. 72, 2919-2933.
- King, J.J., Williams-Jones, A.E., van Hinsberg, V.J., 2010. Finding Invisible Gold in Pyrite Using Crystallography. *Québec Exploration*, 164.

Appendix I: Sample locations and mineral proportions (wt%) based on Rietveld analyses of X-ray diffractograms.

Sample	Kaolinite	Alunite	Cristobalite	Easting	Northing	Elevation (m.a.s.l.)
KS09-1A	40.4	2.0	57.6	196254	9108063	2166
KS09-1B	42.4	26.6	31.0	196252	9108058	2166
KS09-1F	31.7	6.2	62.1	196243	9108036	2154
KS09-2A	9.6	0.6	89.8	196259	9108056	2171
KS09-2B	39.4	29.7	30.9	196257	9108051	2170
KS09-2E	22.6	0.0	77.4	196251	9108038	2159
KS09-3A	2.1	17.6	80.3	196252	9108025	2149
KS09-3D	0.8	0.3	98.9	196259	9108038	2163
KS09-3E	23.0	16.1	60.9	196261	9108042	2168
KS09-3F	37.5	13.2	49.4	196263	9108047	2171
KS09-3G	34.8	64.3	0.9	196266	9108051	2173
KS09-4A	29.3	0.7	70.0	196260	9108029	2153
KS09-4H	18.5	29.6	51.6	196252	9108003	2149
KS09-4I	7.7	73.5	18.9	196257	9108004	2151
KS09-5D	13.7	28.1	58.2	196261	9108011	2153
KS09-5Ea	1.3	38.1	60.6	196288	9108028	2174
KS09-6D	31.2	49.5	19.3	196267	9108004	2156
KS09-6U	1.4	88.4	10.3	196276	9108021	2160
KS09-6X	19.2	13.3	67.6	196283	9108035	2171
KS09-7AV	32.3	61.8	5.9	196281	9108009	2165
KS09-7B	34.4	3.5	62.1	196283	9108013	2168
KS09-7F	25.9	73.5	0.6	196292	9108031	2182
KS09-7Tb	20.5	75.9	3.7	196283	9108013	2168
KS09-7U	47.8	27.9	24.4	196285	9108018	2170
KS09-7V	17.4	75.2	7.5	196288	9108022	2173
KS09-7X	6.0	15.0	79.0	196292	9108031	2182
KS09-7Y	68.4	9.1	22.6	196294	9108036	2187
KS09-7Z	1.9	24.3	73.8	196296	9108040	2186
KS09-8A	61.4	8.1	30.5	196285	9108003	2170
KS09-8C	22.6	10.0	67.4	196283	9108000	2169
KS09-8G	51.2	1.9	46.8	196272	9107976	2155
KS09-8H	29.8	2.7	67.5	196270	9107972	2156
KS09-8U	0.0	0.1	99.9	196285	9108003	2169
KS09-8W	26.3	31.2	42.5	196276	9107985	2155
KS09-9A	55.5	18.1	26.4	196290	9107995	2170
KS09-9C	35.4	11.7	52.9	196286	9107986	2161
KS09-9D	52.9	1.9	45.3	196283	9107982	2156
KS09-9H	51.1	32.9	16.0	196273	9107959	2159
KS09-9R	25.7	17.5	56.8	196294	9107999	2175
KS09-9Y	59.6	2.3	38.2	196310	9107999	2184
KS09-9Z	24.8	4.6	70.6	196312	9108044	2193
KS09-10A	23.4	76.0	0.6	196292	9107992	2170
KS09-10B	17.1	74.0	8.9	196290	9107988	2165
KS09-10U2	11.6	2.3	86.2	196294	9107996	2173
KS09-10V	42.5	0.9	56.6	196296	9108001	2177
KS09-10Z	29.6	11.9	58.5	196263	9107986	2154
KS09-11A	49.9	49.2	1.0	196297	9107985	2166
KS09-11B	18.4	60.1	21.6	196295	9107983	2164
KS09-11C	20.5	72.3	7.2	196293	9107981	2162
KS09-11D	29.0	65.2	5.9	196291	9107978	2160
KS09-11W	47.7	1.3	51.0	196302	9107994	2174
KS09-12A	6.6	62.1	31.3	196303	9107978	2167
KS09-12B	41.0	54.2	4.8	196308	9107973	2169
KS09-12U	29.5	67.2	3.3	196305	9107982	2169
KS09-12Y	42.9	52.7	4.3	196278	9107973	2155
KS09-13AR	32.5	60.7	6.8	196309	9107965	2167
KS09-13F	26.6	31.5	42.0	196284	9107960	2159
KS09-13V	23.0	39.0	38.0	196316	9107978	2174
KS09-13Z	24.2	40.2	35.6	196324	9107996	2189
KS09-14A	24.6	43.7	31.7	196314	9107958	2168
KS09-14D	92.0	0.3	7.7	196308	9107944	2165
KS09-14U	0.3	99.7	0.0	196317	9107962	2169
KS09-14X	0.0	55.1	44.9	196323	9107976	2176
KS09-14Z	9.6	65.1	25.3	196328	9107985	2184
KS09-15E	44.8	0.5	54.7	196311	9107958	2166
KS09-15V	0.0	78.8	21.2	196324	9107985	2182
KS09-15Z	7.6	68.4	24.0	196333	9108003	2197
KS09-16E	5.3	0.1	94.6	196317	9107926	2177
KS10-KISS-1	29.0	0.4	70.6	196313	9107913	2078
KS10-KISS-2	1.3	0.5	98.2	196274	9107962	2083
KS10-KISS-3	53.2	0.6	46.2	196326	9107921	2084
KS10-KISS-4	23.4	44.9	31.7	196328	9107920	2087
KS10-KISS-5	61.8	0.4	37.8	196341	9107922	2084
KS10-KISS-6	14.2	9.3	76.5	196339	9107926	2084
KS10-KISS-7	49.3	49.2	1.5	196331	9107931	2083
KS10-KISS-8	26.6	7.3	66.2	196339	9107926	2084
KS10-KISS-9	28.8	64.4	6.8	196300	9107862	2105
KS10-KISS-10	78.5	8.9	12.6	196305	9107867	2101
KS10-KISS-11	39.7	1.5	58.8	196282	9107888	2076
KS10-KISS-12	53.8	1.3	44.9	196278	9107883	2076
KS10-KISS-13	18.7	66.2	15.0	196246	9107913	2069
KS10-KISS-14	22.2	45.1	32.7	196241	9107931	2064
KS10-KISS-15	1.0	7.2	91.7	196244	9107958	2066
KS10-KISS-16	0.1	33.2	66.7	196284	9108136	2069
KS10-KISS-18	75.3	1.5	23.3	196252	9108091	2061
KS10-KISS-19	20.9	26.1	53.0	196256	9108087	2066
KS10-KISS-20	14.3	37.8	47.9	196257	9108087	2066
KS10-KISS-21	54.2	0.0	45.8	196258	9108087	2066
KS10-KISS-22	21.7	77.7	0.6	196248	9108090	2064

Sample	Kaolinite	Alunite	Cristobalite	Easting	Northing	Elevation (m.a.s.l.)
KS10-KISS-23	46.0	52.3	1.7	196236	9108057	2071
KS10-VA1	58.1	29.5	12.4	196423	9107315	2108
KS10-VA2	15.0	73.8	11.2	196422	9107318	2106
KS10-VA3	6.2	93.2	0.6	196420	9107922	2101
KS10-VA4	52.6	46.5	0.9	196417	9107922	2101
KS10-VA5	15.6	55.3	29.1	196413	9107923	2101
KS10-VA6	44.2	1.3	54.5	196410	9107923	2100
KS10-VA7	96.0	1.2	2.9	196409	9107923	2099
KS10-VA8	12.3	86.6	1.0	196408	9107923	2099
KS10-VA9	33.9	63.7	2.4	196407	9107923	2099
KS10-VA10_A	97.0	0.0	3.1	196408	9107919	2099
KS10-VA10_B	54.7	0.0	45.3	196407	9107918	2099
KS10-VA10_C	63.4	2.6	34.1	196407	9107919	2099
KS10-VA11	48.8	26.8	24.4	196383	9107938	2096
KS10-VA12_A	62.7	0.1	37.2	196391	9107927	2098
KS10-VA12_B	0.1	63.4	36.6	196391	9107927	2098
KS10-VA13	68.3	0.0	31.7	196380	9107947	2100
KS10-VA14	43.7	42.5	13.8	196359	9107998	2087
KS10-VA15	62.7	9.5	27.8	196343	9108002	2086
KS10-VA16	12.0	0.1	87.9	196334	9108024	2083
KS10-VA17	28.0	64.3	7.7	196316	9108030	2082
KS10-VA18	93.4	6.6	0.0	196329	9108043	2081
KS10-VA19	33.7	13.3	50.0	196321	9108048	2075
KS10-VA20	66.7	0.1	33.2	196315	9108069	2075
KS10-VA21	13.4	2.1	84.5	196315	9108069	2075
KS10-VA22	22.5	1.4	76.1	196331	9108099	2067
KS10-VA23	29.9	39.9	30.2	196318	9108115	2070
KS10-VB1	37.0	9.2	53.8	196425	9107953	2103
KS10-VB2	12.2	25.0	62.9	196414	9107969	2099
KS10-VB3	65.0	14.1	20.9	196392	9108010	2093
KS10-VB4	48.3	20.7	31.1	196385	9108065	2076
KS10-VB5	3.1	0.0	96.9	196382	9108065	2078
KS10-VB5-2	13.5	0.1	86.4	196382	9108065	2078
KS10-VB6	43.7	0.3	56.1	196355	9108093	2073
KS10-VB7	27.1	0.0	72.9	196354	9108085	2075
KS10-VB8	44.3	38.7	17.1	196346	9108123	2068
KS10-VB9	3.8	0.6	95.6	196345	9108122	2068
KS10-VB10	23.0	1.1	75.9	196332	9108106	2069
KS10-VC1	59.1	1.9	39.0	196323	9108142	2061
KS10-VC2	71.1	8.2	20.8	196359	9108139	2054
KS10-VC3	14.0	11.4	74.7	196359	9108139	2054
KS10-VC4	55.9	2.8	41.3	196385	9108173	2057
KS10-VC5	41.0	0.5	58.5	196383	9108170	2056
KS10-VC6	68.6	9.3	22.1	196458	9108049	2103
KS10-VC7	21.3	77.0	1.8	196438	9108052	2098
KS10-VC8	32.2	3.9	63.8	196394	9108074	2084
KS10-VC9	31.9	6.6	61.5	196402	9108084	2081
KS10-VC10	26.8	69.5	3.6	196402	9108119	2075
KS10-VC11	19.8	2.0	78.2	196414	9108131	2067
KS10-E1	64.9	33.1	2.0	195985	9107509	2173
KS10-E2	27.7	0.0	72.3	196008	9107530	2176
KS10-E3	0.1	0.8	99.1	196008	9107530	2176
KS10-E4	41.5	4.3	54.1	196034	9107516	2178
KS10-E5	78.6	18.1	3.3	1966109	9107546	2186
KS10-SFM1	23.1	63.8	13.2	1966204	9107975	2049
KS10-SFM2	39.4	15.9	44.7	1966204	9107975	2049

Appendix II: Trace element compositions (ppm) of pyrite grains from the alteration center at Kawah Ijen. Analyses performed using LA-ICPMS.

	Co	Ni	Cu	Zn	As	Se	Mo	Ag	Cd	Sn	Sb	Te	Au	Hg	Tl	Pb	Bi
KS10-VB-5B	20.51	10.71	8.05	0.57	3.19	74.68	0.05	0.03	0.05	0.23	0.02	<0.00	<0.0075	0.25	0.03	0.20	0.00
	50.14	9.13	280.29	116.19	108.04	46.10	2.60	0.78	3.79	2.09	3.86	<0.00	0.01	0.18	3.95	103.01	0.42
	54.30	8.32	302.27	127.86	149.45	86.26	2.48	1.08	3.91	2.19	4.70	<0.00	<0.0055	0.25	3.75	120.29	0.21
	15.61	2.58	16.24	190.61	12.27	94.46	2.50	0.75	0.70	3.51	1.52	<0.00	<0.0187	0.48	0.12	2.47	0.07
	151.24	25.03	17.96	12.38	10.07	94.54	0.09	0.39	0.08	0.05	0.03	<0.00	<0.0087	<0.152	0.12	5.07	0.01
	8.45	8.85	41.05	2.89	7.77	64.83	1.60	0.45	0.04	2.50	0.33	<0.00	<0.0065	<0.11	0.09	1.13	0.11
	10.04	4.27	60.07	328.08	22.89	70.22	1.55	0.42	2.34	7.24	2.09	<0.00	<0.018	0.64	0.67	7.76	0.15
	19.02	3.16	30.02	27.27	5.52	55.10	0.47	0.12	0.21	0.93	0.53	<0.00	0.02	<0.51	0.40	13.91	0.05
	48.05	25.34	21.81	6.19	4.81	76.21	0.59	0.11	0.13	3.55	0.52	<0.00	<0.0101	0.43	0.09	1.75	0.04
	76.23	325.88	60.68	153.60	48.33	70.02	7.77	0.65	1.52	45.53	7.71	<0.00	0.02	0.43	0.44	7.70	0.44
	91.03	25.03	206.67	172.85	359.13	86.46	6.66	1.57	1.97	10.95	5.20	<0.00	0.02	0.40	1.86	83.31	0.77
	54.20	15.40	167.03	113.66	68.23	137.03	7.64	1.85	0.99	15.22	5.92	<0.00	0.02	<0.25	1.60	47.88	0.66
	128.78	42.53	229.67	168.17	97.39	124.12	16.58	2.72	1.85	5.69	5.40	<0.00	<0.0148	0.38	2.87	104.59	1.08
	39.77	21.99	47.73	28.17	1001.29	68.57	3.90	0.58	0.23	14.03	3.82	<0.00	<0.0188	0.37	0.34	5.17	0.19
	56.95	55.91	15.97	24.50	15.51	110.34	1.75	0.29	<0.031	12.98	3.61	<0.00	<0.0159	<0.23	0.15	1.29	0.13
	65.52	7.12	117.30	34.21	47.58	130.99	7.86	1.94	1.34	42.96	9.73	<0.00	<0.019	<0.44	0.64	12.25	0.59
	23.33	129.69	391.26	58.33	26.81	206.50	11.65	1.31	0.22	26.67	6.45	<0.00	<0.0117	0.79	0.34	1.90	0.29
	29.53	27.64	19.04	0.59	2.86	59.43	0.23	0.03	0.07	0.38	0.13	<0.00	<0.0140	0.38	0.05	0.66	0.07
	18.29	7.81	167.40	34.37	924.22	89.94	2.45	0.46	0.12	16.53	3.83	<0.00	0.02	0.61	0.10	4.83	0.26
	14.45	5.67	89.60	24.57	14.62	55.17	1.66	0.22	0.22	13.19	3.93	<0.00	<0.011	0.32	0.11	1.69	0.11
	53.89	17.45	45.02	63.55	78.96	91.26	12.08	0.58	0.18	96.49	23.34	<0.00	0.02	0.95	0.43	3.76	0.65
	9.87	7.51	88.74	0.69	6.26	35.63	0.15	0.01	0.22	0.06	<0.010	<0.00	<0.0125	0.85	0.35	4.27	0.08
	18.66	37.63	28.88	2.90	7.11	52.31	0.22	0.04	<0.059	1.42	0.31	<0.00	<0.0152	1.21	0.12	1.15	0.11
	76.92	27.23	155.41	26.63	106.83	124.06	3.86	0.20	1.67	26.42	8.65	<0.00	0.02	4.00	3.50	53.95	3.13
	103.39	30.64	386.98	157.92	170.23	91.59	5.91	0.37	3.93	4.90	8.89	<0.00	0.02	2.15	8.82	225.62	11.95
	149.92	40.45	107.93	7.59	27.18	92.53	0.76	0.06	<0.053	3.66	1.11	<0.00	<0.018	2.07	1.06	20.99	0.17
	3.29	2.38	76.21	1.30	4.43	10.05	0.15	0.01	<0.052	<0.042	<0.0118	<0.00	<0.0091	<0.84	0.24	3.19	0.14
	148.23	19.58	31.96	0.92	5.15	99.82	0.08	0.02	<0.053	<0.049	0.02	<0.00	<0.0197	1.70	0.14	3.57	0.10
	211.73	35.66	38.83	7.97	34.90	128.32	1.49	0.12	0.21	20.94	3.22	<0.00	<0.0137	0.99	0.47	19.94	0.26
	193.81	32.10	42.18	2.05	29.75	126.73	0.35	0.22	0.09	0.31	0.29	<0.00	<0.020	<1.09	0.53	27.59	0.05
	143.26	17.94	219.01	11.24	46.37	91.62	4.35	0.38	0.64	36.37	11.77	<0.00	<0.032	<1.69	1.39	25.56	1.15
	158.04	20.12	83.32	1.97	16.66	91.85	0.14	0.14	0.46	<0.066	0.09	<0.00	<0.0217	2.64	0.49	12.32	0.16
	64.47	53.00	266.69	118.49	121.52	74.60	6.92	0.39	2.84	7.11	6.67	<0.00	<0.0114	1.72	6.26	142.93	7.51
	57.91	15.84	393.63	53.51	28.43	56.69	2.92	0.19	1.25	21.72	6.24	<0.00	<0.0204	1.99	0.49	9.03	0.45
	45.88	16.29	590.66	1.81	19.70	41.08	1.09	0.04	0.08	8.94	1.91	<0.00	0.02	<1.55	0.49	11.06	0.14
	130.62	20.42	600.32	27.25	103.07	39.80	9.92	0.35	1.97	93.72	25.40	<0.00	<0.028	<1.67	2.23	42.19	2.17
	169.24	27.81	121.57	5.54	17.60	88.01	0.84	0.05	0.19	8.68	2.57	<0.00	<0.033	<1.39	0.64	13.16	0.37
	126.30	24.68	178.71	23.96	96.94	107.06	6.81	0.22	1.30	62.62	14.33	<0.00	0.03	2.50	2.01	52.17	2.10
	86.83	25.91	22.98	0.89	6.59	112.69	0.12	0.02	<0.063	0.21	0.10	<0.00	0.02	1.67	0.15	2.27	0.02
KS10-VA-3	24.62	21.59	44.02	9.80	6.53	0.66	0.33	0.06	0.36	0.69	0.03	<0.00	<0.0056	3.73	1.08	4.47	0.01
	168.83	79.59	3247.25	1041.23	124.62	1.65	14.08	0.09	0.86	9.13	0.60	<0.00	<0.0077	3.10	184.30	27.42	0.08
	263.33	117.19	3450.46	616.74	154.34	1.23	45.63	0.06	4.63	3.43	0.20	<0.00	<0.0078	3.64	88.98	28.85	0.14
	182.48	93.63	3785.10	522.52	400.72	3.09	33.05	0.03	25.90	4.96	0.29	<0.00	<0.0155	4.20	211.46	15.83	0.14

	Co	Ni	Cu	Zn	As	Se	Mo	Ag	Cd	Sn	Sb	Te	Au	Hg	Tl	Pb	Bi
	187.09	46.67	4884.78	1164.48	380.61	1.84	38.19	0.07	1.75	4.28	0.15	<0.00	<0.017	1.32	149.48	23.72	0.09
	147.00	106.53	4755.29	888.36	738.44	3.90	41.00	0.09	5.94	6.81	0.25	<0.00	0.02	3.51	167.48	40.61	0.15
	123.92	73.73	3547.21	690.80	397.62	2.21	24.68	0.02	18.39	4.05	0.18	<0.00	<0.0177	3.11	261.41	16.13	0.37
	85.53	89.01	6776.17	480.01	153.44	3.80	16.97	0.19	4.32	85.11	0.49	<0.00	<0.026	2.03	173.17	84.85	0.18
	137.80	73.81	4044.63	515.74	183.85	3.41	37.13	0.16	1.96	2.28	0.32	<0.00	<0.026	3.92	89.32	20.21	0.14
	180.53	88.99	3186.09	1032.89	450.06	3.43	37.40	0.10	1.20	2.96	0.39	<0.00	<0.037	3.93	112.87	43.51	0.16
	95.99	80.42	3056.89	799.69	430.81	2.39	19.06	0.02	0.66	5.39	0.22	<0.00	<0.016	0.80	117.29	18.95	0.12
	33.76	10.08	29.57	10.91	4.58	1.57	1.67	0.24	0.09	0.25	0.08	<0.00	<0.0059	3.29	3.96	6.85	0.18
	29.65	18.01	23.78	15.79	218.92	1.13	7.98	0.04	0.14	0.24	1.05	<0.00	<0.0072	0.42	8.63	30.68	0.18
	5.28	4.19	74.07	50.54	116.72	4.40	4.29	0.23	0.25	0.54	0.38	<0.00	0.03	0.88	7.57	37.20	0.63
	296.70	203.07	2858.34	1079.26	522.80	4.41	40.57	0.05	7.79	3.71	0.28	<0.00	<0.0108	0.46	62.55	18.83	0.30
KS09-P3	n.a.	20.94	501.20	304.47	402.34	98.65	15.63	0.52	2.02	4.02	15.49	22.10	0.00	0.77	113.64	59.06	53.21
	n.a.	5.14	15.18	0.53	0.00	47.25	0.29	0.01	0.00	0.03	0.05	0.57	0.00	0.40	0.07	0.84	1.35
	n.a.	20.28	21.92	1.27	3.59	96.72	0.52	0.02	0.35	0.34	0.14	0.61	0.00	0.41	0.21	0.67	1.54
	n.a.	15.42	1240.46	28.33	249.53	55.28	39.42	0.69	0.29	0.84	4.43	58.14	0.00	0.91	3.93	36.09	14.32
	n.a.	7.62	1301.65	1.59	8.90	105.67	6.74	0.02	0.12	0.46	0.05	1.78	0.01	0.27	0.20	2.57	6.83
	n.a.	21.19	633.57	9.12	177.78	152.02	38.96	0.32	0.29	2.25	3.84	26.47	0.02	1.88	4.24	35.67	17.27
	n.a.	3.23	86.27	3.04	61.75	40.82	3.25	0.06	0.20	0.52	0.48	5.12	0.00	0.52	1.26	7.11	23.20
	n.a.	1.51	82.15	9.50	66.58	12.77	11.27	0.07	1.35	35.88	0.70	11.97	0.00	0.38	14.57	322.68	43.60
	n.a.	44.81	393.35	7.97	176.11	78.07	22.14	0.24	0.22	3.03	3.50	28.97	0.00	4.43	3.97	20.41	28.88
	n.a.	19.20	467.49	0.97	15.75	0.00	14.98	0.10	0.16	0.18	0.35	0.38	0.00	0.07	1.11	0.25	10.71
	n.a.	6.12	344.18	4.93	122.44	43.68	19.73	0.37	0.08	1.15	2.02	19.46	0.00	0.25	8.52	9.21	13.14
	n.a.	4.26	274.28	1.90	43.19	7.59	5.81	0.02	0.06	0.25	0.40	4.10	0.01	0.00	0.51	2.20	3.82
	n.a.	16.26	396.30	7.19	155.57	48.50	25.68	0.27	0.57	3.87	3.74	26.88	0.00	0.94	3.53	9.92	14.95
	n.a.	26.75	842.18	18.22	232.36	121.20	59.55	0.48	1.03	4.29	6.30	35.93	0.00	0.51	22.85	166.88	30.61
	n.a.	59.84	830.55	18.10	278.95	70.98	58.12	0.46	0.89	3.70	7.57	42.66	0.01	1.39	13.13	38.71	38.86
	n.a.	16.52	488.22	20.83	208.18	60.46	60.32	0.35	1.99	4.72	5.47	32.48	0.01	0.65	9.00	59.71	43.80
	n.a.	65.79	1272.22	12.53	278.64	47.24	61.77	0.67	0.74	5.21	7.02	39.08	0.04	0.93	8.59	23.41	34.54
KS09-VA-9	n.a.	5.32	17.70	0.78	4.85	19.21	0.26	0.01	0.03	0.09	0.02	3.67	0.00	0.74	0.15	0.22	1.13
	n.a.	6.03	60.20	3.25	67.13	96.08	5.41	0.04	0.56	1.41	0.24	2.87	0.00	0.59	7.34	31.50	10.55
	n.a.	2.99	103.41	4.61	310.25	52.16	4.90	0.06	0.67	5.86	0.52	16.70	0.00	0.63	83.12	46.47	19.79
	n.a.	6.11	102.78	0.65	2.17	77.99	0.00	0.00	0.03	0.03	0.00	0.55	0.00	0.35	0.01	0.08	0.44
	n.a.	337.77	1883.09	14.02	1327.59	23.41	261.72	0.00	9.69	60.96	51.12	33.95	0.02	0.99	130.67	0.00	0.00
	n.a.	11.95	72.26	1.18	170.33	129.26	0.38	0.10	0.05	0.13	0.65	0.48	0.00	0.57	2.83	6.93	12.13
	n.a.	5.29	1.70	0.75	4.07	100.41	0.12	0.01	0.02	0.05	0.07	1.13	0.00	0.64	0.18	0.93	0.80
	n.a.	4.91	61.34	1.64	18.21	86.49	0.54	0.01	0.06	0.32	0.14	1.62	0.00	0.90	0.80	3.69	3.53
	n.a.	2.41	744.13	1.91	87.50	33.07	5.82	0.14	1.19	7.71	0.43	21.85	0.00	0.56	3.05	192.09	25.53
	n.a.	0.11	1.64	0.54	0.00	2.71	0.00	0.00	0.00	0.00	0.00	1.86	0.00	0.00	0.00	0.16	1.77
	n.a.	8.95	0.51	0.79	1.56	84.56	0.01	0.00	0.00	0.00	0.00	0.06	0.00	0.09	0.07	0.03	0.25
	n.a.	25.63	0.30	0.64	1.96	93.43	0.00	0.00	0.00	0.00	0.00	0.00	0.00	0.76	0.00	0.08	0.01
	n.a.	7.13	50.20	1.37	14.68	40.55	3.85	0.02	0.20	0.61	0.07	1.20	0.00	0.24	1.11	6.94	5.15
	n.a.	6.36	698.88	3.89	189.99	35.00	18.89	0.49	0.77	4.65	0.90	13.03	0.00	0.81	36.82	66.92	75.98
	n.a.	4.73	1.43	0.54	0.69	51.54	0.01	0.00	0.00	0.00	0.01	0.00	0.00	0.00	0.03	0.19	0.07
	n.a.	2.26	139.20	3.03	46.58	31.36	0.61	0.20	6.23	5.92	0.19	4.41	0.00	0.40	1.20	76.59	79.31

	Co	Ni	Cu	Zn	As	Se	Mo	Ag	Cd	Sn	Sb	Te	Au	Hg	Tl	Pb	Bi
KV08-2	n.a.	0.62	2155.75	1.57	35.26	15.86	25.07	0.26	0.00	0.04	2.77	4.04	0.01	0.78	9.43	1.29	3.61
	n.a.	0.23	1650.42	0.70	31.13	12.58	19.53	0.37	0.00	0.05	3.35	0.67	0.01	2.82	8.00	1.66	7.58
	n.a.	0.65	554.70	0.90	15.68	39.13	11.59	0.09	0.00	0.10	1.28	2.51	0.01	0.60	3.77	1.20	4.33
	n.a.	2.87	1849.92	0.63	24.65	0.76	10.73	0.47	0.00	0.04	3.70	0.09	0.01	4.37	11.50	2.58	7.35
	n.a.	0.15	373.30	1.12	23.43	49.55	1.23	0.29	0.02	0.15	3.77	9.33	0.00	0.97	15.00	2.26	6.01
	n.a.	0.74	859.00	0.86	49.27	12.54	20.28	0.12	0.00	0.06	1.56	1.10	0.00	1.28	2.33	0.85	3.14
	n.a.	0.12	177.12	1.01	15.22	34.70	0.87	0.16	0.00	0.08	2.19	6.55	0.00	1.43	7.18	1.07	1.42
	n.a.	0.64	822.91	0.76	34.79	13.92	10.76	0.16	0.00	0.07	1.84	1.21	0.01	1.56	4.35	0.93	2.91
	n.a.	2.28	876.59	0.56	47.48	15.28	13.22	0.08	0.00	0.08	1.67	1.84	0.01	2.42	2.43	2.11	2.80
	n.a.	3.88	202.48	2.09	7.67	3.01	55.59	0.46	0.09	0.00	0.24	0.36	0.02	8.90	0.95	0.97	2.34
	n.a.	1.55	1238.45	0.58	18.02	2.66	12.01	0.13	0.00	0.00	1.30	0.35	0.04	3.49	1.31	0.43	2.15
	n.a.	0.87	756.81	0.71	24.70	2.70	7.29	0.17	0.05	0.16	2.03	0.20	0.02	5.16	1.93	0.78	2.99
	n.a.	2.14	31.75	0.92	21.82	2.28	10.44	0.06	0.00	3.23	1.42	0.00	0.00	1.05	6.89	3.01	2.66
	n.a.	5.38	1589.73	0.79	23.28	39.12	7.85	0.22	0.00	0.21	2.00	1.07	0.01	170.47	2.08	0.69	4.31
KS10-VA-20	8.96	819.40	340.83	1158.05	354.50	7.52	0.86	1.36	11.82	0.49	7.33	<0.00	0.07	1.61	0.81	5.26	0.35
	20.68	22.30	1368.42	616.98	990.98	25.52	0.40	0.45	33.13	60.01	1.26	<0.00	0.02	1.32	15.59	180.17	31.40
	63.00	133.44	234.48	503.81	370.40	2.62	0.77	0.70	6.37	0.40	2.21	<0.00	0.06	1.02	0.63	9.46	0.44
	43.79	35.68	264.36	67.54	490.23	89.45	12.58	0.40	5.89	8.11	9.23	<0.00	0.03	1.70	7.59	170.88	10.78
	85.81	28.65	613.15	32.39	466.72	99.95	36.74	0.30	6.96	14.42	2.43	<0.00	0.01	1.71	76.32	195.66	11.74
	113.54	31.44	817.80	36.13	558.23	147.42	54.36	0.26	4.55	11.42	2.98	<0.00	0.01	2.83	36.16	189.17	12.67
	33.31	103.92	1451.75	367.95	1720.49	22.27	7.38	4.49	7.96	2.26	13.15	<0.00	0.04	0.57	95.28	417.94	12.87
	32.36	13.52	290.14	7.63	397.68	123.81	4.43	2.07	2.31	0.56	2.52	<0.00	<0.0020	1.43	2271.58	2510.17	28.80
	43.55	49.50	253.51	13.25	94.73	127.73	0.85	0.10	9.04	260.61	1.03	<0.00	<0.0031	0.48	10.77	223.68	4.74
	63.86	21.86	1332.98	185.06	836.05	156.20	32.63	0.54	69.87	158.08	3.96	<0.00	0.02	2.97	56.61	652.65	43.95
KS10-VA-20	91.43	21.41	418.22	22.39	356.33	112.18	26.71	0.30	3.55	20.05	1.60	<0.00	0.01	1.80	27.23	140.01	8.47
	54.29	10.34	44.98	4.73	77.80	87.12	0.09	0.03	0.26	0.05	0.29	<0.00	<0.0054	1.52	1.47	39.51	0.30
	36.97	19.57	751.27	24.64	1894.40	20.97	23.12	5.82	6.64	2.91	8.75	<0.00	0.01	0.83	282.49	5261.88	16.56
	12.93	10.28	77.49	363.25	278.03	90.79	0.65	0.30	2.63	1.45	0.32	<0.00	0.00	1.84	251.30	90.72	2.50
	6.02	433.82	228.50	977.10	678.99	32.50	0.75	1.75	18.65	1.38	4.53	<0.00	0.13	0.38	2.75	21.76	1.17
	396.26	166.59	2058.40	102.47	783.67	14.92	37.23	7.29	19.06	630.66	17.02	<0.00	0.03	0.47	190.52	576.36	191.80
	118.71	20.19	64.70	1.20	89.78	76.38	1.46	0.06	0.43	0.34	0.93	<0.00	<0.0036	1.16	11.67	29.51	0.91
	0.14	1.19	2.74	0.81	6.24	46.98	0.05	0.00	0.12	0.05	0.02	<0.00	<0.0048	1.07	0.04	1.25	0.20
	93.25	20.06	343.04	7.26	208.26	105.20	12.01	0.19	1.50	3.79	2.05	<0.00	0.01	1.69	22.18	103.06	4.28
	11.34	177.07	326.57	900.37	725.88	8.67	1.20	1.49	14.16	0.79	3.02	<0.00	0.09	0.55	27.09	55.61	7.61
	24.84	10.46	184.99	11.61	204.99	52.28	8.71	0.08	1.31	6.81	0.61	<0.00	0.01	2.05	11.14	65.13	5.55
	17.48	56.28	240.69	27.86	697.20	112.88	1.76	0.12	1.49	0.73	1.54	<0.00	0.02	0.36	8.50	50.39	4.18
	30.00	4.45	2.45	11.09	6.12	16.41	0.02	0.01	0.06	0.13	0.02	<0.00	<0.0043	0.59	0.08	1.88	0.05
	26.09	139.22	185.16	602.64	658.25	24.46	1.46	2.05	18.85	1.36	3.02	<0.00	0.10	0.23	1.62	12.90	0.94
	13.51	37.22	247.51	100.61	1316.17	32.96	3.47	1.01	5.83	5.28	6.58	<0.00	<0.0059	0.52	314.57	893.31	26.98
	54.37	31.17	639.46	77.00	146.72	150.85	20.29	0.45	7.28	3.67	2.24	<0.00	<0.0135	2.77	22.96	110.92	13.70
KS10-KISS-7	102.62	35.31	504.34	72.81	205.30	285.83	41.85	0.33	1.13	35.63	1.51	<0.00	0.02	2.84	12.27	147.20	6.16
	133.51	34.90	686.69	16.54	236.40	269.51	54.66	0.36	1.53	4.71	1.50	<0.00	0.01	4.46	9.63	55.56	4.23
	115.51	28.50	927.33	26.50	364.06	63.96	135.03	0.51	1.20	2.63	2.47	<0.00	0.02	5.67	13.44	40.33	4.18
	121.81	32.87	1275.53	17.53	525.40	149.02	93.06	1.19	2.09	3.47	6.56	<0.00	<0.0169	7.25	29.81	104.91	29.20

	Co	Ni	Cu	Zn	As	Se	Mo	Ag	Cd	Sn	Sb	Te	Au	Hg	Tl	Pb	Bi
	184.12	42.93	1453.78	46.02	683.36	100.04	246.10	0.75	1.34	6.67	6.42	<0.00	0.03	15.28	23.72	63.01	6.15
	96.51	27.00	834.41	24.42	336.65	104.25	49.79	0.39	1.15	2.96	2.32	<0.00	<0.0156	6.77	12.46	60.15	4.48
	141.16	33.75	1275.99	23.06	482.42	129.31	96.26	0.75	1.07	3.60	3.31	<0.00	<0.033	8.37	20.06	129.66	5.86
	165.53	62.29	1254.05	56.63	472.08	103.39	110.10	0.74	1.69	3.54	3.33	<0.00	0.02	8.47	22.15	63.28	5.80
	138.11	36.63	1118.74	54.86	411.65	99.46	114.91	0.65	1.77	3.22	2.82	<0.00	0.02	7.40	21.94	57.15	5.10
	156.75	45.03	1028.56	78.15	394.82	109.18	106.81	0.58	2.55	3.70	2.54	<0.00	0.02	6.75	19.70	73.07	5.06
	117.60	33.70	927.45	46.82	404.56	107.19	73.19	0.54	1.63	3.33	2.74	<0.00	0.02	6.41	17.77	49.51	4.53
KS10-VC-2	812.70	27.66	1601.71	52.23	28.60	27.25	11.12	0.94	0.53	1.40	0.70	<0.00	<0.018	1.32	39.25	25.44	25.92
	11.58	5.07	760.01	5.36	<1.71	11.19	1.78	<0.039	<0.238	<0.20	0.62	<0.00	<0.079	<3.68	0.80	2.37	2.23
	156.94	25.76	1751.97	25.38	28.74	25.33	20.81	0.61	1.82	13.82	2.88	<0.00	0.07	<1.57	3.58	10.52	6.64
	147.83	50.49	3228.31	413.38	40.19	<16.40	8.31	0.32	<0.57	3.00	2.81	<0.00	<0.22	<10.64	9.11	11.55	3.53
	10.33	2.15	437.27	80.86	3.25	7.72	1.25	1.52	0.82	0.16	0.16	<0.00	<0.030	<2.53	0.85	13.12	2.25
KS10-SFM-1	6.65	5.31	94.09	1.73	92.63	147.60	0.43	0.18	0.07	0.42	14.76	<0.00	0.01	6.60	35.95	48.47	7.46
	0.31	4.47	69.48	5.03	27.15	137.65	0.20	0.11	0.26	0.36	2.89	<0.00	<0.0044	2.69	9.63	17.94	2.14
	0.31	3.50	6.59	1.11	15.04	296.54	0.12	0.08	0.03	0.07	0.17	<0.00	<0.0083	2.11	3.48	4.61	2.47
	115.75	51.99	135.08	14.06	42.25	83.13	1.66	0.22	0.77	0.50	3.51	<0.00	<0.0094	5.42	43.96	46.96	6.59
	0.30	7.64	10.70	1.56	24.75	188.74	0.11	0.10	<0.025	0.81	1.59	<0.00	<0.0060	3.82	11.16	8.84	4.51
	49.28	31.71	159.54	42.99	83.51	124.35	1.82	1.24	2.14	0.90	6.19	<0.00	0.07	6.64	26.50	39.60	4.94
	275.08	42.77	260.83	10.27	66.61	66.49	49.99	0.36	0.84	0.93	8.29	<0.00	<0.020	7.44	28.37	78.78	9.31
	215.19	50.18	224.27	46.13	53.99	66.86	5.31	0.55	2.28	1.03	1.45	<0.00	<0.0164	6.25	16.03	49.16	4.17
	71.63	54.77	316.97	58.18	144.94	61.85	5.61	9.80	<1.91	140.96	8.18	<0.00	<0.30	61.75	29.77	176.71	7.60
	2.84	9.65	21.12	30.66	133.59	212.52	0.26	0.06	0.26	0.19	4.09	<0.00	0.01	2.29	41.56	24.78	4.16
	22.52	12.56	64.00	1.93	53.71	84.71	0.79	0.24	0.17	0.55	3.09	<0.00	<0.0103	6.10	20.12	30.52	5.41
	259.21	55.32	209.31	3.13	57.43	73.80	17.43	0.44	1.23	1.18	1.39	<0.00	<0.0105	6.40	20.44	41.81	4.57
	217.80	62.71	209.62	13.16	58.39	106.10	6.38	0.36	2.18	1.15	3.02	<0.00	0.01	7.58	32.08	78.69	10.26
	131.47	56.45	245.97	8.68	72.17	110.85	7.55	0.44	1.98	1.70	3.72	<0.00	0.03	8.21	43.05	76.44	11.38
	23.77	32.94	130.60	1.19	52.90	40.29	1.06	0.35	0.28	0.36	1.74	<0.00	<0.0090	8.23	30.87	34.98	6.61
	0.71	8.35	20.36	0.75	23.53	5.56	0.19	0.12	0.04	0.31	1.08	<0.00	0.02	3.20	9.01	16.74	2.87
	1.95	8.25	43.07	11.15	37.32	14.68	0.42	0.10	0.10	0.17	3.29	<0.00	0.01	5.65	15.79	11.29	2.77
	69.09	28.71	203.83	13.64	97.04	94.87	8.30	0.39	0.61	1.21	5.29	<0.00	<0.017	10.07	25.50	43.81	5.84
KS09-W2	n.a.	0.06	14.55	0.54	611.55	66.22	803.80	1.30	<0.0120	0.09	0.27	273.97	<0.00203	1.39	5.80	0.22	0.83
	n.a.	1.58	5.88	0.95	33.92	72.78	5.76	0.04	0.20	0.77	0.23	12.19	0.00	0.47	1.28	2.90	2.26
	n.a.	0.26	72.58	0.97	27.66	21.85	14.14	0.06	<0.036	0.22	0.07	16.12	<0.0053	<0.113	0.49	0.76	3.95
	n.a.	0.22	9.24	0.74	10.95	12.23	3.14	0.03	<0.041	<0.054	<0.0099	11.29	<0.0055	<0.130	0.15	0.19	0.80
	n.a.	11.80	407.75	4.27	104.00	41.38	48.10	0.50	0.91	32.78	1.38	28.08	<0.0042	0.68	3.31	38.81	9.80
	n.a.	0.05	39.77	0.45	55.51	6.99	3.18	0.21	<0.0155	<0.032	0.03	9.19	<0.0032	<0.10	3.06	2.48	14.04
	n.a.	<0.040	30.80	0.21	44.59	53.19	3.56	0.23	0.06	<0.035	0.01	39.73	<0.0030	<0.10	1.17	1.39	7.49
KS09-W2	n.a.	<0.041	8.59	0.52	49.48	49.16	22.52	0.08	0.04	0.13	0.08	40.41	<0.0032	<0.08	0.50	0.15	0.37
KS09-W4	n.a.	30.27	414.64	1627.87	1353.62	74.09	10.67	2.91	10.85	367.69	60.96	41.25	<0.139	358.35	997.85	613.62	1064.67
	n.a.	287.26	3137.02	1567.37	3433.27	1476.31	1695.58	5.45	12.81	7773.23	1705.88	76.29	<0.98	1082.14	254.39	1224.02	8895.97
	n.a.	93.87	1698.94	104.14	447.83	1018.27	216.85	1.76	<3.26	523.96	88.80	63.25	<0.33	1456.21	34.10	95.34	1475.29
	n.a.	343.22	2115.73	6800.43	1605.02	1117.72	883.25	9.21	42.74	520.31	272.96	68.32	0.19	485.75	779.27	1516.68	44763.00
	n.a.	241.29	1743.15	720.79	1803.29	726.33	731.14	3.48	9.48	221.41	87.78	71.94	<0.053	357.62	115.12	361.56	30059.00
	n.a.	66.53	152.03	121.64	108667.00	265.24	25.85	2.93	<5.41	35.92	14.32	<27.76	<0.87	1047.58	12.07	530.15	25.73

	Co	Ni	Cu	Zn	As	Se	Mo	Ag	Cd	Sn	Sb	Te	Au	Hg	Tl	Pb	Bi
	n.a.	2.78	36.83	15.40	107.11	29.96	17.59	0.10	0.72	97.37	18.54	8.08	0.00	8.05	56.84	76.75	18.61
	n.a.	n.d.	n.d.	128.41	1075.74	479.01	n.d.	n.d.	n.d.	97.64	n.d.	242.48	n.d.	n.d.	n.d.	14.97	7.02
KS09-P2	n.a.	25.21	844.21	20.55	354.08	84.88	106.80	0.45	0.84	6.00	7.04	48.51	0.01	2.36	10.85	39.13	34.89
	n.a.	0.41	8.77	0.38	5.47	86.53	0.05	n.d.	0.07	<0.029	0.02	0.23	<0.0035	0.52	0.05	0.19	0.02
	n.a.	37.22	1108.66	31.42	497.54	155.25	104.85	0.64	6.14	9.91	9.64	61.10	0.01	2.00	9.97	78.37	41.81
	n.a.	30.96	921.39	21.36	461.42	239.15	83.84	0.63	1.28	8.81	7.85	71.07	0.01	2.21	12.82	54.00	120.59
	n.a.	23.79	1089.22	26.49	776.90	69.33	120.84	0.69	1.32	9.84	10.41	55.34	0.02	2.81	68.35	636.98	56.01
	n.a.	45.33	1146.61	38.54	529.18	89.64	102.38	0.72	1.16	8.60	11.72	67.04	0.02	3.19	14.38	43.25	51.49
	n.a.	28.78	4619.19	0.41	11.18	16.08	40.77	0.04	<0.045	0.53	0.30	2.26	<0.0081	1.33	0.68	1.38	1.00
	n.a.	31.58	1171.01	27.54	439.47	81.08	326.39	0.55	0.74	7.38	9.17	61.00	0.03	2.50	11.21	36.98	43.47
	n.a.	29.39	1173.61	27.63	466.23	72.67	111.71	0.84	1.27	8.25	8.95	71.65	0.01	3.25	17.82	38.34	105.82
	n.a.	14.55	536.88	10.76	526.69	66.97	40.17	0.30	1.08	3.92	9.04	22.90	<0.0062	0.94	385.08	818.23	19.98
	n.a.	25.25	614.65	9.73	247.55	43.72	70.91	0.33	0.78	3.54	4.49	36.91	<0.0086	2.09	11.25	22.14	34.51
KS09-W6	n.a.	15.34	224.90	2.94	64.64	540.09	20.92	0.18	0.59	0.55	0.28	16.03	0.01	7.13	13.31	64.17	14.44
	n.a.	14.34	203.20	1.34	24.74	638.06	3.23	0.10	0.56	0.61	0.16	8.95	<0.0055	7.32	2.56	28.00	12.64
	n.a.	15.72	314.11	1.84	33.09	593.68	39.02	0.16	0.70	1.75	0.22	11.76	<0.00112	0.76	4.92	52.24	11.00
	n.a.	18.84	115.49	3.20	56.74	593.62	49.03	0.15	0.86	0.79	0.34	17.71	<0.00104	0.63	12.93	78.37	13.23
	n.a.	11.57	146.73	8.32	255.62	469.41	1.09	0.28	0.73	0.89	0.85	27.63	<0.00122	0.51	40.19	343.71	13.66
	n.a.	9.83	169.29	13.03	351.18	350.03	1.00	0.31	0.77	0.20	1.06	32.13	0.00	0.45	58.81	503.59	9.49
	n.a.	21.09	308.26	1.65	5.44	638.67	2.00	0.09	0.19	1.04	0.17	4.06	<0.0035	0.49	0.06	6.44	5.81
	n.a.	37.46	143.84	3.57	428.07	344.58	0.70	0.25	0.16	1.61	0.82	33.98	<0.0134	1.48	107.21	788.30	13.27
	n.a.	11.77	114.71	3.31	1145.00	193.01	0.08	0.28	0.34	0.06	1.78	75.66	<0.00113	0.30	364.79	1929.82	2.68
	n.a.	1.09	269.55	5.35	2069.48	91.16	0.08	0.46	0.88	0.10	3.49	120.45	<0.00141	0.64	492.45	3708.69	8.17
	n.a.	14.47	538.89	2.70	51.05	515.29	18.83	0.29	0.79	0.53	0.55	64.18	<0.0059	0.90	6.54	108.45	21.18
	n.a.	14.47	102.20	3.14	11.53	458.51	4.92	0.18	0.13	0.66	0.11	17.01	0.00	0.81	0.39	11.23	12.09
	n.a.	14.53	92.52	2.16	18.07	497.77	28.15	0.14	0.06	0.99	0.12	13.96	<0.0023	0.69	0.33	9.79	9.86
	n.a.	18.43	259.82	4.10	29.84	524.69	26.78	0.17	0.33	7.89	0.49	18.61	<0.0042	1.41	1.51	161.51	13.14
	n.a.	13.60	47.94	2.54	190.63	250.95	0.18	0.09	0.32	0.08	0.37	19.84	0.00	0.39	65.84	349.14	2.07
	n.a.	18.00	180.38	8.90	332.56	312.48	2.66	0.31	0.78	0.97	0.84	35.00	<0.0025	1.80	97.01	560.80	10.97
KV08-204A	n.a.	0.45	620.30	8.31	36.18	15.89	1.46	0.18	0.20	0.32	2.10	0.72	0.01	5.63	1.34	10.04	3.40
	n.a.	0.67	263.18	13.37	11.18	9.58	1.14	0.07	0.49	0.10	0.73	0.48	<0.0057	1.37	0.13	11.42	0.47
	n.a.	0.62	1087.50	9.68	27.08	8.34	6.32	0.21	<0.066	0.11	1.93	1.80	<0.0067	1.73	1.80	10.69	3.31
	n.a.	0.31	401.98	5.45	5.69	11.10	1.14	0.22	<0.035	0.09	1.52	0.83	<0.0046	1.19	1.29	4.48	0.66
	n.a.	0.36	118.17	15.30	6.12	1.25	0.95	0.27	0.07	0.44	0.92	<0.23	<0.0042	0.76	0.77	24.69	0.16
	n.a.	0.06	123.72	1.31	3.49	3.67	0.66	0.09	0.06	<0.027	0.77	<0.14	<0.0041	0.45	0.54	1.50	0.21
	n.a.	0.05	401.48	0.74	7.52	31.93	0.15	0.04	<0.018	0.11	1.00	4.27	<0.0018	1.79	5.70	2.78	0.92
	n.a.	0.58	652.26	0.55	11.15	52.98	1.56	0.06	<0.020	0.10	2.67	2.33	<0.0023	3.09	0.49	1.38	0.83
KV08-204C	n.a.	0.90	56.96	3.95	8.49	137.96	6.05	0.14	0.05	0.14	0.34	26.06	0.00	1.26	0.46	23.05	0.69
	n.a.	1.88	267.69	1.08	19.73	46.19	8.82	0.16	<0.027	0.51	0.50	11.19	<0.0045	0.90	0.80	2.14	0.72
	n.a.	72.31	1342.80	1.80	45.03	5.11	90.32	0.19	0.02	4.20	2.68	10.26	0.05	12.33	3.08	25.67	5.46
	n.a.	39.89	840.37	3.83	43.98	25.01	61.99	0.13	0.06	2.14	1.79	23.71	0.03	8.88	2.28	36.56	2.33
	n.a.	103.10	1496.26	2.53	70.57	10.30	69.72	0.24	<0.041	3.40	2.99	15.55	0.02	18.75	3.95	18.16	5.35
	n.a.	2.16	391.37	7.11	102.26	14.38	156.91	0.44	0.05	246.98	61.94	19.18	0.02	13.21	0.75	130.32	0.50
	n.a.	45.81	121.74	7.65	3.94	172.10	25.53	0.83	0.05	0.29	0.30	0.40	0.01	<0.21	0.18	53.41	0.47

	Co	Ni	Cu	Zn	As	Se	Mo	Ag	Cd	Sn	Sb	Te	Au	Hg	Tl	Pb	Bi
KV08-203	n.a.	6.60	78.24	4.19	68.43	17.44	58.36	0.51	0.10	0.26	1.32	46.33	0.08	3.99	2.32	4.50	4.12
KV08-X	n.a.	1.85	353.46	1.80	27.47	26.20	28.45	0.45	0.05	0.20	1.63	4.53	<0.0052	5.35	1.06	3.78	0.13
	n.a.	0.82	793.96	0.87	13.73	26.46	22.43	0.24	<0.029	0.03	0.24	1.72	0.01	1.14	0.58	0.92	0.11
	n.a.	6.62	395.78	5.24	32.89	29.23	116.71	0.39	<0.060	0.86	1.55	5.79	0.01	7.01	0.88	5.27	0.18
	n.a.	5.22	247.73	2.14	33.43	27.66	17.89	0.37	<0.065	1.27	1.80	2.34	<0.0051	3.36	2.07	6.70	1.03
	n.a.	6.69	1474.93	1.14	39.40	19.92	35.63	0.39	0.03	0.11	0.44	6.15	0.01	2.44	3.13	3.30	0.45
KV08-X	n.a.	17.02	1639.14	2.49	80.96	24.03	152.79	0.48	<0.047	1.88	1.81	45.95	0.01	15.34	3.34	24.84	1.10
	n.a.	269.17	565.78	2.71	1417.89	117.46	328.62	4.21	0.18	0.36	1.72	19.12	0.02	5.61	2.64	762.55	3.38

n.d. indicates that the element was not detected and n.a. indicates that the element was not analyzed

Appendix III: Whole rock compositions of unaltered Kawah Ijen volcanic rocks. Major element oxides are reported in wt% and trace elements in ppm. The data are from Berlo, 2001.

	SiO ₂	TiO ₂	Al ₂ O ₃	Fe ₂ O ₃	MnO	MgO	CaO	Na ₂ O	K ₂ O	P ₂ O ₅	Co	Ni	Cu	Zn	Zr	Nb	Pb
KV32	50.62	0.95	20.28	9.85	0.18	3.66	9.98	2.95	1.18	0.21	29	10	120	82	82	4	6
KV58	50.50	0.96	18.74	11.09	0.19	5.00	9.00	2.86	1.21	0.25	32	21	136	83	91	4	6
KV30	50.71	0.94	20.15	9.86	0.17	3.72	9.81	2.99	1.17	0.22	29	10	92	81	88	4	7
KV75	58.94	0.75	17.29	7.47	0.15	2.74	6.23	3.41	2.65	0.20	18	6	38	67	84	4	11
KV20	50.39	1.02	18.75	10.98	0.19	4.51	9.72	3.06	1.14	0.22	33	13	112	85	90	4	4
KV17	58.89	0.79	17.18	7.48	0.15	2.85	6.41	3.50	2.55	0.18	19	8	72	81	92	5	9
KV35	52.02	0.94	20.29	9.18	0.17	3.11	9.31	3.38	1.24	0.25	24	6	82	78	94	6	6
KV883	51.35	1.10	19.87	9.72	0.17	3.04	9.53	3.16	1.11	0.29	27	8	48	82	95	4	6
KV822	56.27	0.74	19.80	6.97	0.13	2.41	7.27	3.62	2.09	0.24	18	7	29	62	91	5	8
KV825	50.21	1.09	19.58	10.37	0.16	3.76	9.28	3.07	1.17	0.31	28	12	122	82	108	5	5
KV884	57.58	0.86	17.54	8.07	0.15	2.95	6.38	3.59	2.74	0.19	22	7	48	71	81	3	11
KV826	51.55	1.03	19.65	9.34	0.18	3.12	9.12	3.00	1.34	0.28	25	6	106	81	76	3	6
KV827	51.32	1.09	19.75	9.63	0.17	3.18	9.43	3.22	1.33	0.28	25	8	164	83	143	6	6
KV844	64.23	0.49	17.42	4.04	0.09	1.12	4.17	4.03	3.80	0.11	7	5	32	48	184	11	17
KV74	51.16	0.96	20.53	9.25	0.17	2.54	8.33	2.90	1.30	0.26	25	6	141	89	173	8	8
KV13	50.35	0.97	20.01	10.27	0.18	4.01	9.97	3.06	1.10	0.21	30	12	150	81	271	12	6
KV07	51.39	0.95	20.31	9.40	0.18	3.39	9.83	3.16	0.98	0.21	24	7	100	79	271	12	6

Appendix IV: Major (wt%) and trace element (ppm) whole rock compositions of altered rocks from the Kawah Ijen crater.

	SiO ₂	Al ₂ O ₃	Fe ₂ O ₃	MgO	CaO	Na ₂ O	K ₂ O	TiO ₂	P ₂ O ₅	MnO	Cr ₂ O ₃	TOT/C (%)	TOT/S (%)	LOI
KS09-1B	47.64	14.09	0.28	0.18	7.22	0.34	2.84	0.64	0.24	<0.01	<0.002	0.02	7.23	22
KS09-2B	58.38	20.22	0.59	0.13	0.15	0.17	2.05	0.79	0.11	0.03	0.01	0.03	3.67	16.9
KS09-3E	37.8	8.19	0.66	0.31	15.38	0.2	1.66	0.58	0.16	<0.01	0.003	0.17	11.21	19.8
KS09-3F	44.75	14.36	2	0.15	4.26	0.69	1.87	0.7	0.08	<0.01	0.01	0.04	7.97	30.9
KS09-7F	33.47	23.51	0.16	0.03	0.1	0.13	4.14	0.44	0.15	<0.01	<0.002	0.03	9.16	37.7
KS09-7TB	33.01	23.04	0.73	0.06	0.73	1.05	4.93	0.44	0.24	<0.01	0.002	0.05	9.42	35.4
KS09-7U	82.81	3.49	0.55	0.05	0.17	0.3	0.6	0.98	0.09	<0.01	0.02	0.05	2.11	10.8
KS09-7V	36.48	19.86	0.18	0.01	0.45	1.32	3.04	0.51	0.25	<0.01	0.007	0.02	9.05	37.5
KS09-8H	90.93	2.36	0.85	0.02	0.07	0.08	0.21	1.07	0.07	<0.01	<0.002	<0.02	0.3	4.3
KS09-8Y	71.93	10.42	1.51	<0.01	0.04	0.19	0.95	0.49	0.18	<0.01	<0.002	<0.02	2.26	14.2
KS09-8ZB	24.86	26.87	11.62	0.03	0.09	0.29	2.38	0.3	0.23	<0.01	<0.002	<0.02	13.25	33.1
KS09-10B	19.5	29.03	0.89	0.05	1.75	1.41	2.04	0.29	0.25	<0.01	0.002	0.04	10.34	44.5
KS09-11B	32.55	22.18	0.16	0.01	0.32	0.63	4.26	0.32	0.21	<0.01	<0.002	0.03	8.62	38.9
KS09-11C	39.45	22.61	0.15	0.02	0.13	0.41	5.72	0.38	0.16	<0.01	0.003	0.03	8.11	30.6
KS09-11Y	36.14	19.82	0.86	0.02	0.05	1.83	3.09	0.43	0.07	<0.01	<0.002	0.03	9.7	37.6
KS09-13B	80.84	2.82	2.96	0.06	0.13	0.09	0.46	0.54	0.06	<0.01	<0.002	<0.02	4.48	12
KS09-14W	34.8	16.74	3.93	0.02	0.09	0.97	3.34	0.38	0.03	<0.01	<0.002	<0.02	16.74	39.6
KS09-15W	8.62	19.66	19.5	0.01	0.26	2.58	1.54	0.12	0.1	<0.01	<0.002	<0.02	28.82	47.5
KS09-16EX	0.43	0.05	<0.04	<0.01	<0.01	<0.01	<0.01	<0.01	<0.01	<0.01	<0.002	0.03	100.2	99.5
KS10-KISS-6	80.95	2.08	0.86	0.09	0.12	0.15	0.11	1.24	0.05	0	0.012	<0.02	4.49	14.3
KS10-KISS-7	2.49	0.42	48.55	<0.01	0.07	0.04	0.08	0.21	0.02	0.02	0.007	0.14	60.22	47.8
KS10-KISS-8	85.35	1.45	0.66	0.07	0.07	0.12	0.11	0.96	0.05	0	0.004	<0.02	1.24	11
KS10-KISS-15	31.42	1.82	22.3	0.13	0.22	0.16	0.21	0.52	0.06	0.01	0	0.06	48.05	43
KS10-KISS-17	76.51	4.37	4.09	0.08	0.2	0.11	0.55	0.95	0.06	0.01	0.005	0.03	6	12.9
KS10-KISS-19	60.77	1.72	8.95	0.04	0.08	0.07	0.35	0.82	0.1	0	0	0.04	9.26	26.9
KS10-VA-3	59.61	11.82	4.7	0.38	0.94	0.88	3.01	0.78	0.18	0.06	0.003	0.07	4.1	17.5
KS10-VA-4	50.66	19.48	3.89	0.38	1.09	2.29	3.19	0.53	0.16	0.04	0.008	0.03	3.68	18.1
KS10-VA-7	62.09	6.79	10.54	0.34	0.89	0.36	1.84	0.95	0.11	0.05	0.002	0.03	6.33	15.9
KS10-VA-9	59.18	17.98	1.37	0.11	0.31	0.39	2.36	0.71	0.18	0.02	0	0.04	2.71	17.3
KS10-VA-13	76.76	2.61	7.06	0.11	0.18	0.09	0.33	0.94	0.04	0.05	0.002	0.05	3.31	11.7
KS10-VA-15	43.38	11.19	11.15	0.02	0.03	0.32	2.83	0.49	0.2	0	0	0.04	14.7	30.2
KS10-VA-23	47.17	4.31	20.08	0.02	0.07	0.04	0.08	0.54	0.06	0	0.004	0.07	19.92	27.5
KS10-VB-1	79.08	7.14	2.15	0.28	0.77	0.24	1.97	0.85	0.08	0.04	0.013	0.04	0.35	7.3
KS10-VB-2	75.27	8.67	2.43	0.25	0.72	0.17	2.05	0.87	0.08	0.04	0	0.02	0.71	9.3
KS10-VA-10B	74.52	2.47	4.06	0.04	0.15	0.12	0.32	1.08	0.05	0	0	0.06	6.71	17.1
KS10-VC-2	82.1	2.26	1.38	0.14	0.26	0.21	0.48	0.74	0.05	0.02	0	<0.02	1.32	12.3
KS10-VC-3	84.95	1.24	0.68	0.11	0.13	0.09	0.14	0.24	0.03	0.01	0	0.02	1.76	12.4
KS10-VC-4	87.17	1.57	1.5	0.03	0.09	0.17	0.23	0.48	0.03	0	0.005	0.04	1.33	8.6
KS10-VC-5	80.51	5.16	1.31	0.05	0.29	0.04	0.81	1.23	0.1	0.02	0.008	0.05	3	10.4
KS10-VC-9	87.9	0.36	0.63	0.05	0.05	0.05	0.07	0.23	0.04	0	0.008	0.04	0.41	10.5
KS10-VC-11	81.14	1.95	0.6	0.06	0.07	0.07	0.42	1.59	0.06	0	0.005	0.03	6.57	13.9

	Sum	Ba	Be	Co	Cs	Ga	Hf	Nb	Rb	Sn	Sr	Sc	Ta	Th
KS09-1B	95.52	746	<1	<0.2	1.2	11.4	4.2	6.3	39.7	7	739.9	31	0.3	7.9
KS09-2B	99.55	652	<1	0.9	1.6	19.8	4.9	8.1	23	22	310.1	26	0.5	10.8
KS09-3E	84.72	357	<1	1.3	0.6	13	2.9	5.2	35.9	20	486.7	21	0.3	10.7
KS09-3F	99.76	220	<1	3.9	0.7	11.2	3.7	6.4	34.3	27	184.3	16	0.3	3.9
KS09-7F	99.83	523	<1	<0.2	4.7	13.9	3.4	4.2	67.1	8	329.5	42	0.3	15.8
KS09-7TB	99.67	478	1	5.7	<0.1	17.1	2.1	3.9	49.2	8	520.5	13	0.2	12.9
KS09-7U	99.91	480	<1	1.3	0.4	2.4	6.1	10.1	5.8	6	204.9	6	0.6	11.1
KS09-7V	99.56	400	<1	0.4	<0.1	17.2	3.1	3.7	54.7	9	448.8	10	0.2	14.7
KS09-8H	99.97	257	<1	1.9	0.4	1.5	9.6	11.5	9.9	20	31.5	7	0.8	7.1
KS09-8Y	99.89	293	<1	0.7	0.2	10.9	9.5	12.9	6.7	12	194.7	7	0.9	18.3
KS09-8ZB	99.77	456	3	11.3	0.2	51.4	2	3.3	10.8	12	333.5	35	0.2	21.5
KS09-10B	99.68	242	1	2.7	1.5	15.2	1.2	2.9	148.2	39	269.6	9	0.1	11.1
KS09-11B	99.54	168	<1	0.9	0.3	11.1	2.4	3.3	255.2	68	396.7	39	0.2	13.1
KS09-11C	99.6	423	2	0.6	2	5.6	3.5	4.2	123.6	4	506.6	9	0.3	8
KS09-11Y	99.88	959	<1	3.1	<0.1	5.1	4.4	5.3	16.4	3	165.1	4	0.3	2.6
KS09-13B	99.94	167	1	6.5	0.6	5.2	9.7	13	29.1	5	111.8	5	1	6.2
KS09-14W	99.9	162	<1	19	0.3	2.6	3.9	5	15.8	2	315.1	3	0.4	2.9
KS09-15W	99.89	68	2	26.8	0.3	11.5	1	1.1	17.8	6	264	8	<0.1	9.2
KS09-16EX	99.99	32	<1	0.5	<0.1	<0.5	0.2	0.2	0.1	<1	0.9	<1	<0.1	<0.2
KS10-KISS-6	99.95	267	<1	2.8	0.6	2.3	7.9	10.6	7.6	5	13.5	8	0.7	4.7
KS10-KISS-7	99.76	0	<1	159.5	0.2	1.4	0.6	2.3	2.3	6	11.8	1	0.2	0.7
KS10-KISS-8	99.87	841	<1	1.5	1.2	3.6	6.7	11.2	8.4	13	137.4	8	0.9	9.9
KS10-KISS-15	99.87	202	<1	110.2	0.5	2.6	6.2	5	8.7	3	31.5	8	0.3	3.1
KS10-KISS-17	99.88	556	<1	15.6	3.2	4	7.5	10.9	60.2	4	173.8	7	0.7	8.9
KS10-KISS-19	99.84	530	<1	9.8	0.7	1.6	4.7	7.3	8.3	7	411.5	8	0.5	9.2
KS10-VA-3	99.86	540	1	11	4	12.6	4.8	7.7	80.4	2	290.7	16	0.5	10
KS10-VA-4	99.85	512	1	3.3	3.4	14.7	5.3	7.6	90.1	2	385.6	14	0.4	10.1
KS10-VA-7	99.88	396	<1	85.5	3.2	8.3	5.4	7.8	64.8	7	75.5	7	0.5	7.1
KS10-VA-9	99.85	606	<1	1.4	4.1	17.8	5.1	8.1	105.9	1	292.9	21	0.5	11.2
KS10-VA-13	99.89	577	<1	6.5	2.5	3.5	8.7	11.3	40.2	7	24.2	5	0.9	6.3
KS10-VA-15	99.85	423	<1	23.3	0.2	18.5	4.2	5.5	8.6	12	352.9	8	0.3	8
KS10-VA-23	99.86	874	<1	39.1	0.2	3.2	6.8	6.2	2.7	12	29	7	0.6	4.6
KS10-VB-1	99.88	870	1	3.8	3.6	7.6	6.4	10.7	76.1	5	65	5	0.7	9.8
KS10-VB-2	99.88	779	1	4	5	7.9	7.5	11.2	111.2	5	54.1	6	0.8	9.5
KS10-VA-10B	99.89	758	<1	4.7	1.7	2.6	6.3	10.3	34.4	10	44	3	0.6	4.6
KS10-VC-2	99.96	399	<1	3.2	1.4	3.4	3.9	7.9	26	5	36.9	2	0.7	5
KS10-VC-3	100.02	34	<1	2.5	0.6	1.9	3.1	3.7	14.3	1	9.2	2	0.8	1.6
KS10-VC-4	99.87	830	<1	10.1	0.6	1.6	10.6	13.4	11	17	45.6	2	1.1	8.2
KS10-VC-5	99.87	892	<1	2.7	5.2	5.4	6.9	12	121.7	20	21.3	5	0.8	8.1
KS10-VC-9	99.91	794	<1	3.6	0.8	1.3	5.5	10.4	3.5	6	99	1	0.7	7.2
KS10-VC-11	99.88	814	<1	2.8	1.2	1.3	9.8	11	17.2	12	37.1	15	0.9	1.4

	U	V	W	Zr	Y	La	Ce	Pr	Nd	Sm	Eu	Gd	Tb	Dy
KS09-1B	3.6	218	0.8	153.1	30	23.6	53.8	6.67	28.8	5.94	1.45	4.83	0.7	4.25
KS09-2B	4	225	1.4	175.1	8.3	10.8	14.1	1.2	3.8	0.5	0.11	0.57	0.12	0.98
KS09-3E	1.9	183	1.2	108.1	11.9	17.1	36.7	4.58	22.2	6.08	1.82	9.61	1.16	3.65
KS09-3F	1.5	167	2.5	136.7	6.4	6.6	16	2.11	9.3	1.67	0.47	1.61	0.22	1.22
KS09-7F	2.7	253	0.8	103	15.5	19.8	51.4	6.35	25.9	4.67	1.05	3.15	0.48	2.86
KS09-7TB	1.9	132	9.3	89.9	1.6	22.9	43.7	4.05	12.7	2.59	1.07	4.24	0.37	0.9
KS09-7U	1.7	43	5.1	234	9.5	19.6	36.9	3.57	11	1.39	0.3	1.13	0.2	1.3
KS09-7V	1.7	142	2.3	116.9	5	52	105.3	11.35	41	4.71	0.97	1.5	0.23	1.11
KS09-8H	1.4	26	1.2	332.3	2.1	2.2	3.2	0.25	0.8	0.16	0.03	0.18	0.04	0.29
KS09-8Y	3.4	61	3.1	312.8	6.6	17.9	35.7	3.56	12.5	2.54	0.92	2.07	0.28	1.17
KS09-8ZB	1.4	431	2.4	73.8	7.8	73.8	160.2	17.73	64.3	6.98	1.24	3.26	0.35	1.42
KS09-10B	0.9	159	<0.5	50.7	1.8	22.8	49	4.94	15.2	2.53	1.1	2.94	0.27	0.84
KS09-11B	2.4	216	2.4	96.7	22.7	36.4	68	7.13	24.7	4.42	1.66	6.21	0.87	4.65
KS09-11C	1	267	2.5	129.2	4.2	12.8	29.9	4.16	19.5	3.39	1.07	2.95	0.25	0.96
KS09-11Y	1.1	147	3.1	197.2	2.4	9.6	10.1	0.61	1.3	0.13	0.04	0.17	0.03	0.26
KS09-13B	2.9	41	0.9	315	8.5	13.3	27.1	2.92	10.3	1.49	0.23	1.03	0.18	1.08
KS09-14W	0.9	73	1.1	125.6	3	16.8	16.2	0.86	1.8	0.23	0.05	0.22	0.05	0.36
KS09-15W	0.6	229	<0.5	36.7	2.4	18.2	38.2	5.13	22.9	4.62	1.15	3.58	0.33	0.86
KS09-16EX	<0.1	<8	<0.5	7.2	0.1	0.1	0.6	<0.02	<0.3	<0.05	<0.02	<0.05	<0.01	<0.05
KS10-KISS-6	1.4	40	1.2	239.5	7.5	2.3	5.1	0.6	2.3	0.71	0.07	0.88	0.17	1.1
KS10-KISS-7	0.2	15	0.6	21.8	1.3	1.1	1.9	0.2	1	0.17	0.03	0.16	0.03	0.16
KS10-KISS-8	2.8	41	1.2	245.4	13.6	10	15.7	1.6	5.7	1.35	0.14	1.62	0.33	2.15
KS10-KISS-15	1	47	0.7	289.9	6.7	3.4	7	0.72	3.2	0.54	0.13	0.85	0.15	0.92
KS10-KISS-17	2.4	35	2	257.6	16.2	20.2	29.7	2.45	8.9	1.83	0.24	2.4	0.41	2.42
KS10-KISS-19	2.1	58	1.5	174.1	7.7	25.9	44.5	4.28	15.7	2.21	0.41	1.72	0.23	1.29
KS10-VA-3	2.5	148	1.3	180.5	17.2	21.6	44.4	5.1	20.7	3.64	0.67	3.1	0.52	2.82
KS10-VA-4	2	114	1.3	165.3	16.3	20.8	47	4.57	16.1	2.99	0.66	3.34	0.54	3.2
KS10-VA-7	2.5	73	1.2	204.1	15.9	14.1	30.6	3.45	13.9	2.83	0.49	2.69	0.44	2.46
KS10-VA-9	2.5	192	1.2	186	10.7	22	42.6	4.07	13.5	2.32	0.34	2.04	0.31	1.74
KS10-VA-13	2	32	1.8	285.1	10	6.4	13.6	1.54	5.6	1.29	0.12	1.41	0.24	1.45
KS10-VA-15	1.4	72	3.2	148.8	3.4	13.3	28.3	2.99	11.2	1.53	0.27	0.95	0.11	0.55
KS10-VA-23	1.9	41	1.4	237.8	3	2.6	3.6	0.27	1.1	0.14	0.04	0.21	0.05	0.36
KS10-VB-1	2.3	36	1.9	206.1	16.7	15.3	32.1	3.69	14.5	2.97	0.42	2.79	0.47	2.85
KS10-VB-2	2.7	45	1.8	254.7	17.8	15.9	32.6	3.8	15.5	3.02	0.39	2.92	0.5	2.96
KS10-VA-10B	1.8	28	1.8	231.6	8.2	4.1	8.4	0.91	3.5	0.81	0.1	0.86	0.17	1.07
KS10-VC-2	1.1	16	1.8	134.6	8	6.7	11.9	1.29	4.7	1.01	0.09	0.98	0.18	1.14
KS10-VC-3	0.4	11	<0.5	80.4	2.8	1.3	2.2	0.29	1.3	0.37	0.06	0.37	0.07	0.42
KS10-VC-4	3.1	21	1.7	390.6	13.4	6.5	14.6	1.44	4.9	1.42	0.12	1.62	0.32	1.93
KS10-VC-5	2.2	42	1.4	241.4	12.4	11.8	24.4	2.75	11.1	2.3	0.23	2.19	0.35	2.02
KS10-VC-9	1.8	<8	1.1	191.3	7.2	12.8	20.7	1.55	4.7	0.85	0.04	0.84	0.17	1.08
KS10-VC-11	1.2	14	1.6	386.7	1.4	2	2.6	0.28	1	0.21	0.02	0.22	0.04	0.32

	Ho	Er	Tm	Yb	Lu	Mo	Cu	Pb	Zn	Ni	As	Cd	Sb	Bi
KS09-1B	0.9	3.05	0.54	3.68	0.62	0.4	0.3	7.3	<1	0.2	5.5	<0.1	0.3	1.9
KS09-2B	0.26	0.94	0.17	1.56	0.28	0.4	4.1	83.2	15	1.2	10.7	<0.1	0.6	1.6
KS09-3E	0.54	1.53	0.24	1.86	0.3	1.1	6.7	24	76	2.1	11.5	0.1	2.4	1.2
KS09-3F	0.23	0.71	0.1	0.88	0.15	0.6	9.6	19.8	150	3.8	25.1	0.1	0.5	7.7
KS09-7F	0.6	1.82	0.29	1.82	0.28	4.4	0.3	26.3	<1	0.7	9	<0.1	<0.1	12.2
KS09-7TB	0.07	0.15	0.03	0.22	0.04	8.5	10.7	26.1	54	1.6	4	<0.1	0.4	0.8
KS09-7U	0.29	1.14	0.18	1.49	0.27	2.6	7.2	33	12	8.9	6.5	<0.1	0.6	0.9
KS09-7V	0.18	0.53	0.07	0.65	0.11	1.7	1.9	51.7	3	1.2	6	<0.1	0.4	0.6
KS09-8H	0.08	0.28	0.05	0.43	0.08	3.1	4	2.6	<1	2.5	4	<0.1	0.3	1.7
KS09-8Y	0.25	0.85	0.16	1.27	0.23	3.6	1.2	40.8	<1	0.5	20.5	0.3	0.6	7.3
KS09-8ZB	0.24	0.85	0.13	1.1	0.17	44.7	46.1	18.1	4	4.7	113.8	0.2	0.7	3.5
KS09-10B	0.07	0.15	0.02	0.17	0.03	13.7	31.2	33.5	3	0.9	36.9	<0.1	0.3	23.8
KS09-11B	0.85	2.38	0.32	2.42	0.4	14.6	9.4	4.9	2	0.3	11.8	<0.1	<0.1	3.1
KS09-11C	0.13	0.37	0.06	0.54	0.1	2.5	8	5.4	1	0.7	27.5	<0.1	<0.1	0.4
KS09-11Y	0.07	0.29	0.05	0.53	0.1	3.2	13.4	22.9	52	1.6	3.9	<0.1	0.3	1.3
KS09-13B	0.29	1.09	0.21	1.47	0.27	15.1	55.4	7.1	<1	2.4	37.6	<0.1	2	5.8
KS09-14W	0.11	0.38	0.08	0.53	0.1	14.7	129.8	12.4	1	4.6	19.5	<0.1	0.8	1.8
KS09-15W	0.08	0.18	0.04	0.33	0.06	11.5	39.1	4.4	2	4.1	68.2	<0.1	5.8	3.3
KS09-16EX	<0.02	<0.03	<0.01	<0.05	<0.01	0.1	1.2	0.2	2	0.1	1.1	<0.1	<0.1	<0.1
KS10-KISS-6	0.24	0.8	0.14	0.94	0.16	1.9	8	3.5	2	1.6	12.7	<0.1	5	1.4
KS10-KISS-7	0.05	0.13	0.03	0.17	0.03	108.2	1110.1	49.9	23	33.1	366.9	0.8	4.6	54.3
KS10-KISS-8	0.5	1.63	0.28	1.86	0.3	4	5.2	81.5	1	0.9	13	<0.1	5.9	2
KS10-KISS-15	0.21	0.73	0.13	0.84	0.14	6.2	328.9	7.1	9	26.8	79	0.2	3.2	12.6
KS10-KISS-17	0.57	1.8	0.3	1.77	0.3	2.2	79.8	83.4	4	4.8	32.1	0.1	0.9	4.3
KS10-KISS-19	0.3	0.86	0.15	1.11	0.18	1.5	148.4	108.8	6	5.4	100.4	0.4	2.8	9.9
KS10-VA-3	0.61	1.76	0.27	1.81	0.29	2.4	34.5	6.5	8	6.8	6.6	0.1	0.1	1.3
KS10-VA-4	0.61	1.83	0.27	1.83	0.28	1.3	9	7	6	1.9	9.5	<0.1	<0.1	1.3
KS10-VA-7	0.52	1.58	0.26	1.6	0.26	4.3	76.4	36.4	21	20.5	43.3	0.4	0.1	1.3
KS10-VA-9	0.35	1.03	0.17	1.27	0.18	0.6	13.9	6.6	2	0.9	1.9	<0.1	<0.1	3.3
KS10-VA-13	0.35	1.06	0.18	1.21	0.19	4.4	163.2	15.7	13	4.1	21.4	<0.1	0.6	6.1
KS10-VA-15	0.12	0.44	0.07	0.67	0.1	8.3	164.8	26.2	2	6.4	31.3	<0.1	0.8	14.4
KS10-VA-23	0.09	0.34	0.09	0.63	0.13	6.1	55.5	4	6	9.4	9.7	3.5	1.4	12
KS10-VB-1	0.6	1.82	0.28	1.8	0.29	2.5	11.2	5.3	2	2.1	4.4	<0.1	0.5	0.8
KS10-VB-2	0.63	1.92	0.29	1.97	0.3	1	10	5	3	2.1	1.5	<0.1	0.7	0.4
KS10-VA-10B	0.27	0.85	0.17	0.99	0.17	4.5	20.7	5.1	3	2	8.1	<0.1	0.3	1.7
KS10-VC-2	0.3	0.75	0.13	0.81	0.13	2.4	30.7	2.6	2	1.8	10.5	<0.1	0.9	2.1
KS10-VC-3	0.09	0.28	0.05	0.29	0.06	0.9	5.2	1.2	2	1.2	7.4	<0.1	0.7	1.7
KS10-VC-4	0.46	1.5	0.27	2.03	0.34	12.9	47.8	2.9	1	1.9	10.9	<0.1	0.9	7.4
KS10-VC-5	0.44	1.18	0.21	1.33	0.22	2.9	25.6	2.1	3	2.3	3.6	<0.1	0.5	7.1
KS10-VC-9	0.28	0.86	0.14	1.01	0.17	1.5	12.2	34.4	2	1.7	5	<0.1	0.8	0.3
KS10-VC-11	0.05	0.17	0.03	0.25	0.04	2.6	18.9	7.7	2	2.7	3.7	<0.1	0.9	3.2

	Ag	Au (ppb)	Hg	Tl	Se	Te
KS09-1B	<0.1	1.2	0.13	0.3	1.2	<1
KS09-2B	<0.1	1.4	<0.01	0.4	2.5	<1
KS09-3E	0.1	2.6	1.36	0.1	7	<1
KS09-3F	0.9	4.6	0.59	1.1	2.7	<1
KS09-7F	<0.1	<0.5	0.07	2.2	4.4	1
KS09-7TB	0.2	4.9	0.15	0.1	2	<1
KS09-7U	0.2	2.9	0.55	<0.1	2.5	<1
KS09-7V	<0.1	2.5	0.27	<0.1	2.3	<1
KS09-8H	<0.1	3.2	0.05	0.1	2	<1
KS09-8Y	<0.1	<0.5	3.15	2.5	3.6	<1
KS09-8ZB	<0.1	<0.5	2	1.2	23.1	6
KS09-10B	<0.1	4.5	0.35	3.7	18.9	2
KS09-11B	<0.1	6.3	0.53	0.7	9.8	2
KS09-11C	<0.1	2.4	0.14	0.2	2.4	<1
KS09-11Y	0.3	2.7	0.03	0.1	2.3	<1
KS09-13B	<0.1	0.9	2.85	1	10.2	4
KS09-14W	<0.1	2.5	1.6	0.9	6.6	2
KS09-15W	<0.1	2.5	3.01	2.6	15.8	8
KS09-16EX	<0.1	<0.5	0.31	<0.1	36.7	4
KS10-KISS-6	<0.1	2	3.39	0.2	16	2
KS10-KISS-7	0.5	0.9	6.55	13.8	76.5	30
KS10-KISS-8	<0.1	1	2.47	0.3	5.3	3
KS10-KISS-15	0.1	1.2	2.87	3.6	27.3	10
KS10-KISS-17	0.1	1.5	0.17	4.2	10.5	2
KS10-KISS-19	<0.1	1.1	0.07	14.6	13.2	4
KS10-VA-3	<0.1	1.3	0.05	1.4	1.4	<1
KS10-VA-4	<0.1	1	0.05	0.6	1.2	<1
KS10-VA-7	<0.1	3.3	0.08	4.1	1.5	<1
KS10-VA-9	<0.1	1.2	<0.01	0.2	<0.5	<1
KS10-VA-13	<0.1	4.5	0.46	1.8	1.5	2
KS10-VA-15	<0.1	1.4	0.14	2.9	12.2	3
KS10-VA-23	<0.1	2.3	0.27	0.3	>100.0	2
KS10-VB-1	<0.1	<0.5	0.25	<0.1	1.2	<1
KS10-VB-2	<0.1	1.5	0.94	<0.1	6.6	<1
KS10-VA-10B	<0.1	1.8	0.13	0.6	1.4	<1
KS10-VC-2	<0.1	0.9	0.17	0.9	1.2	1
KS10-VC-3	<0.1	0.9	0.22	0.4	0.8	<1
KS10-VC-4	0.3	1	0.63	0.2	5.7	<1
KS10-VC-5	<0.1	<0.5	0.09	1.1	1.3	<1
KS10-VC-9	<0.1	0.9	0.31	0.2	0.6	<1
KS10-VC-11	<0.1	<0.5	0.51	0.3	3.5	<1

Appendix V: Composition of pyrite grains from the altered rocks at Kawah Ijen based on EMP analyses. Major element oxides are reported in wt% and trace elements in ppm.

	As	Cu	Se	Te	SO ₃	FeO
KS09-VA9	n.d.	570	n.d.	n.d.	51.85	45.84
	n.d.	n.d.	270	n.d.	53.38	46.39
	n.d.	1170	n.d.	n.d.	52.22	46.62
	810	500	n.d.	n.d.	52.94	46.15
	600	n.d.	n.d.	n.d.	52.78	46.77
	730	n.d.	n.d.	n.d.	53.24	46.64
	680	n.d.	n.d.	n.d.	53.30	46.56
KS09-C4	600	n.d.	300	480	51.72	45.51
	540	650	460	450	52.51	46.09
	600	n.d.	340	320	53.14	45.81
	n.d.	1000	250	n.d.	52.55	46.10
	530	480	n.d.	n.d.	52.06	46.15
KS09-C5	n.d.	n.d.	370	n.d.	51.95	45.56
	990	1480	n.d.	n.d.	52.77	45.99
	n.d.	1390	n.d.	n.d.	52.91	46.19
	n.d.	n.d.	460	n.d.	52.80	46.66
	620	570	n.d.	n.d.	52.94	45.72
	n.d.	680	n.d.	n.d.	52.10	46.70
	n.d.	780	n.d.	n.d.	52.34	46.41
	n.d.	780	240	n.d.	52.34	45.36
	n.d.	n.d.	240	n.d.	52.81	46.62
	n.d.	630	n.d.	n.d.	53.70	46.71
	n.d.	440	n.d.	n.d.	53.00	46.83
	n.d.	1170	n.d.	n.d.	53.26	46.87
	n.d.	1860	n.d.	n.d.	51.85	46.17
	n.d.	890	n.d.	n.d.	53.11	46.79
	n.d.	1210	n.d.	n.d.	51.93	46.53
	n.d.	n.d.	220	n.d.	52.73	46.41
	n.d.	2000	n.d.	n.d.	52.35	46.64
	n.d.	2000	n.d.	n.d.	53.37	46.49
	n.d.	2000	n.d.	n.d.	53.78	46.44
	n.d.	1510	n.d.	n.d.	53.29	46.67
	n.d.	1920	n.d.	n.d.	53.30	46.42
	n.d.	880	n.d.	n.d.	53.08	46.79
KS09-C2	520	n.d.	n.d.	n.d.	52.95	46.62
	n.d.	550	n.d.	n.d.	53.19	46.56
	n.d.	1570	n.d.	n.d.	53.94	46.45
KS09-C3	n.d.	640	240	n.d.	53.41	46.25
	n.d.	480	n.d.	n.d.	53.50	46.20
	n.d.	n.d.	390	n.d.	51.78	45.30
	780	510	440	460	51.64	45.31
	529	520	320	440	52.18	45.59
	n.d.	760	350	n.d.	52.74	45.31
	870	850	250	380	52.16	45.39
KS10-KISS-7	n.d.	510	n.d.	n.d.	53.75	46.21
	820	980	n.d.	n.d.	53.35	46.05
	n.d.	630	n.d.	n.d.	54.26	45.97
	n.d.	410	n.d.	n.d.	53.30	46.54
	120	450	n.d.	n.d.	53.45	46.35
KS10-VA20	630	n.d.	n.d.	n.d.	52.97	46.40
	n.d.	430	n.d.	n.d.	53.36	46.62
	n.d.	n.d.	2000	n.d.	51.88	46.57
KS10-VA15	n.d.	1010	n.d.	n.d.	53.58	45.25
	490	1000	n.d.	n.d.	55.16	45.60
	n.d.	400	n.d.	n.d.	54.11	45.29
	n.d.	400	n.d.	n.d.	54.30	45.60
	n.d.	410	n.d.	n.d.	53.59	46.10
	n.d.	700	n.d.	n.d.	53.82	46.10
	n.d.	2000	n.d.	n.d.	53.11	46.05
	n.d.	2000	n.d.	n.d.	53.58	45.86
	n.d.	2000	n.d.	n.d.	53.35	45.92
	n.d.	2000	n.d.	n.d.	53.25	46.10
	n.d.	590	n.d.	n.d.	53.19	46.23
	n.d.	680	n.d.	n.d.	53.35	46.25
	n.d.	580	n.d.	n.d.	53.08	46.31
	n.d.	490	n.d.	n.d.	52.83	46.15
KS10-VA23	n.d.	500	n.d.	n.d.	53.98	46.46
KS10-VB5A	530	n.d.	n.d.	n.d.	53.78	46.44
KS10-SFM-1	n.d.	n.d.	n.d.	n.d.	52.61	46.04

n.d. indicates that the element was not detected and n.a. indicates that the element was not analyzed.

Appendix VI: Compositions of fumarolic gases and their condensates at the active dome in the Kawah Ijen crater.

Sample no.	KV07-402	KV07-411	KV07-421	KV08-003	KV08-010	KV08-014	Best estimate	1 σ
Year	2007	2007	2007	2008	2008	2008	2007-2008	
Gas collected (g)	9.61	13.38	9.88	3.86	4.88	8.81		
Temperature (°C)	495	330	335	490	>400	>400		
Major species	g/kg gas	g/kg gas	g/kg gas	g/kg gas	g/kg gas	g/kg gas	g/kg gas	g/kg gas
H ₂ O	987.5	973.5	983	966.8	956.4	949.2	952.8	5.1
CO ₂	9.2	18.8	13.1	25	31.4	38.8	35.1	5.3
SO ₂	2.7	7.4	3.6	3.5	5.3	4.5	4.9	0.5
H ₂ S	0.21	n.d.	0.08	3.5	6.6	7.1	6.89	0.4
N ₂	0.17	0.14	0.14	1.17	0.22	0.22	0.22	0.41
Minor and traces	mg/kg gas	mg/kg gas	mg/kg gas	mg/kg gas	mg/kg gas	mg/kg gas	mg/kg gas	mg/kg gas
HCl	219	115	76	64	134	92	113	29.4
HF	9.9	5.5	2.2	9.7	3.3	0.67	2	0.8
He	0.009	0.009	0.005	0.012	0.012	0.019	0.015	0
H ₂	0.07	0.15	0.1	0.15	0.15	0.24	0.2	0.1
Ar	12.6	6.3	6.23	9.7	1.9	1.7	1.8	0.1
O ₂	0.11	3.44	0.18	0.2	0.08	0.32	0.2	0.2
CH ₄	0.079	0.001	0.001	0.01	0.001	0.019	0.01	0
Si	8.3	132	97	n.a.	n.a.	n.a.	114	25
Na	17	40	66	n.a.	n.a.	n.a.	53	19
Ca	6.5	37	29	54	32	22	32	12
B	4.3	21	22	n.a.	n.a.	n.a.	21	1
Fe	7.2	11	26	25	17	8	17	8
Al	5.2	16	21	n.d.	n.d.	9	16	6
K	2.4	3.8	15	n.a.	n.a.	n.a.	9.5	8
Mg	1.6	3.3	6.3	10	6.6	2.9	6.3	3
P	1.6	5.4	6.8	n.a.	n.a.	n.a.	6.1	1
As	0.82	3.5	3.8	3.1	2.1	0.9	3.1	1
Cr	0.91	1.1	3.1	3.1	2.3	1.3	2.3	1
Cu	1	2	3	3	2	2	2	1
Se	0.36	2.3	2.1	2	2	1	2	1
Ti	0.24	2.6	1.8	2.3	1.6	1	1.8	1
Ni	0.41	1	1.7	1.7	1.3	0.5	1.3	1
Zn	0.28	1	1.3	1.4	1	0.45	1	1
Mn	0.14	n.d.	0.84	2.3	0.68	0.31	0.76	0.9
Te	0.12	0.52	0.61	n.a.	n.a.	n.a.	0.56	0.3
Sc	0.15	0.55	0.7	0.7	0.46	0.21	0.55	0.2
V	0.06	0.18	0.26	0.2	n.d.	0.06	0.19	0.1
Sr	0.02	0.17	0.1	0.14	0.08	0.14	0.14	0.1
Pb	0.01	0.06	0.07	0.09	0.05	0.03	0.06	0
Trace elements	µg/kg gas	µg/kg gas	µg/kg gas	µg/kg gas	µg/kg gas	µg/kg gas	µg/kg gas	µg/kg gas
Ba	10	383	265	341	261	130	265	97
Hg	12	56	124	n.a.	n.a.	n.a.	90	48
Li	2	11	14	123	83	82	82	49
Sb	10	36	41	39	30	12	36	12
Zr	1	13	8	30	32	31	30	11
Mo	3	43	29	33	20	8	29	13
Rb	7	24	30	43	26	25	26	8
Tl	2	35	20	34	22	12	22	10
Sn	3	28	18	30	16	17	18	7
Be	4	12	18	16	11	5	12	5
La	2	10	8	n.a.	n.a.	n.a.	9	1
Ce	2	16	8	14	8	8	8	4
Ga	2	9	8	9	6	5	8	2
Nd	2	5	11	13	8	7	8	3

Trace elements	µg/kg gas	µg/kg gas	µg/kg gas	µg/kg gas	µg/kg gas	µg/kg gas	µg/kg gas	µg/kg gas
Y	2	8	8	9	6	7	8	1
Bi	n.d.	n.d.	2	57	10	0.4	6	26
Ho	n.d.	5	5	5	3	1	5	1
Nb	n.d.	5	5	5	4	2	5	1
Co	n.d.	176	48	0.9	1.6	1.4	1.6	76
Cs	n.d.	194	99	1.3	0.8	0.8	1.3	87
Sm	n.d.	52	35	0.5	0.2	0.9	0.9	24
Pr	n.d.	93	59	0.7	0.3	0.9	0.9	43
Hf	n.d.	n.d.	n.d.	0.8	0.9	0.5	0.8	0.2
Dy	n.d.	25	21	0.5	0.2	0.8	0.8	12
Th	n.d.	1	1	1.1	0.6	0.7	0.7	0.2
Gd	n.d.	n.d.	46	0.4	0.2	0.7	0.6	23
W	75	62	52	0.2	0.6	0.1	0.6	31
In	n.d.	2	1	0.5	0.3	0.5	0.5	1
Er	n.d.	54	46	0.2	0.1	0.4	0.4	27
Au	n.d.	n.d.	0.4 ?	<4	<3	<2	0.4 ?	-
Yb	n.d.	19	15	0.2	0.1	0.3	0.3	9
Cd	n.d.	n.d.	n.d.	0.3	0.1	0.2	0.2	8
U	n.d.	38	48	0.2	0.1	0.3	0.3	24
Eu	n.d.	8	5	0.1	0.05	0.2	0.2	4
Tb	n.d.	n.d.	6	0.1	0.03	0.1	0.1	3
Tm	n.d.	2	2	0.03	0.02	0.05	0.05	1
Lu	n.d.	3	2	0.04	0.02	0.04	0.04	1
Ta	2	n.d.	n.d.	0.01	n.d.	n.d.	0.01	-
Ag	n.d.	n.d.	<0.3	<5	<4	<2	<3	-

n.d. indicates that the element was not detected and n.a. indicates that the element was not analyzed.

Appendix VII: fO_2 – pH Diagram

Reaction	log K (225 °C and 50 bar)	Source
$H_2S = HS^- + H^+$	-6.82	1
$HSO_4^- = SO_4^{2-} + H^+$	-4.84	1, 2
$H_2S + 2O_2 = HSO_4^- + H^+$	66.50	1, 2
$H_2S + 2O_2 = SO_4^{2-} + 2H^+$	61.66	1
$HS^- + 2O_2 = SO_4^{2-} + H^+$	68.48	1
$2KAl_3Si_3O_{10}(OH)_2 + 2H^+ + 3H_2O = 3Al_2Si_2O_5(OH)_4 + 2K^+$	-4.75	3
$3KAlSi_3O_8 + 2H^+ = KAl_3Si_3O_{10}(OH)_2 + 6SiO_2 + 2K^+$	-8.05	3
$KAl_3(SO_4)_2(OH)_6 + 8H^+ = 2HSO_4^- + K^+ + 3Al^{3+} + 6H_2O$	-11.83	2, 4
$KAl_3(SO_4)_2(OH)_6 + 10H^+ = 2H_2S + K^+ + 3Al^{3+} + 6H_2O + 4O_2$	-144.83	1, 2
$2KAl_3(SO_4)_2(OH)_6 + 2H^+ + 6SiO_2 + 3H_2O =$ $3Al_2Si_2O_5(OH)_4 + 8O_2(g) + 2K^+ + 4H_2S$	-283.76	1, 3, 4
$2KAl_3(SO_4)_2(OH)_6 + 6SiO_2 + 3H_2O = 3Al_2Si_2O_5(OH)_4 + 2K^+$ $+ 4HSO_4^- + 2H^+$	-17.76	2, 3, 4
$S + H_2O + 1.5O_2 = HSO_4^- + H^+$	-44.34	2, 5
$S + H_2O = H_2S + 0.5O_2$	17.65	1, 5
$S + H_2O + 1.5O_2 = SO_4^{2-} + 2H^+$	-39.10	1, 5
$Fe_{0.9}S + 0.4O_2 + 0.8H_2S = 0.9FeS_2 + 0.8H_2O$	18.82	1, 6
$Fe_{0.9}S + 0.4O_2 + 0.8HS^- + 0.8H^+ = 0.9FeS_2 + 0.8H_2O$	24.27	1, 6
$0.9Fe_3O_4 + 3HS^- + 3H^+ = 3Fe_{0.9}S + 3H_2O + 0.3O_2$	19.84	1, 3, 6
$3FeS_2 + 6H_2O + 11O_2 = Fe_3O_4 + 6SO_4^{2-} + 12H^+$	307.91	1, 3, 6
$Fe_3O_4 + 3HS^- + 3H^+ = 3FeS_2 + 3H_2O(l) + 0.5O_2$	102.96	1, 3, 6
$Fe_2O_3 + 4SO_4^{2-} + 8H^+ = 2FeS_2 + 4H_2O + 7.5O_2$	-211.56	1, 3, 6
$Fe_2O_3 + 4HSO_4^- + 4H^+ = 2FeS_2 + 4H_2O + 7.5O_2$	-230.93	2, 3, 6
$2Fe_3O_4 + 0.5O_2 = 3Fe_2O_3$	18.85	3

(1) Johnson et al., 1992; (2) Shock et al., 1997; (3) Holland and Powell, 1998; (4) Stoffregen et al., 2000; (5) Helgeson et al., 1978; (6) Robie and Hemingway, 1995